ISSN en trámite

Geofísica Internacional

Revista Trimestral Publicada por el Instituto de Geofísica de la Universidad Nacional Autónoma de México

México
Volume 57 Number 2
April - June
2018

— Geofísica Internacional —

GEOFÍSICA INTERNACIONAL, Año 57, Vol. 57, Núm. 2, abril - junio de 2018 es una publicación trimestral, editada por la Universidad Nacional Autónoma de México, Ciudad Universitaria, Alcaldía Coyoacán, C.P. 04150, Ciudad de México, a través del Instituto de Geofísica, Circuito de la Investigación Científica s/n, Ciudad Universitaria, Alcaldía Coyoacán, C.P. 04150, Ciudad de México, Tel. (55)56 22 41 15. URL: http://revistagi.geofisica.unam.mx, correo electrónico: revistagi@igeofisica.unam.mx. Editora responsable: Andrea Rostan Robledo. Certificado de Reserva de Derechos al uso Exclusivo del Título: 04-2022-081610251200-102, ISSN: en trámite, otorgados por el Instituto Nacional del Derecho de Autor (INDAUTOR). Responsable de la última actualización Saúl Armendáriz Sánchez, Editor Técnico. Fecha de la última modificación: 31 de marzo 2018, Circuito de la Investigación Científica s/n, Ciudad Universitaria, Alcaldía Coyoacán, C.P. 04150, Ciudad de México.

Geofísica Internacional

Vol. 57, Núm. 2, abril-junio de 2018

Contents

Geofísica Internacional (2018) 57-2: 89-106

Original paper

Estimation of ground motion in Xalapa, Veracruz, Mexico during the 1920 (*M*~6.4) crustal earthquake, and some significant intraslab earthquakes of the last century

Francisco Córdoba-Montiel, Srhi Krishna Singh, Arturo Iglesias, Xyoli Pérez-Campos and K. Sieron

Received: October 10, 2016; accepted: January 18, 2018; published on line: April 02, 2018

Resumen

En este trabajo se estiman los movimientos del terreno en la ciudad de Xalapa, Veracruz, durante el sismo del 4 de enero de 1920 (M~6.4) y tres sismos intraplaca significativos ocurridos en la placa subducida (M_w7.0) a finales del siglo pasado. Estos eventos representan un escenario sísmico razonable para Xalapa. Para lograrlo, se instaló una red portátil de sismógrafos de banda ancha en nueve sitios de esta ciudad y uno adicional en un sitio duro de referencia fuera de la ciudad. A partir de registros de sismos, se estimó el efecto de sitio mediante el cálculo de los cocientes espectrales estándar (SSRs). Basados en el modelo de fuente ω^{-2} de Brune, el efecto de sitio obtenido mediante la técnica SSR, y la aplicación de un método estocástico, se estimaron los valores pico de aceleración ($A_{máx}$) y de velocidad ($V_{máx}$) del movimiento del terreno en Xalapa. En el caso del sismo de Xalapa de 1920, los valores estimados de $A_{máx}$ correspondientes a una caída de esfuerzos, $\Delta\sigma$, de 50 bar se encuentran entre 100 y 250 cm/s^2, excepto en dos ubicaciones en las que el efecto de sitio es muy grande y donde $A_{máx}$ alcanza valores entre 300 y 600 cm/s^2. Los valores de $V_{máx}$ estimados están dentro del intervalo de 10 y 20 cm/s, excepto en el punto con el mayor efecto de sitio donde es ~ 40 cm/s. Para $\Delta\sigma$ de 30 y 100 bar se producen aproximadamente la mitad y dos veces estos valores pico, respectivamente. La principal incertidumbre de estas estimaciones se debe al valor de $\Delta\sigma$, porque aunque parece razonable un rango de 30 a 100 bar para sismos corticales en la Faja Volcánica Trans-Mexicana (donde se localiza Xalapa), no está restringido por los datos. La media de la caída de esfuerzos para eventos intraplaca en la placa subducida, ~ 300 bar, está mejor delimitada a partir de estudios previos.Se estimaron una media de ~ 30 cm/s^2 para $A_{máx}$ y de 4 cm/s para $V_{máx}$ en Xalapa, para los sismos de 1973 (Orizaba) y de 1999 (Tehuacán); los valores correspondientes para el sismo de 1980 (Huajuapan) son ~ 10 cm/s^2 y 2 cm/s. La incertidumbre de la estimación se encuentra probablemente dentro de un factor de 2 a 3.

Las ecuaciones de predicción de movimiento del suelo desarrolladas a partir de datos en la región del antearco (con menor atenuación que la región del trasarco) y registrados en sitios duros parece funcionar razonablemente bien para los sitios de Xalapa, los cuales se ubican en la región trasarco. Esta observación sugiere que las ondas sísmicas de los sismos intraplaca que atraviesan la cuña del manto antes de llegar a Xalapa, sufren una atenuación relativamente elevada. Sin embargo, dichas ondas se amplifican debido al efecto de sitio local. Parece que en Xalapa los dos efectos, a grandes rasgos se equilibran entre sí.

Palabras clave: Sismo de Xalapa de 1920, sismos intraplaca en Xalapa, efecto de sitio, peligro sísmico.

F. Córdoba-Montiel
K. Sieron
Centro de Ciencias de la Tierra
Universidad Veracruzana
Xalapa, Veracruz, Mexico

S.K. Singh
Arturo Iglesias
X. Pérez-Campos
Instituto de Geofísica
Universidad Nacional Autónoma de México
Mexico City, Mexico
Corresponding author:

Abstract

Ground motions in Xalapa, Veracruz, Mexico, during the earthquake of January 4, 1920 (M~6.4), and three significant intraslab earthquakes (M_w7.0) of the last century were estimated. These events are reasonable scenario earthquakes for Xalapa. Towards this goal, portable broadband seismographs at nine sites in the city and an additional one at a reference hard site outside the city were deployed. Peak ground acceleration (A_{max}) and peak ground velocity (A_{max}) in Xalapa were estimated based on Brune ω^{-2} source model and the site effect, obtained from earthquake recordings by using the standard spectral ratio (SSR) technique, and the application of a stochastic method. During the 1920 Xalapa earthquake the estimated A_{max} values corresponding to a stress drop, $\Delta\sigma$, of 50 bar are between 100 and 250 cm/s^2, except at two sites where the site effect is very large and A_{max} values reach 300 and 600 cm/s^2. Estimated V_{max} values are between 10 and 20 cm/s, except at the site with the largest site effect where it is ~ 40 cm/s. $\Delta\sigma$ of 30 and 100 bar produce about half and twice of these peak values, respectively. The main uncertainty in the present estimations is due the $\Delta\sigma$ value, because although a range of 30 to 100 bar for crustal earthquakes in the Trans-Mexican Volcanic Belt (in which Xalapa is located) seems reasonable, it is not constrained by the data. The mean stress drop for intraslab events, ~ 300 bar, is better constrained from previous studies. A median A_{max} of ~ 30 cm/s^2 and a median V_{max} of 4 cm/s in Xalapa during the 1973 (Orizaba) and 1999 (Tehuacán) earthquakes was estimated; the corresponding values during the 1980 (Huajuapan) earthquake are ~ 10 cm/s^2 and 2 cm/s. The uncertainty in the estimation is probably within a factor of 2 to 3. The ground motion prediction equations developed from data in the forearc region with less attenuation (than the backarc region) and recorded at hard sites appear to work reasonably well for Xalapa sites, which lie in the back arc. This observation suggests that the seismic waves from intraslab earthquakes, traveling through the mantle wedge before arriving Xalapa, suffer relatively large attenuation. However, these waves get amplified due to local site effects. It seems that in Xalapa these two effects, roughly, balance each other.

Key words: 1920 Xalapa earthquake, intraslab earthquakes, site effects, seismic hazards.

Introduction

The Xalapa earthquake of January 4, 1920 (M_s6.4), is the second most deadly earthquake in Mexico's recent history; only the Michoacán earthquake of 1985 (M_w8.0) caused more deaths (Suárez, 1992). Flores and Camacho (1922) reported a detailed description of the 1920 earthquake, based on which Figueroa (1974) elaborated and published an isoseismal map of the earthquake. More recently, Suárez (1992) revisited the earthquake region, summarized the damage and felt reports, and re-interpreted the data in a modern seismotectonic framework. Suter *et al.* (1996) augmented felt and damage reports from newspaper accounts and produced a revised isoseismal map.

According to Flores and Camacho (1922), 647 persons were killed as a consequence of the earthquake. Suter *et al.* (1996) reported that the number of death exceeded 1500. Most of the deaths were caused by a mud avalanche and debris flow. Modified Mercalli intensity (MMI) exceeded X in the epicentral zone. Intensities were as high as X-XI in the towns of Chilchotla, Coatepec, Xico, and Teocelo. In Xalapa the intensities did not exceed VIII-IX (Suárez, 1992). The damage was more extensive in the south of the city. Many houses suffered damage and some walls collapsed. Serious damage was reported to the post office building, the Justice Palace , and the Government Palace.

Xalapa lies in the eastern part of the Trans-Mexican Volcanic Belt (TMVB) (Figure 1). The belt is host to faults that are nearly parallel and orthogonal to its approximately E-W axis (Johnson and Harrison, 1990; Suter *et al*., 2001). Seismicity is relatively low in the TMVB but moderate and large earthquakes do occur. Xalapa earthquake of 1920 is one example. Acambay earthquake of 1912 (M_s7.0), which occurred in the central part of the TMVB about 100 km WNW of Mexico City (Urbina and Camacho, 1913), is another example. Suárez *et al*. (1994) reported a large earthquake in 1568 (M~7) in/near Guadalajara which caused severe damage to the city. A relatively large earthquake on February 11, 1875, destroyed the town of San Cristóbal de la Barranca located about 40 km NNW of Guadalajara (García Acosta and Suárez Reinoso, 1996). Cities and towns in the Mexican altiplano, such as Xalapa, are exposed to seismic hazard from earthquakes in the TMVB. Unfortunately, with the exception of Mexico City and the city of Oaxaca, there are few strong-motion recordings of such earthquakes in other

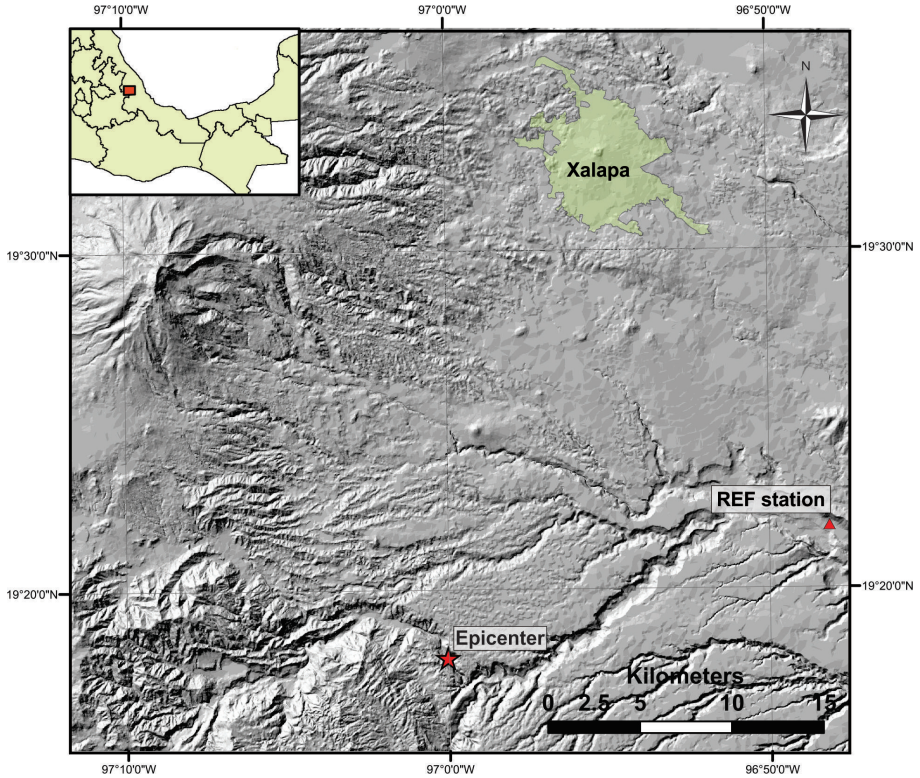

Figure 1. High resolution digital elevation model (Lidar image) showing the city of Xalapa, the epicenter of the 1920 Xalapa earthquake, and the reference site (REF).

cities of the altiplano. This leads to uncertainty in the estimation of seismic hazard. An estimation of ground motion during these events may be obtained by converting reported MMI to peak acceleration, A_{max}, or/or peak velocity, V_{max} (Trifunac and Brady, 1975; Wald *et al.*, 1999). This, however, is an extremely unreliable process, especially because no such relationship is available for the region of interest.

Xalapa is also exposed to large intermediate-depth, normal-faulting, intraslab earthquakes in the subducted Cocos plate. Such earthquakes have caused frequent, severe damage in the Mexican altiplano. Some examples are the earthquake of January 15, 1931 (*M*7.8), which caused heavy damage to the city of Oaxaca (Barrera, 1931; Singh *et al*., 1985), and the earthquakes of August 28, 1973 (M_w7.0), October 24 1980 (M_w7.0), and June 15, 1999 (M_w7.0), all of which resulted in deaths and damage in the states of Veracruz, Puebla, and Oaxaca (Singh and Wyss, 1976; Yamamoto *et al*., 1984; Singh *et al*., 1999). Significant intraslab earthquakes in the vicinity of Xalapa are listed in Table 1 and plotted in Figure 2. Of these events, the three recent M_w7.0 earthquakes of 1973, 1980, and 1999 were located within 250 km from Xalapa (Figure 2). Yet, due to lack of seismic instrumentation, no recording is available of ground motion produced by these events in the city. García *et al.* (2005) have derived ground motion prediction equations (GMPEs) for intraslab Mexican earthquakes. These equations are valid for hard sites in the fore-arc region. As Xalapa lies in the back-arc with possible significant site effect, there is no reason to expect that the GMPE would be valid for the city.

The main goal of this paper is to estimate A_{max} and V_{max} in Xalapa during the 1920 earthquake and during the three M_w7.0 intraslab earthquakes (1973 Orizaba, 1980 Huajuapan, and 1999 Tehuacán). To accomplish the latter, an estimation of the site effect at several locations in the city is performed and then a stochastic method is applied, an approach that has proven very useful in regions lacking recordings (Boore, 1983). The predicted ground motions from these types of earthquakes (shallow and intraslab) should help constrain and complement probabilistic seismic hazard analysis (PSHA) in the city of Xalapa.

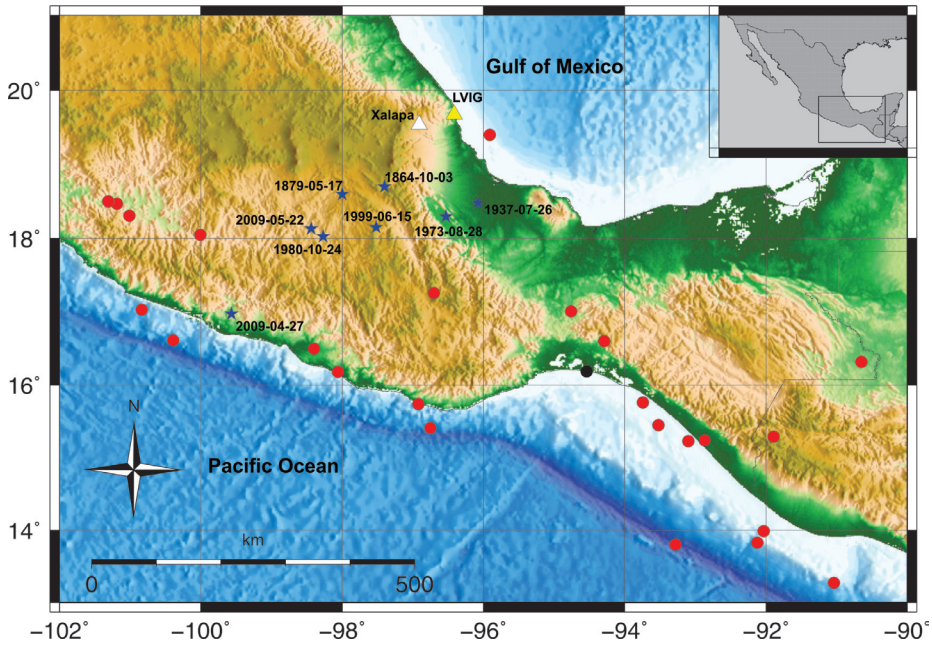

Figure 2. Seismicity location. Red circles: earthquakes used in the estimation of site effect in Xalapa. Blue stars: significant intraslab earthquakes within 250 km of Xalapa which are discussed in the text. Black dot: earthquake whose recordings at REF and LVIG are used to estimate the site effect at REF.

Table 1. Intraslab earthquakes within 250 km of Xalapa that are relevant to this study.

Event	Date	Latitude (ºN)	Longitude (ºW)	Depth	Magnitude
1	1864-10-03	18.70	97.40	---	7.3a
2	1879-05-17	18.60	98.00	---	7.0a
3	1937-07-26	18.48	96.08	85	7.3b
4	1973-08-28	18.30	96.53	82	7.3 (*m*B)c, 7.0 (M_w)d,e
5	1980-10-24	18.03	98.27	65	7.0 (*m*B)c, 7.0 (M_w)c,f
6	1999-06-15	18.15	97.52	60	7.0 (Mw)g
7	2009-05-22	18.10	98.43	41	5.7 (Mw)h

a. Singh *et al*. (1981)
b. Jiménez and Ponce (1978)
c. m_B: long-period body-wave magnitude (Abe, 1981)
d. Singh and Wyss (1976)
e. González-Ruiz (1986)
f. Yamamoto *et al*. (1984)
g. Singh *et al*. (1999)
h. UNAM Seismology Group (2010)

1920 Xalapa earthquake

A precise location of the earthquake and geometry of the causative fault could not be determined due to the lack of adequate seismic instrumentation. The epicenter of the event, 19.3 ºN, 97.0 ºW, listed in different studies of the earthquake, is based on the area that suffered the highest damage. This epicenter is ~ 29 km SSE of Xalapa (Figure 1). A Wiechert seismograph was temporarily installed in Xalapa within a few days after the earthquake. Hypocentral distances obtained from the seismograms of the aftershocks were 30 to 40 km, ruling out intraslab origin of the earthquake in the subducting Cocos plate since such an event would occur at depths greater than about 60 km (Suárez, 1992). The geologic

fault where the 1920 earthquake originated has not yet been identified and probably does not have a surface expression.

According to Suter *et al.* (1996), satellite imagery shows a lineament ≥ 15 km long and striking N72°E in the area of the highest damage. The orientation of this lineament is parallel to the trajectories of the tectonic maximum horizontal stress in this region, inferred from the alignments of Quaternary cinder cones (Suter, 1991; Zoback *et al.,* 1990). Normal faults have been mapped from geological surface observations further west in the TMVB (Johnson and Harrison, 1989; Suter *et al*., 1991). Earthquakes in the TMVB are shallow in depth (< 15 km) with normal-faulting focal mechanism (Suárez and Ponce, 1986; Singh *et al*., 2011). Most probably the Xalapa earthquake occurred also at a shallow (depth ≤ 15 km) on a normal fault with an ~ E-W orientation.

The magnitude of the Xalapa earthquake listed in the catalog of Mexican earthquakes by Figueroa (1970) is 7.8. This magnitude is unrealistically high. It does not appear to be an instrumental magnitude but was probably subjectively assigned, biased by the damage reports. Singh *et al*. (1984) estimated surface-wave magnitude, M_S, as 6.4 from an Uppsala Wiechert seismogram. Suárez (1992) reported body-wave magnitude, m_b, as 6.4. In this study, $M_w = M_S = m_b = 6.4$ will be taken for this earthquake, where M_w is the moment magnitude.

Intraslab earthquakes

The intraslab earthquakes relevant to this study, which have occurred in the states of Oaxaca, Veracruz, and Puebla, are shown in Figure 2 and listed in Table 1. The source parameters of the earthquakes of 1973, 1980, and 1999, including location, depth, and M_w, should be fairly reliable as they are based on special studies. It is for these three intraslab earthquakes that ground motions in Xalapa are estimated.

A Brief Description of the Stochastic Method

If Fourier amplitude spectrum and duration of the intense part of ground motion at a site can be specified, then the peak ground motion parameters can be estimated through the application of Parseval's theorem and results from the random vibration theory (Cartwright and Longuet-Higgins, 1956; Hanks and McGuire, 1981; Boore, 1983, 2003). An estimation of the Fourier acceleration amplitude spectrum of the ground motion of an earthquake, $A(f, R)$, can be obtained from the following relation which is valid under far-field, point-source approximation (Singh *et al*., 2002):

$$A(f,R) = C \cdot G(R)\,[\{f^2 \dot{M}_0(f)\}] \\ [S(f) e^{-pkf} B(f,f_m)\, e^{-\pi f R / bQ(f)}], \quad (1)$$

where

$$C = FPR_{\theta j}(2p)^2/(4\pi\rho b^3). \quad (2)$$

In equations (1) and (2), $\dot{M}_0(f)$ is the moment rate spectrum, R = hypocentral distance, $R_{\theta f}$ = average radiation pattern (0.55), F = free surface amplification (2.0), P takes into account the partitioning of energy in the two horizontal components ($1/\sqrt{2}$), b = shear-wave velocity in the focal region, ρ = density in the focal region, and $G(R)$ accounts for the geometrical spreading. The terms in the second square bracket of Equation (1) modify the source acceleration spectrum, $f^2 \dot{M}_0(f)$. In these terms $Q(f)$ = quality factor which includes both anelastic absorption and scattering. The attenuation in the near-surface layer and the finite bandwidth of the observed spectrum imposed by the sampling rate are taken into account by parameter κ (Singh *et al*., 1982; Anderson and Hough, 1984) and/or Butterworth filter $B(f, f_m)$. Following Boore (1983), $B(f, f_m) = (1.0 + (f / f_m)^8))^{-0.5}$ was taken. Often either $B(f, f_m)$ or κ is found sufficient to model the high-frequency fall off of the observed spectrum. $S(f)$ in Equation (1) is the local site effect.

In using Equation (1), it was assumed that the sources follow a Brune ω^{-2} model, i.e.,

$$\dot{M}_0(f) = M_0 f_c^2 / (f^2 + f_c^2), \quad (3)$$

where f_c is the corner frequency which is related to the source radius, a, by $f_c = 2.34\beta/2\pi a$ (Brune, 1970). The source radius, in turn, is related to stress drop, $\Delta\sigma$, by $\Delta\sigma = (7/16)(M_0/a^3)$.

To compute $A(f, R)$ estimations of $\Delta\sigma, f_m, \kappa, Q(f)$, and the site effect $S(f)$ are needed. As will be mentioned later in the text, $Q(f)$, corresponding to crustal and intraslab earthquakes, are reasonably well known. Reasonable values of $\Delta\sigma, f_m$, and κ in the estimation of peak ground motion parameters will be assumed. Below, the procedure used to estimate the site effect, $S(f)$, in Xalapa is described.

Deployment of portable seismographs in Xalapa

To determine the site effect, broadband seismographs were deployed in the city in nine locations (Figure 3). Some of these sites were located in the area that experienced the large damage during the 1920 earthquake. An additional station was installed on a hard site which was taken as the reference site. Given the low signal/noise ratio within the urban area, the reference station (henceforth called REF) was installed near the town of Jalcomulco ~ 20 km from Xalapa (Figure 1). At the REF site in Jalcomulco, basement rock is composed of Mesozoic calcareous rocks, characterized by a low noise level, while in Xalapa, the noise level is considerably higher. Although basaltic lava flows crop out throughout Xalapa city, the underlying volcanic stratigraphy includes loose pyroclastic material, which could explain the high noise levels.

Since only a limited number of seismographs were available, their location was changed three times during the experiment, thus occupying a total of nine sites. Only the REF station operated continuously at the same site.

The seismographs functioned in autonomous mode recording continuously at a sampling interval of 0.01 s. Figure 3 shows location of XALA, an accelerographic station operated by Instituto de Ingeniería, UNAM, and two portable seismographs that were deployed by another group at sites CERRO and IDIOMAS in 2009. A_{max} and V_{max} values of two earthquakes recorded at these stations were used in the present study to compare observed and estimated values.

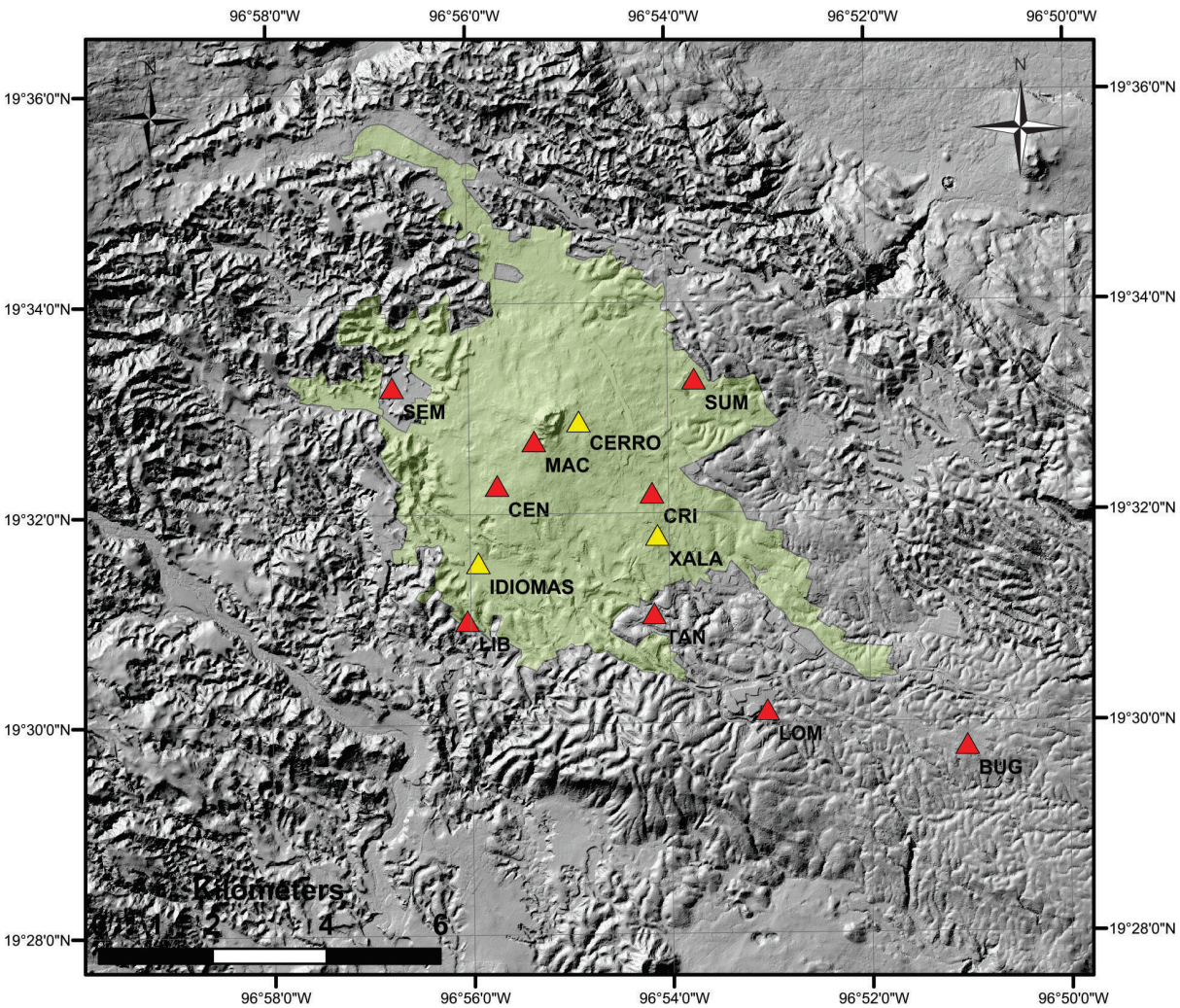

Figure 3. High resolution Lidar image of Xalapa. Red triangles: nine sites in the city where portable seismographs were deployed to estimate site effect. Yellow triangles: temporary stations (CERRO and IDIOMAS) deployed by another workgroup and the accelerographic station (XALA). XALA is operated by Instituto de Ingeniería, UNAM.

Site effect estimation using standard spectral ratio (SSR) technique

All the events reported by the Servicio Sismológico Nacional (Mexican National Seismological Service, SSN) that were recorded at the reference station, REF were first selected. From this set of earthquakes, those that were also recorded at one or more temporary sites in Xalapa were chosen. The earthquakes are listed in Table 2 and their locations are shown in Figure 2.

The recordings were first corrected for instrumental response. The standard spectral ratios (SSRs) were computed by dividing the Fourier amplitude spectrum of each of the horizontal components recorded at the Xalapa sites by the Fourier amplitude spectrum of the corresponding component at the reference station. Baseline correction and 5% cosine taper were applied to the traces before computing the amplitude spectrum. The spectra were smoothed by applying 1/6 octave filter before computing the spectral ratios (see Córdoba-Montiel, 2010 for details). The NS component sensor at the reference station REF failed on March 16th, 2008. Therefore, the SSRs of subsequent recordings were computed with only the EW component assuming both components to be equal. The same assumption was made at station LOM which NS component also failed during the experiment.

Site effect at the reference site REF

It was first checked that REF was indeed a hard site by computing horizontal to vertical (H/V) spectral ratios (Lermo and Chávez-García, 1993) using the records obtained at this site during the first months after installation. Figure 4 shows median and ±1 standard deviation curves of H/V spectral ratio computed for several registered earthquakes. The median ratio at REF was ~ 1 implying no significant amplification of seismic waves at this site and, hence, it was considered to be a hard site.

Table 2. Focal parameters of earthquakes used in the estimation of site effect at nine locations in Xalapa. Source: Mexican National Seismological Service (http://www.ssn.unam.mx).

Date	GMT Time	Latitude ^{0}N	Longitude ^{0}W	Depth km	M
26/11/2007	21:56:16	18.50	-101.31	53	5.6
07/12/2007	06:00:01	16.50	-98.40	20	4.7
11/12/2007	01:28:52	15.74	-96.92	27	4.6
13/12/2007	17:08:54	17.26	-96.70	82	4.5
04/01/2008	14:27:57	17.01	-94.76	122	4.4
05/01/2008	01:56:45	13.83	-92.12	63	5.6
06/01/2008	16:55:20	13.99	-92.03	20	5.0
12/02/2008	12:50:18	16.19	-94.54	90	6.6
12/03/2008	04:51:52	15.23	-93.10	97	4.8
12/04/2008	08:23:18	17.03	-100.84	20	4.5
15/04/2008	03:03:06	13.27	-91.04	40	6.5
15/04/2008	07:31:43	18.31	-101.01	65	4.6
17/04/2008	01:52:59	15.45	-93.52	95	5.4
28/04/2008	00:06:29	18.05	-100.01	52	5.6
28/04/2008	08:18:02	16.61	-100.39	7	4.6
29/04/2008	10:56:42	18.47	-101.19	60	5.4
30/04/2008	10:47:10	15.24	-92.87	125	4.5
04/05/2008	10:21:35	15.41	-96.75	10	4.5
17/05/2008	20:04:08	16.18	-98.06	40	4.8
25/05/2008	05:45:12	15.29	-91.89	198	4.7
31/05/2008	08:05:30	16.32	-90.65	25	4.8
05/06/2008	05:11:26	15.76	-93.74	99	4.8
22/06/2008	01:32:07	16.60	-94.29	112	4.9
27/06/2008	02:33:03	19.40	-95.91	22	4.0
29/06/2008	09:42:19	13.80	-93.28	25	5.1

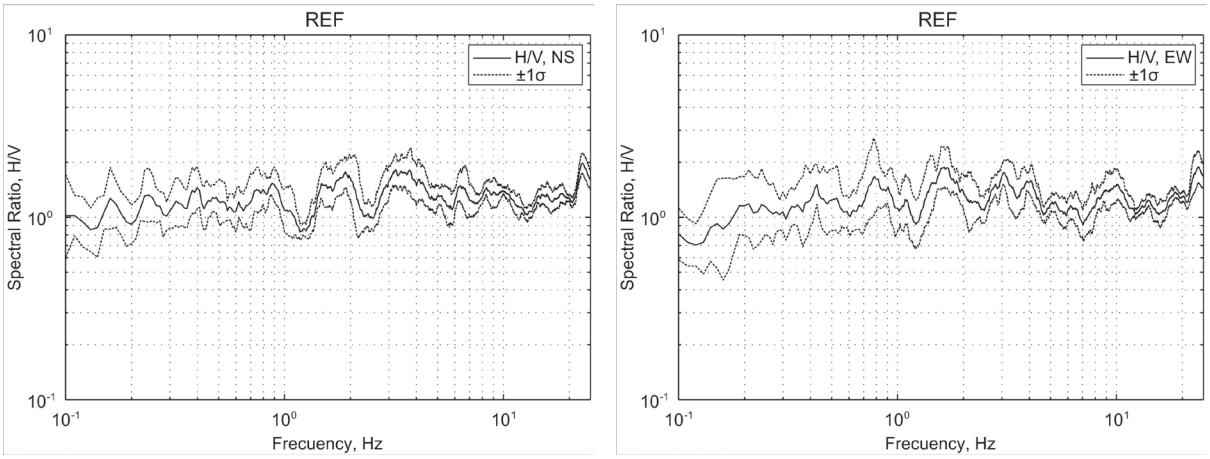

Figure 4. Horizontal to vertical (H/V) spectral ratio as a function of frequency at the reference station, REF. The curves corresponding to the median and ±1 standard deviation are shown. Left: NS component, right: EW component.

Figure 5 shows SSRs (site/REF spectral ratios) at sites in Xalapa. These ratios illustrate a de-amplification around f = 10 Hz at most of the sites which suggests either high attenuation of seismic waves at sites in Xalapa or an amplification at REF near 10 Hz. An amplification at REF site would not be problematic if ground motions of future earthquakes could be predicted on this site. The motions elsewhere in Xalapa could then be estimated using the known site effect (relative to REF). This, for example, is the method often used in Mexico City where the observed or estimated ground motion at the reference site of CU (Ciudad Universitaria, a hill-zone site in Mexico City) is used to calculate the motions elsewhere in the city (Singh *et al*., 1988). The method was validated by Ordaz *et al*. (1988). The estimation of ground motion at CU is possible since many events have been recorded at the site since 1964. This, of course, is not the case for the reference site REF. It is, therefore, important to know if REF is amplified at high frequencies and, if so, to quantify this amplification.

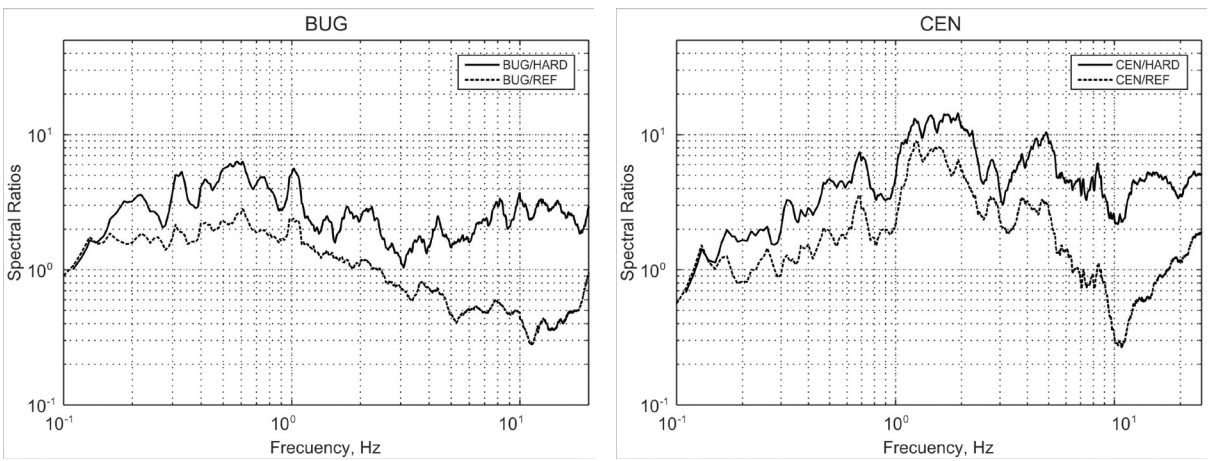

Figure 5. Standard spectral ratios (SSRs) of EW component at sites in Xalapa. Dashed curves: *Site/REF* spectral ratios. Continuous curves: *Site/Hard (Site/LVIG)* spectral ratios.

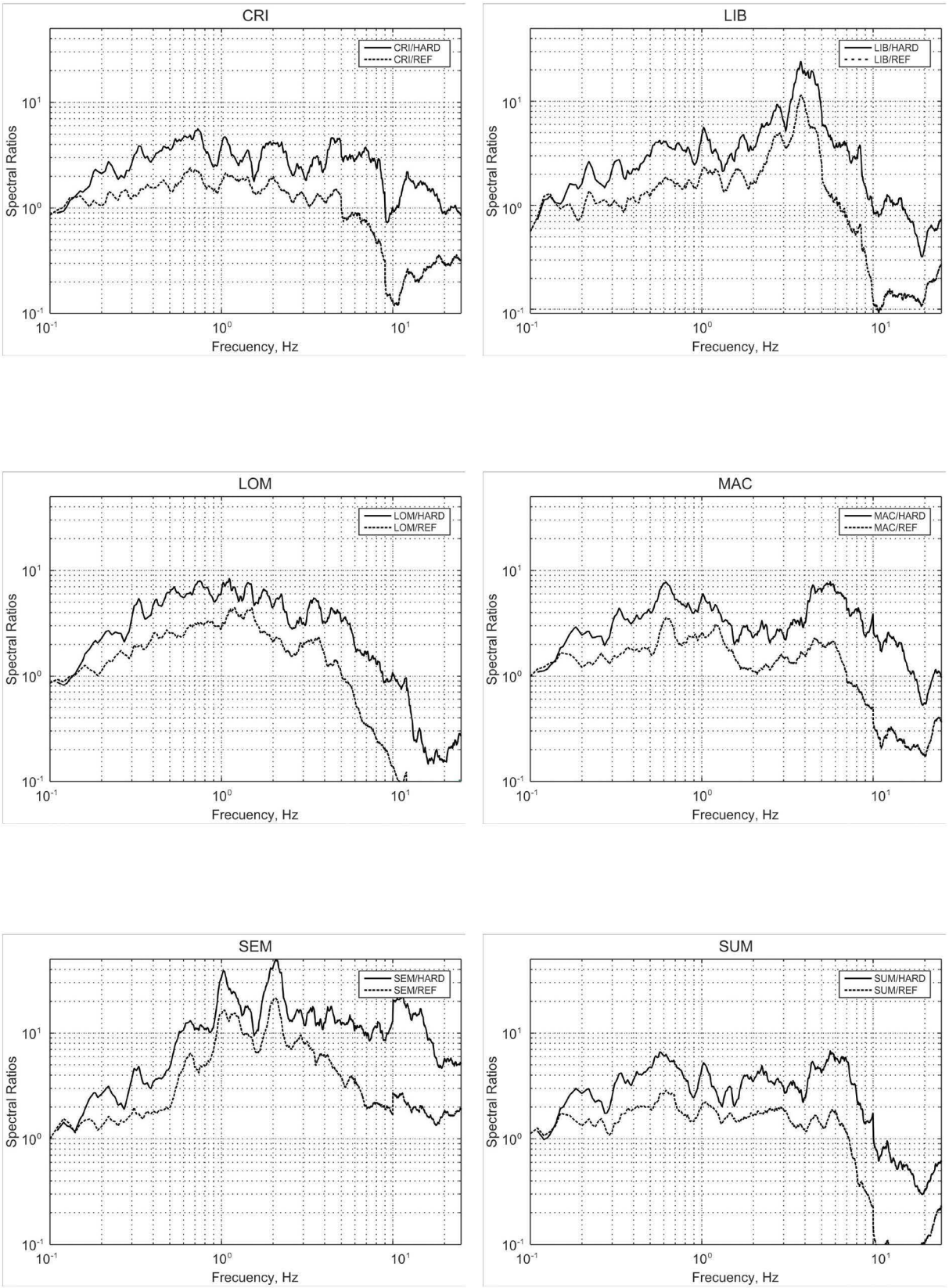

Figure 5. Continued.

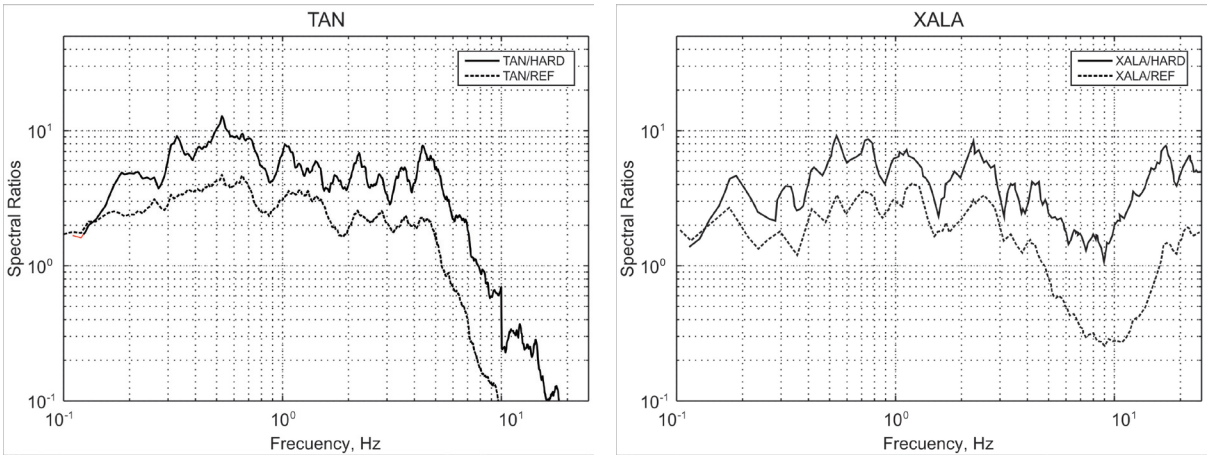

Figure 5. Continued.

Recordings at REF and LVIG produced by the Oaxaca earthquake of February 12, 2008 (16.35 ºN, 94.51 ºW; M_w6.5, H = 87 km, black circle in Figure 2), provide an opportunity to check and quantify possible site effect at REF (Figure 6). LVIG is a SSN broadband station located in the Laguna Verde nuclear plant facility, it is approximately at the same distance (~ 440 km) and nearly at the same azimuth as REF (Figure 2). LVIG is a known hard site (Singh *et al*., 2006). The median REF to LVIG spectral ratio of the two horizontal components is shown in Figure 7. There are three arguments which support REF/LVIG spectral ratio as reasonable proxy for the spectral amplification at REF with respect to a hard site. Firstly, as mentioned above LVIG is known to be a hard site (Singh *et al*., 2006). Secondly, a peak in the REF/LVIG spectral ratio occurs at about 10 Hz (Figure 7) which corresponds to the sag in the spectral ratios at sites in Xalapa with respect to REF (Figure 5). Thirdly, as shown later, the observed spectrum at REF during an intraslab earthquake of May 22, 2009, is similar to the theoretical spectrum corrected for REF site effect. Clearly, a truly hard site in Xalapa would have been desirable as a reference site. However, the use of REF/LVIG spectral ratio as the spectral amplification at REF with respect to a hard site is a reasonable compromise.

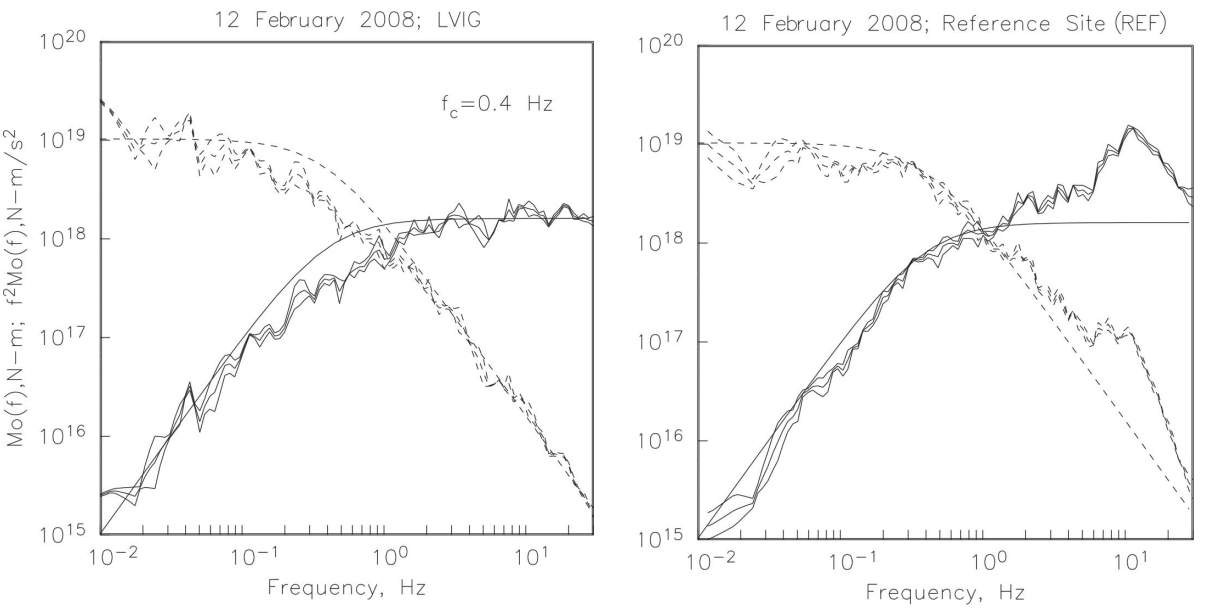

Figure 6. The source displacement (dashed curves) and acceleration spectra (continuous curves) retrieved from the recordings at LVIG and REF are shown on left and right graphics , respectively.

To estimate site effect in Xalapa with respect to a "true" hard site, we need to multiply the SSRs computed with respect to REF, shown in Figure 5, by the REF/ LVIG spectral ratio given in Figure 7. The resulting site effect is also shown in Figure 5. Two sites with unusually large amplification are LIB (~ 20 times at ~ 4 Hz) and SEM (~ 40 times at ~ 2 Hz).

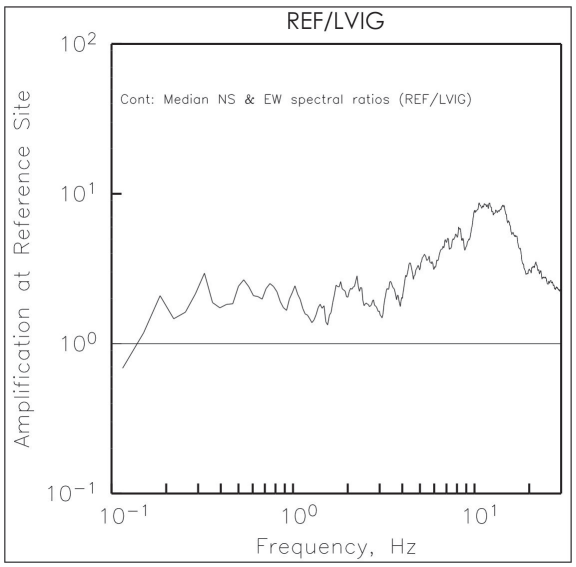

Figure 7. Median (REF/LVIG) spectral ratio of the two horizontal components of February 12, 2008, earthquake (black dot in Figure 2). Since LVIG is a hard site, the spectral ratio gives site effect at REF.

Ground motions in Xalapa

Under some further reasonable assumptions, we can now compute $A(f, R)$ in Equation (1) using the random vibration theory to estimate peak ground motion parameters. The shallow Xalapa earthquake of 1920 and the intraslab earthquakes will be separately treated.

Estimation of ground motion for the 1920 Xalapa earthquake

As the earthquake was shallow, $\rho = 2.85$ gm/cm^3 and $\beta = 3.6$ km/s were chosen in the source region. Since R ~ 30 km, in this case the geometrical spreading term, $G(R)$ was taken, as $1/R$. $Q = 98f^{0.72}$ obtained by Singh *et al*. (2007) for the central TMVB was taken. A ω^{-2} Brune source model (Equation 3) was assumed. Following Herrmann (1985), the approximation for the duration of the intense part of the ground motion, T_d, by $T_d = 1/f_c + 0.05R$, where R is in km was used. It was assumed that the high-frequency fall off of the spectrum could be adequately modeled by $B(f, f_m)$ and setting $\kappa = 0.0$ s (this value for 1920 earthquake was based on REF recordings). Figure 8 shows estimated A_{max} and V_{max} assuming f_{max} = 10 and 15 Hz, and $\Delta\sigma$ = 30, 50 and 100 bar, a reasonable range of stress drop for crustal earthquakes in the TMVB. Observed spectra at REF support f_{max} between 10 and 15 Hz (Córdoba-Montiel, 2010) and $\kappa = 0.0$ s. As expected, the peak values are somewhat greater for f_{max} of 15 Hz than 10 Hz. For $\Delta\sigma$ = 50 bar and f_{max} of 15 Hz, the estimated A_{max} values were between 100 and 250 cm/s^2, except at sites LIB and SEM where they are ~ 300 and 600 cm/s^2, respectively. These are also the sites with large site effect (Figure 5). $\Delta\sigma$ of 30 and 100 bar produce about half and twice of these peak values, respectively. Estimated V_{max} values for $\Delta\sigma$ = 50 bar were between 10 and 20 cm/s, except at SEM where it is ~ 40 cm/s. Again, $\Delta\sigma$ of 30 and 100 bar give rise to about half and twice of these peak values. At a hypothetical hard site in Xalapa (R ~ 30 km), A_{max} and V_{max}, corresponding to $\Delta\sigma$ = 50 bar, would be 40 cm/s^2 and 3.5 cm/s, respectively. Thus, the site effect in the city causes an amplification of A_{max} and V_{max} by a factor of ~ 3 to 6.

Estimation of ground motions for intraslab earthquakes

Note that hypocentral distances of the 1973 Orizaba and 1999 Tehuacán earthquakes from Xalapa are roughly the same (168 km and 177 km, respectively). As the magnitudes of the two earthquakes are the same, M_w7.0, the estimated peak ground motions for the 1973 earthquake will also be roughly valid for the 1999 earthquake.

For simulating ground motions, ρ = 3.2 gm/cm^3 and β = 4.68 km/s were chosen in the source region. Following García *et al*. (2004), the geometrical spreading, $G(R)$, is taken as $1/R$ for all R. García *et al*. (2004) reported $Q(f) = 251f^{0.58}$ for intraslab earthquakes, the stations reported by these authors were located in the forearc region. Singh *et al.* (2006) analyzed seismograms of intraslab earthquakes recorded at station LVIG, located in the backarc, and relatively close to Xalapa (Figure 2). They found that *S* waves were highly attenuated requiring a quality factor given by $Q(f) = 120f^{0.75}$. These authors attributed low Q to wave trajectories partly traversing through the mantle wedge. In the present ground motion simulations at Xalapa this Q will be used. Also f_{max} = 15 Hz and κ = 0.04 s were selected (for intermediate-depth events this value was based on intraslab earthquake recording of May 22, 2009).

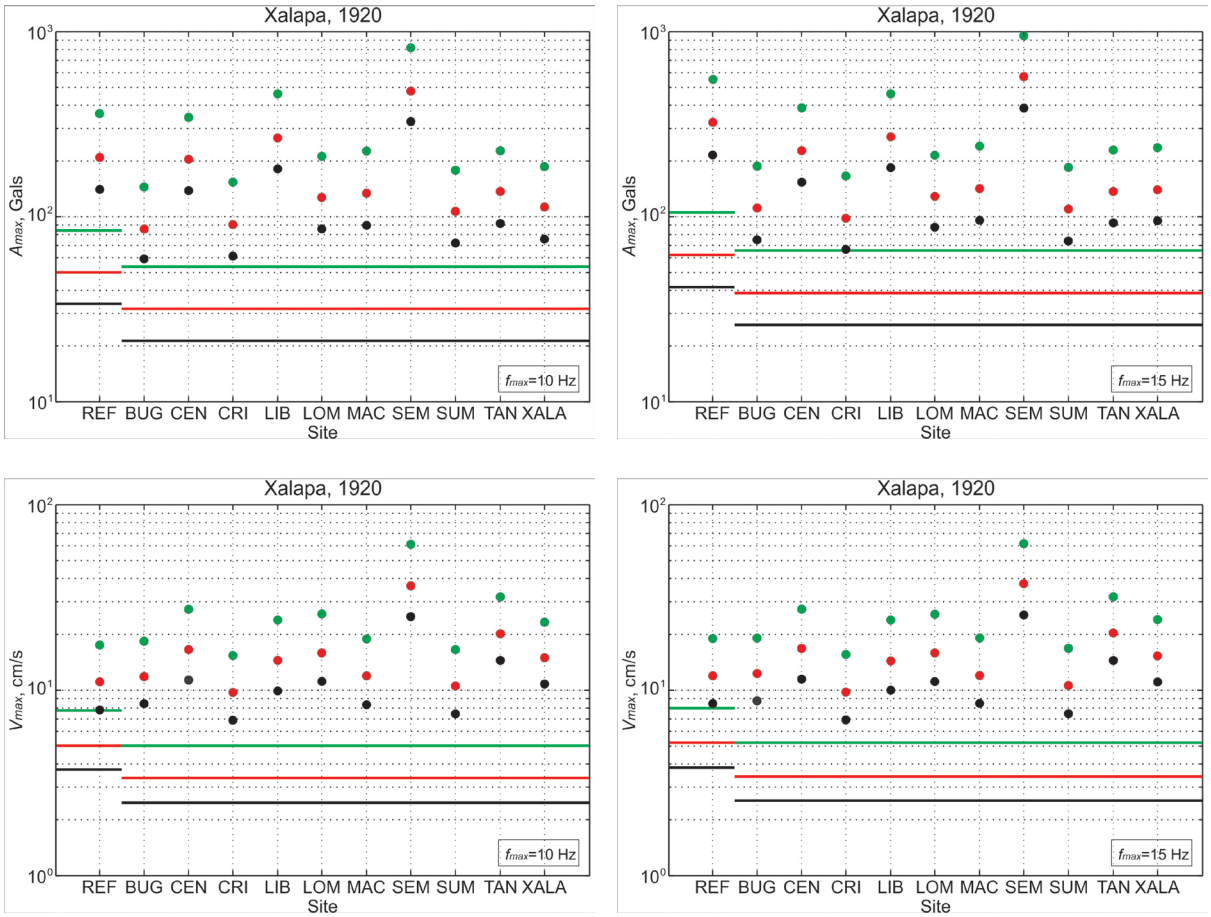

Figure 8. Estimated A_{max} and V_{max} at sites in Xalapa and at REF during the 1920 Xalapa earthquake assuming f_{max} = 10 and 15 Hz. Black, red, and green dots correspond to Δσ of 30, 50, and 100 bars, respectively. Black, red, and green lines show estimated values corresponding to Δσ of 30, 50, 100 bars, respectively, ignoring the site effect.

A validation of the chosen parameters above is provided by the recordings of the intraslab earthquake of May 22, 2009, which was located near the 1980 Huajuapan earthquake (Figure 2, Table 1). It was recorded at stations REF, XALA, IDIOMAS, and CERRO in Xalapa, and at LVIG in Laguna Verde. Unfortunately, the seismograms at IDIOMAS and CERRO were not available for analysis in the present study, only the A_{max} and V_{max} values. The 2009 earthquake was studied in some detail by UNAM Seismology Group (2010). From the analysis of *S*-wave spectra, M_0 and $\Delta\sigma$ of the earthquake were estimated as 4.6x10^{17} Nm (M_w5.7) and 340 bar, respectively. Figure 9 compares the observed spectra with the estimated spectra at REF, XALA, and LVIG (through Equation 1) using the parameters given above, including and excluding site effect (site effect = 1 for LVIG). The spectra ignoring the site effect are, as expected, well below the observed ones. The observed and estimated spectra with site effect are in reasonable agreement, except at low frequencies. The disparity at low frequencies, which is due to poor estimations of the stochastic method at low frequencies (i.e. Boore, 1983), can be reduced by assuming a larger magnitude and/or choosing $G(R)$ corresponding to the dominance of surface waves. A larger magnitude, however, is unacceptable as it would not be in agreement with the study of UNAM Seismological Group (2010) and M_w5.6 reported in the Global CMT catalog. On the other hand, the dominance of surface waves over body waves and $Q(f) = 120f^{0.75}$ are not compatible. A_{max} and V_{max} are associated with the spectrum at higher frequencies (f > 1 Hz). Since the estimated and observed spectra are in reasonable agreement at f > 1 Hz, it was justified to use the parameters given above for estimating spectra of the target events. Estimated (via stochastic method) and observed A_{max} and V_{max} at sites REF, XALA, and LVIG are given in Table 3 along with the predictions from the GMPE for intraslab Mexican earthquakes by García *et al*. (2005). The estimations from the stochastic method at

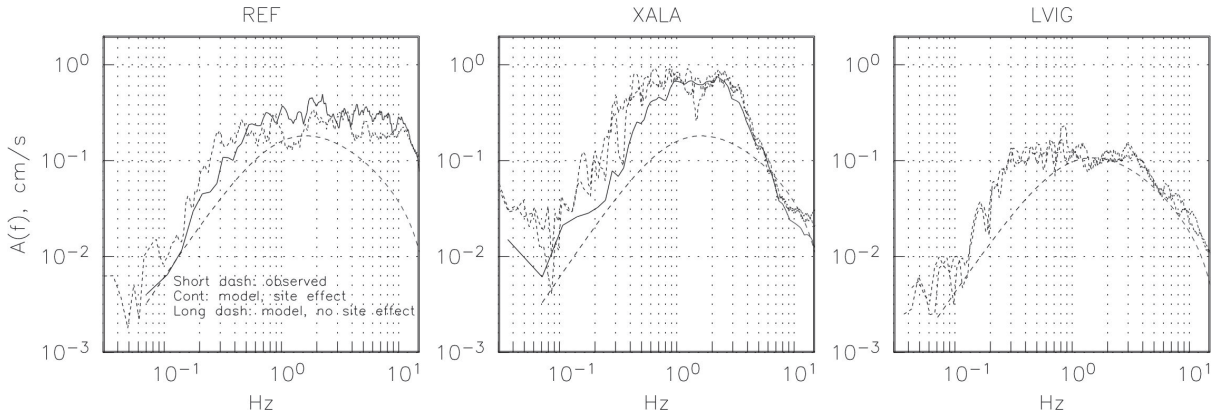

Figure 9. Observed spectra (short dashed curves) of horizontal components at REF, XALA, and LVIG for the intraslab Chiautla earthquake of 2009 (Table 1). Estimated spectra (through Equation 1), including site effect (continuous curves) and excluding site effect (long dashed curves) are also shown. The spectra ignoring the site effect, , are below the observed ones. The observed and estimated spectra with site effect are in reasonable agreement except at low frequencies (see text).

REF and XALA are greater, but within a factor of ~ 2, from the observed ones. The results in Table 3 give some confidence that the stochastic predictions for target earthquakes, based on the chosen parameters given above, may be accurate within a factor of 2 to 3. Estimated A_{max} and V_{max} at sites in Xalapa along with observed values, if available, are shown in Figure 10. As in the case of the 1920 earthquake, relatively high peak values, related to large site effects (Figure 5), occur at SEM, LIB, and CEN. Figure 10 also shows predictions from the GMPE and stochastic method excluding site effect. Stochastic predictions of A_{max} and V_{max} in Xalapa with and without site effect differ by a factor of ~ 3 to 6. Curiously, the estimated A_{max} in Xalapa via stochastic method including site effect is, on average, about the same as from the GMPE even though there is a considerable site effect in the city. This is most probably a consequence of two opposing effects. Although the seismic waves suffer amplification due to the site effect, it is counterbalanced by higher attenuation due to lower Q along the wave path traversing the mantle wedge. The estimated V_{max} from stochastic method at Xalapa site, on average, is greater by a factor of ~ 2 as compared to that from GMPE (Figure 10). It seems that the amplification caused by site effect and deamplification resulting from a low Q in the mantle wedge do not balance at frequencies related to V_{max} and the amplification effect dominates.

Table 3. Observed and estimated A_{max} and V_{max} during intraslab earthquake of 22 May 2009 (M_w5.7) at sites REF and XALA in Xalapa, and LVIG in Laguna Verde.

Station	Observed				Stochastic estimation#		Estimation fro GMPE$	
	A_{max}, cm/s^2		V_{max}, cm/s		A_{max}, cm/s^2	V_{max}, cm/s	A_{max}, cm/s^2	V_{max}, cm/s
	NS	EW	NS	EW				
REF%	-	7.0e-1	-	3.3e-2	1.5e0	9.1e-2	1.8e0	8.7e-2
XALA	9.0e-1	7.8e-1	1.1e-1	1.1e-1	1.9e0	2.1e-1	1.7e0	8.4e-2
LVIG	1.7e-1	2.3e-1	2.1e-2	2.7e-2	3.9e-1	3.7e-2	8.8e-1	5.2e-2

Stochastic estimation is based on ω^{-2} source model with M_w5.7, $\Delta\sigma$ = 340 bar, $Q(f) = 120f^{0.72}$, f_{max} = 15 Hz, κ = 0.04 s, and includes site effect at REF and XALA (see text). Site effect is taken 1 at LVIG.
$ GMPE from García et al. (2005) for the quadratic mean of the two horizontal components.
% NS component malfunctioned at REF.

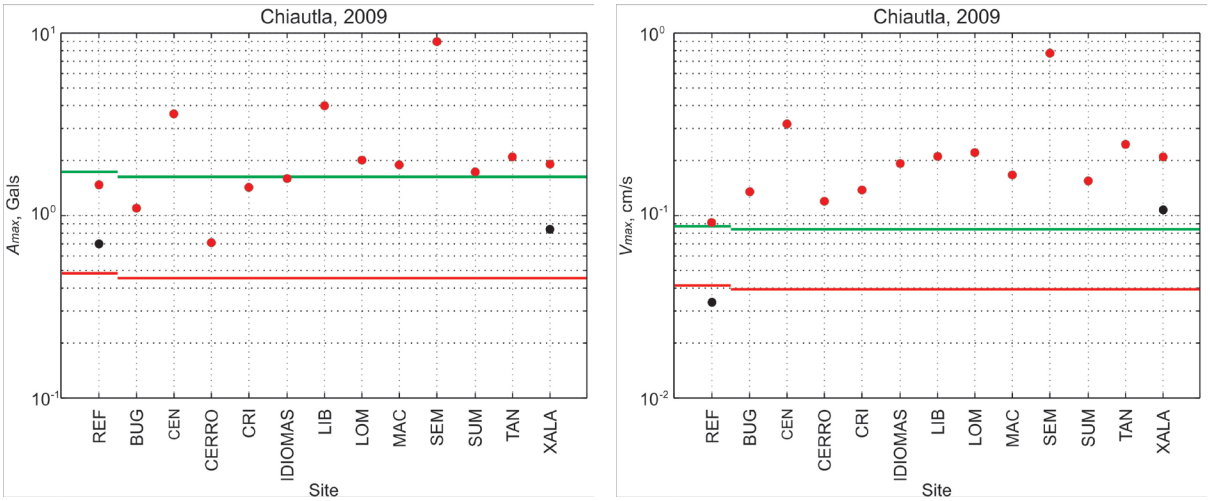

Figure 10. Estimated (red dots) and observed (blue dots) A_{max} and V_{max} at sites in Xalapa and at REF for the Chiautla earthquake of 2009. The estimations are from application of the stochastic method. Red line shows stochastic estimation excluding site effect. Green line indicates estimation from GMPE of García *et al*. (2005).

Peak ground motions in Xalapa during the intraslab earthquakes of 1973 and 1980 were estimated using the stochastic method and the parameters given above. As mentioned earlier, the earthquake of May 22, 2009, was located near the 1980 earthquake (Figure 2). The recordings of the 2009 event at REF and XALA as empirical Green's function (EGF) were used to synthesize motions at these sites following a random summation scheme proposed by Ordaz *et al*. (1995). In the synthesis a stress drop was used, $\Delta\sigma$, of 340 bar for the EGF event of 2009 as reported by UNAM Seismology Group (2010). The same stress drop for the target events was assumed. Table 4 lists the estimated peak values at sites REF and XALA from the stochastic method and the GMPE for the 1973 and 1980 earthquakes. For the latter earthquake, the estimated peak values from the EGF technique are also listed. The predictions from the stochastic method are similar to those obtained by the EGF technique for the 1980 earthquake. Unlike the 2009 earthquake, the estimated A_{max} at Xalapa sites by the stochastic method is, on average, somewhat larger than that predicted by the GMPEs for both 1973 and 1980 earthquakes (Figure 11). Estimated V_{max} from the stochastic method for both earthquakes are consistently larger than those obtained from GMPE by a factor of ~ 2 (Figure 11). The present estimated A_{max} and V_{max} values at sites in Xalapa during the 1973 Orizaba earthquake are ~ 30 cm/s^2 and 4 cm/s, respectively; the corresponding values during the 1980 Huajuapan earthquake (and, hence, also during the 1999 Tehuacán earthquake) are ~12 cm/s^2 and 2 cm/s.

Table 4. Estimated A_{max} and V_{max} at sites REF and XALA near/in Xalapa from M_w7.0 intraslab earthquakes of 1973 and 1980.

Earthquake	Station	EGF estimation%				Stochastic estimation#		Estimation from GMPE$	
		A_{max}, cm/s^2		V_{max}, cm/s		A_{max},	V_{max},	A_{max},	V_{max},
		NS	EW	NS	EW	cm/s^2	cm/s	cm/s^2	cm/s
1973,	REF, R = 147 km	-	-	-	-	20.3	2.4	67.9	2.4
M_w7.0	XALA, R = 168 km	-	-	-	-	24.6	4.6	50.8	1.9
1980,	REF, R = 224 km	-	3.2	-	0.8	6.9	1.0	16.9	0.9
M_w7.0	XALA, R = 229 km	8.2	7.5	2.9	2.1	11.3	2.3	15.7	0.9

% Accelerogram of May 22, 2009 (M_w5.7), used as empirical Green´s function. Synthesis follows a random summation scheme proposed by Ordaz *et al*. (1995). $\Delta\sigma$ = 340 bar for both EGF and target events.
# Stochastic estimation is based on ω^{-2} source with M_w7.0, $\Delta\sigma$ = 304 bar, $Q(f) = 120f^{0.72}$, f_{max} = 15 Hz, κ = 0.04 s, and includes site effect at XALA (see text).
$ GMPE from García *et al*. (2005) for the quadratic mean of the two horizontal components.

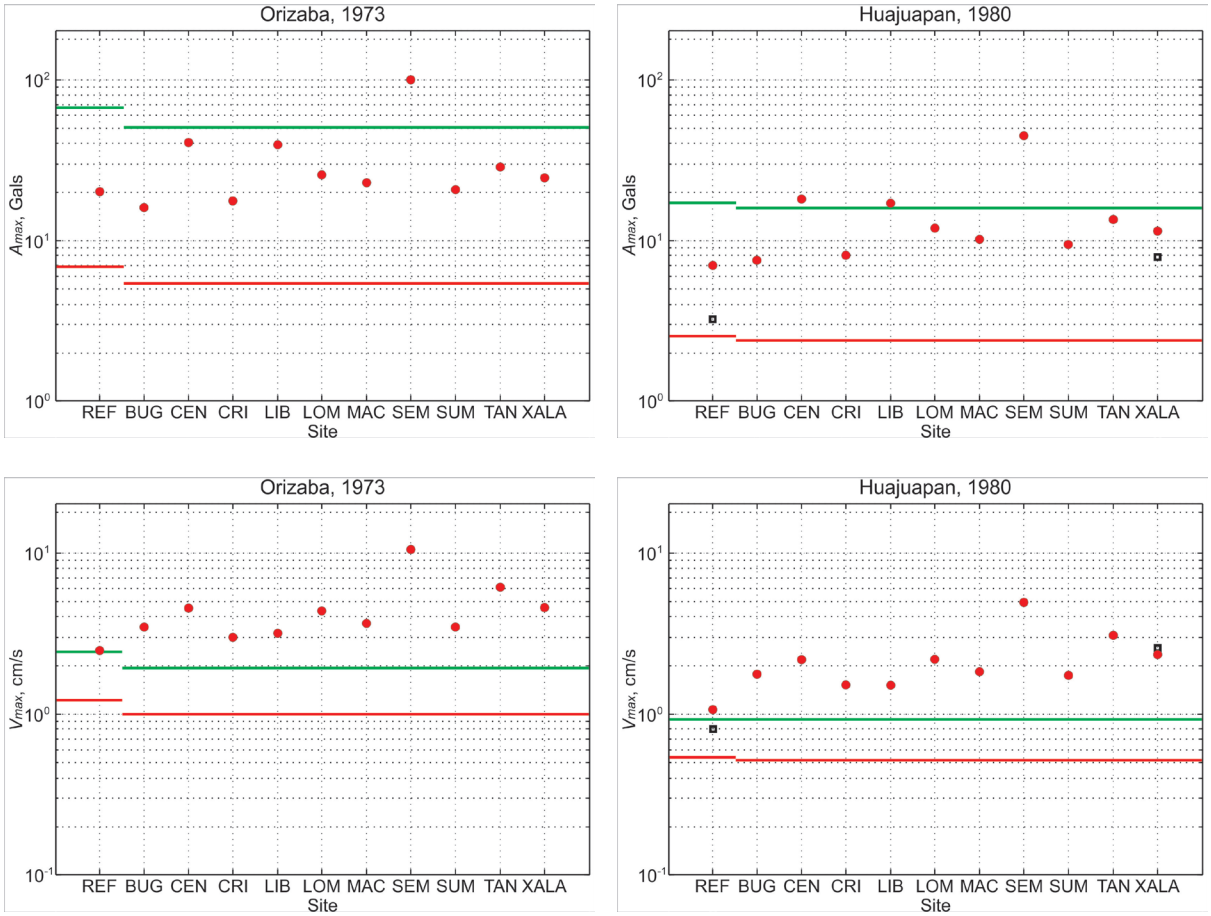

Discussion and Conclusions

A stochastic method was applied to estimate A_{max} and V_{max} in the city of Xalapa during some critical earthquakes of the last century. The calculations account for amplification of seismic waves due to site effect. A Brune ω^{-2} source model and a stress drop, $\Delta\sigma$, of 50 bar was assumed to estimate A_{max} in Xalapa during the shallow, crustal 1920 Xalapa earthquake (M_w6.4). The present estimates of A_{max} range between 100 and 250 cm/s^2 reaching approximately 300 and 600 cm/s^2 at two locations with the largest site effect. The estimated V_{max} values are between 10 and 20 cm/s except at the location of the largest site effect where it is ~ 40 cm/s. When ignoring the site effect the model yields A_{max} and V_{max} of 38 cm/s^2 and 3 cm/s, respectively. Thus the site effect amplifies A_{max} and V_{max} by a factor of ~ 2.5 to 6 at most locations but by ~ 15 at one site.

The parameters used in the estimation of ground motion during the 1920 earthquake are not constrained by data, since no recording of local, crustal earthquakes in Xalapawere available. The peak ground motions are critically dependent on stress drop. For example, A_{max} and V_{max} values for $\Delta\sigma$ = 30 and 100 bar are about half and twice those for $\Delta\sigma$ = 50 bar. A stress drop between 30 and 100 bar is probably reasonable for crustal earthquakes in the TMVB. If so, then Figure 8 summarizes the corresponding range of A_{max} and V_{max} values which may have occurred during the 1920 earthquake.

The estimated peak ground motions from the intraslab earthquakes are expected to be reliable (within a factor of about 2) since a better control on average stress drop was available from a previous study (García *et al*., 2004). There is also some validation of other input parameters used in the application of the stochastic method. It comes from the Xalapa recordings of an M_w5.7 intraslab earthquake and simulation of ground motions using these traces as empirical Green's functions. Median A_{max} and V_{max} of ~ 30 cm/s^2 and 4 cm/s, respectively were estimated in Xalapa during the 1973 Orizaba and 1999 Tehuacán earthquakes; the corresponding values during the 1980 Huajuapan earthquake are ~ 10 cm/

s^2 and 2 cm/s. In the isoacceleration map of the 1999 earthquake, Xalapa falls between the contours of 20 and 40 cm/s^2 (Singh *et al*., 1999), which agrees with the present estimation of A_{max}. From the range of A_{max} and V_{max} at sites in Xalapa shown in Figure 11 and GMICE by Wald *et al*. (1999), the estimated MMIs for the 1973 and 1999 earthquakes are IV-V while for the 1999 earthquake it is III-IV. These intensities are lower than MMI of VI reported by Figueroa (1974) for the 1973 earthquake and VI estimated by Yamamoto *et al*. (1984) for the 1980 earthquake. The reason for this discrepancy, as in the case of the 1920 earthquake, probably arises from the fact that the GMICE developed from recent California data is not valid for the TMVB.

As previously reported for Laguna Verde, the seismic waves from intraslab earthquakes traversing through the mantle wedge before arriving Xalapa are expected to suffer relatively large attenuation. However, these waves amplify due to local site effect. It seems that in Xalapa the two effects, roughly, balance each other. As a consequence, the Ground Motion Prediction Equation, developed from data in the forearc region with lesser attenuation and at hard sites (García *et al.*, 2005), appears to work reasonably well for Xalapa.

The present study provides a rough estimation of peak ground motions in Xalapa during the scenario earthquakes considered above, and lays ground for their estimation during future postulated earthquakes. The large uncertainty in the estimations can only be mitigated by extensive recording of local and regional earthquakes in the city.

Acknowledgements

The authors acknowledge National Seismological Service (SSN), National Center for Disaster Prevention (CENAPRED) and Institute of Geophysics, UNAM, for providing seismic equipment which was deployed in the field. In particular, we are grateful to Dr. Juan Manuel Espíndola Castro and the people who facilitated the sites where seismic stations were temporarily installed. DEGTRA, a software package developed by Dr. Mario Ordaz, was extensively used in the analysis of the data. LVIG data was obtained by the SSN technical personnel as well as station maintenance, data acquisition and distribution. Seismic data provided by the Strong Ground Motion Database System (http://aplicaciones.iingen.unam.mx/AcelerogramasRSM/) have been the product of the instrumentation and processing work of the Seismic Instrumentation group at the Instituto de Ingeniería of the National Autonomous University of Mexico (UNAM), as well as its Information Technology (IT) infrastructure. This work was supported by CONACYT project 255598.

References

Abe K., 1981, Magnitude of large shallow earthquakes from 1904 to 1980. *Phys. Earth. Planet. Interiors*, 27, 72-92.

Anderson J., Hough S., 1984, A model for the shape of the Fourier amplitude spectrum of acceleration at high frequencies. *Bull. Seism. Soc. Am.*, 74, 1969-1993.

Barrera D.T., 1931, El temblor del 14 de enero de 1931. *Reporte Instituto de Geología*, Universidad Nacional Autónoma de México, 40 p.

Boore D.M., 1983, Stochastic simulation of high-frequency ground motions based on seismological models of the radiated spectra. *Bull. Seism. Soc. Am.*, 73, 1865-1894.

Boore D.M., 2003, Simulation of ground motion using the stochastic method. *Pageoph*, 160, 635-676.

Brune J.N., 1970, Tectonic stress and the spectra of seismic shear waves from earthquakes. *J. Geophys. Res.*, 75, 4997-5009.

Cartwright D.E., Longuet-Higgins M.S., 1956, The statistical distribution of the maxima of a random function. *Proc. R. Soc. London*, 237, 212-232.

Córdoba-Montiel, F., 2010. Simulación del movimiento del suelo en la ciudad de Xalapa durante el temblor del 3 de enero de 1920 (*M*~6.4). Tesis de Maestría, p. 112, Posgrado en Ciencias de la Tierra, Universidad Nacional Autónoma de México, México D.F.

Figueroa J., 1970, Catálogo de sismos ocurridos en la República Mexicana: México, D.F., Instituto de Ingeniería, UNAM, 272, 88 p.

Figueroa J., 1974, Sismicidad en Puebla, Macrosismo del 28 de agosto de 1973: México, D.F., Instituto de Ingeniería, UNAM, 343, 64 p.

Flores T., Camacho H., 1922. Memoria relativa Terremoto Mexicano del 3 de Enero de 1920. *Boletín del Instituto Geológico de México*, 38, 107 p.

García Acosta V., Suárez Reynoso, G., 1996, Los sismos en la historia de México. Tomo I. FCE, UNAM, CIESAS, México, 718 p.

García D., Singh S.K., Herráiz M., Pacheco J.F., Ordaz M., 2004, Inslab earthquakes of central Mexico: Q, source spectra and stress drop. *Bull. Seism. Soc. Am.*, 94, 789-802.

García D., Singh S.K., Herráiz M., Ordaz M., Pacheco J.F., 2005, Inslab earthquakes of central Mexico: peak ground-motion parameters and response spectra. *Bull. Seism. Soc. Am.*, 95, 2272-2282.

González-Ruiz J., 1986, Earthquake source mechanics and tectonophysics of the Middle America subduction zone in Mexico. Ph. D. Thesis, University of California at Santa Cruz.

Hanks T.C., McGuire R.K., 1981, The character of high-frequency strong ground motion. *Bull. Seism. Soc. Am.*, 71, 2071-2095.

Herrmann R.B., 1985, An extension of random vibration theory estimates of strong ground motion at large distances. *Bull. Seism. Soc. Am.*, 75, 1447-1453.

Johnson C.A., Harrison C.G.A., 1989, Tectonics and volcanism in Central Mexico: A landsat thematic mapper perspective. *Remote Sens. Environ.*, 28, 273-286.

Jiménez Z., Ponce L., 1978, Focal mechanism of six large earthquakes in northern Oaxaca, Mexico, of the period 1928-1973. *Geofísica Internacional*, 17, 379-386.

Johnson C.A., Harrison C.G.A., 1990, Neotectonics in Central Mexico. *Phys. Earth Planet. Int.*, 64, 187-210.

Lermo J., Chávez-García F.J., 1993, Site effect evaluation using spectral ratios with only one station. *Bull. Seism. Soc. Am*., 5, 1574-1594.

Ordaz M., Singh S.K., Reinoso E., Lermo J., Espinosa J.M., Domínguez T., 1988, Estimation of response spectra in the lake-bed zone of the Valley of Mexico. *Earthquake Spectra*, 4, 815-834.

Ordaz M., Arboleda J., Singh S.K., 1995, A scheme of random summation of an empirical Green´s function to estimate ground motions from future large earthquakes. *Bull. Seism. Soc. Am.*, 85, 1635-1647.

Singh S.K., Wyss M., 1976, Source parameters of the Orizaba earthquake of August 28, 1973. *Geofísica Internacional*, 16, 165-184.

Singh S.K., Havskov J., Astiz L., 1981, Seismic gaps and recurrence periods of large earthquakes along the Mexican subduction zone, *Bull. Seism. Soc. Am.*, 71, 827-843.

Singh S.K., Apsel R., Fried J., Brune J.N., 1982, Spectral attenuation of SH waves along the Imperial fault. *Bull. Seism. Soc. Am.*, 72, 2003-2016.

Singh S.K., Rodríguez M., Espíndola J.M., 1984, A catalog of earthquakes of Mexico from 1900 to 1981. *Bull. Seism. Soc. Am.*, 74, 267-279.

Singh S.K., Suárez G., Domínguez T., 1985, The great Oaxaca earthquake of 15 January 1931: Lithosphere normal faulting in the subducted Cocos plate. *Nature*, 317, 56-58.

Singh S.K., Lermo, Domínguez T., Espinosa J.M., Mena E., Quaas R., 1988, The Mexico Earthquake of September 19, 1985—A Study of Amplification of Seismic Waves in the Valley of Mexico with Respect to a Hill Zone Site. *Earthquake Spectra*, 4, 4. pp. 653-673. https://doi.org/10.1193/1.1585496

Singh S.K., Ordaz M., Pacheco J.F., Quaas R., Alcántara L., Alcocer S., Gutiérrez C., Meli R., Ovando E., 1999, A preliminary report on the Tehuacán México earthquake of June 15, 1999 (M_w = 7.0). *Seism. Res. Lett.*, 70, 489-504.

Singh S. K., Mohanty W., Bansal B.K., Roonwal G.S., 2002, Ground motion in Delhi from future large/great earthquakes in the central seismic gaps of the Himalayan arc, *Bull. Seism. Soc. Am.*, 92, 555-569.

Singh S.K., Pacheco J.F., García D., Iglesias A., 2006, An estimate of shear-wave Q of the mantle wedge in Mexico. *Bull. Seism. Soc. Am.*, 96, 176-187.

Singh S.K., Iglesias A., García D., Pacheco J.F., Ordaz M., 2007, Q of Lg waves in the Central Mexican Volcanic Belt. *Bull. Seism. Soc. Am.*, 97, 1259-1266.

Singh S.K., Iglesias A., Ordaz M., Pérez-Campos X., Quintanar L., 2011, Estimation of Ground Motion in Mexico City from a Repeat of the M~7.0 Acambay Earthquake of 1912. *Bull. Seism. Soc. Am.*, 101, 2015-2028.

Suárez G., Ponce L., 1986, Intraplate Seismicity and Crustal Deformation in Central Mexico (resumen). *EOS Trans. Am. Geophys. Union*, 67, 1114.

Suárez G., 1992, El sismo de Jalapa del 3 de enero de 1920. *Rev. Mex. de Ing. Sísmica*, 42, 3-15.

Suárez G., García Acosta V., Gaulon, R., 1994, Active crustal deformation in the Jalisco block, Mexico: evidence for a great historical earthquake in the 16th century. *Tectonophys*, 234, (1), 117-127.

Suter M., 1991, State of stress and active deformation in Mexico and western Central America, in *Neotectonics of North America,* D.B. Slemmons, *et al.* (Editors), Geological Society of America, Boulder, Colorado, Decade Map Vol. 1, 401-1421.

Suter M., Aguirre G., Siebe C., Quintero O., Komorowski J.C., 1991, Volcanism and Active Faulting in the Central Part of the Trans-Mexican Volcanic Belt, Mexico, in *Geological Excursions in Southern California and Mexico*, M.J. Walawender and B.B. Hanan (Editors), Geological Society of America, Boulder, Colorado, Guidebook, 1991 Annual Meeting, 224-243.

Suter M., Carrillo-Martínez M., Quintero-Legoretta O., 1996, Macroseismic study of shallow earthquakes in the central and eastern parts of the trans-Mexican volcanic belt, Mexico. *Bull. Seism. Soc. Am.*, 86, 1952-1963.

Suter M., López-Martínez M., Quintero Legorreta O., Carrillo-Martínez M., 2001, Quaternary intra-arc extension in the central Trans-Mexican Volcanic Belt. *GSA Bulletin*, 113, 693-703.

Trifunac M.D., Brady A.G., 1975, On the correlation between seismic intensity scales with the peaks of recorded ground motions. *Bull. Seism. Soc. Am.*, 65, 139-162.

UNAM Seismology Group, 2010, Intraslab Mexican earthquakes of 27 April 2009 (Mw 5.8) and 22 May 2009 (Mw 5.6): a source and ground motion study. *Geofísica Internacional*, 49, 153-163.

Urbina, F., Camacho, H., 1913, La zona megaseísmica Acambay-Tixmadejé Estado de México conmovida el 19 noviembre 1912. *Boletín del Instituto Geológico de México*, 32, 125 p.

Wald D.J., Quitoriano V., Heaton T.H., Kanamori H., 1999, Relationship between peak ground acceleration, peak ground velocity, and modified Mercalli intensity in California. *Earthquake Spectra*, 15, 557-565.

Yamamoto J., Jiménez Z., Mota R., 1984, El temblor de Huajuapan de León, Oaxaca, México, del 24 de octubre de 1980. *Geofísica Internacional*, 23, 83-110.

Zoback M.L., Zoback M.D., Adams J., Bell S., Suter M., Suárez G., Jacob K., Estabrook C., Magee M., 1990, Stress map of North America, Continent-scale Map-005, Geological Society of America, Boulder, Colorado, Scale 1:5,000,000.

Geofísica Internacional (2018) 57-2: 107-120

Original paper

Stoneley Wave Predicted Permeability and Electrofacies Correlation in the Bangestan Reservoir, Mansouri Oilfield, SW Iran

Bahman Soleimani*, Mehrdad Moradi and Ali Ghabeishavi

Received: November 24, 2016; accepted: December 07, 2017; published on line: April 02, 2018

Resumen

La caracterización de los yacimientos es una de las metas más importantes para la explotación de los campos petroleros. Determinar la permeabilidad y el tipo de rocas es de primordial importancia para conocer la calidad del yacimiento. En este trabajo se utilizan las ondas de Stoneley a partir de herramientas sónicas bipolares para encontrar cambios de permeabilidad en el yacimiento Bangestan, del campo petrolero Mansouri. Se estimó el índice (tortuosidad) con ondas Stoneley. Despues de comparar la èrmeabilidad resultante de las ondas de Staneley, núcleos y el método Timur, se concluye que las tres permeabilidades son muy parecidas. La porosidad de los núcñeos y la porosidad efectiva obtenida del análisis de muestras de pozos fueron similares. El método de electrofacies (EF), como método de comparación, se utilizó para encontrar tipos de rocas que definieran las zonas internas y externas al yacimiento. Simultáneamente con la compactación EF, se consideraron e interpretaron datos de radiación gamma, porosidad neutrónica, densidad, sonar, saturación de agua y porosidad de 78 pozos. Como resultado del análisis se definieron 9 cúmulos, que después de considerar datos de presión capilar (CP) se redujeron a 4. Los cúmulos 1 y 2 presentan mayor porosidad. En EF 3 se observó mayor abundancia de fracturas y solutos comparado con las otras EFs. Basado en un tipo matricial se encontró la clasificación de porosidad Archie de tipos I y III. El tamaño del poro en EF 1 y 2 fue esencialmente del tipo B mientras que EF 3 fue del tipo A. Las EFs generadas y determinadas con ondas Stoneley y registros de datos de los pozos también se compararon presentando buena correlación.

Palabras clave: Ondas Stoneley, herramientas sónicas dipolares, yacimiento Bangestan, campo petrolero Mansouri, electrofacies.

Abstract

Reservoir characterization is one of the most important goals for the development of any oilfield. Determination of permeability and rock types are of prime importance to judge reservoir quality. In this research, Stoneley waves from dipole sonic tools were used in order to discover changes in permeability in the Bangestan reservoir, Mansouri oilfield.
Index (tortuosity) could be estimated by Stoneley waves. After comparing the permeability resulting from Stoneley waves, cores and the Timur method, it was concluded that all the three permeabilities were very similar. The core porosity and effective porosity from the analysis of well logs were found to match as well. Electrofacies (EF) method, as a clustering method, was utilized to find rock types in order to define reservoir and non-reservoir zones. Simultaneous with EF clustering, gamma ray, neutron porosity, density, sonic, water saturation and porosity (PHIE) data from 78 wells were also considered and interpreted. Nine clusters were defined as a result of the analysis, being reduced to only four clusters after applying PC (capillary pressure) data. Among the four clusters, clusters 1 and 2 contained more vuggy pores than the others. Fracture abundance and solution seams were observed more frequently in EF-3 as compared to other EFs. Based on the matrix type, Archie porosity classification types I and III were recognized. The pore sizes in EFs-1 and 2 were mostly of the B type while in EF-3, it was A type.
The EFs generated and determined by Stoneley waves and the well log data were also compared, showing a good correlation.

Key words: Stoneley wave, Dipole sonic tools, Bangestan reservoir, Mansouri oilfield, Electrofacies.

B. Soleimani*
Geology Dept.
Shahid Chamran University of Ahvaz,
Ahvaz, Iran.
*Corresponding author: soleimani_b@scu.ac.ir

M. Moradi
Geology Dept.
Shahid Chamran University of Ahvaz
Ahvaz, Iran.
Second add: National Iranian Drilling Company
Well Logging Operation
Ahvaz, Iran.

A. Ghabeishavi
Dept. of Developing Geology
National Iranian Oil Company
Ahvaz, Iran.

Introduction

Understanding the characteristics of any reservoir is of prime importance to the development of any oilfield. Accordingly, hydrocarbon interval and prediction of hydrocarbon production in each drilled well are vital for petrophysical study and their evaluation and also to pinpoint a new well in future drilling project.

The petrophysics study is extremely important to find out some key parameters such as reservoir permeability. Permeability and porosity are dependent upon the texture and rock fabric. Widespread changes in all types of porosity and variation in pore throat from the micron scale (up to 350 μm) to the nano-scale (below to 1-3 nm) (Eigmati *et al*., 2011; Josh *et al*., 2012; Ortega and Aguilera, 2014) are effective in quantifying the permeability (Gao and Hu, 2013). Pore throat variation is more effective in computing permeability as compared to the size of the pore itself. Moreover, pore throat can be reckoned by the size of the pore. The pore throat size and its distribution are important in many fluid transport processes (Lake, 1989; Anovitz and Cole, 2015), the fluid saturation distribution, porosity, permeability, and to some extent, wettability (Green, 2009) and seismic properties (Batzle and Wang, 1992; Malembo, 2015) or the properties of the entire rock mass as well (Collet and Gurevich, 2013) in reservoir rock.

There are several methods to estimate permeability (Anissofira, and Latief, 2015; Brown, 2015; Gupta and Maloney, 2015; Luijendijk, and Gleeson, 2015; Sadeq *et al*., 2015; Wang *et al*., 2016; Wei *et al*., 2015). Reservoir analysis and evaluation is dependent upon the characteristics of reservoir geology as well as the indication of the formation porosity and pore throat. The aim is to infer the petrophysical properties of the reservoir rock, gain awareness about parameters, and finalize the spatial map extent of the flow unit. Due to lack of adequate information from the reservoir, we are obliged to employ different methods to find the permeability. If permeability is found by any specific technique, almost all the parameters of the reservoir can be correlated and determined. Separation of rock types by different procedures is also useful to study the reservoir quality and sometimes the reservoir zoning of certain reservoirs. A full description of the reservoir requires a perfect combination of geological and petrophysical data so that the researchers can determine the characteristics of the reservoir as close as possible to the real geology (Abbaszadeh *et al*., 1996; Amaefule *et al*., 1993; Rebelle *et al*., 2009; Tiab and Donaldson, 2004).

Determining all rock types in a reservoir and the variation in characteristics in horizontal and vertical directions constitute one of the most important analyses in the process of characterizing a reservoir (Bagheri and Biranvand, 2006; Lucia, 2007; Serra, 1986; Serra and Abbott, 1982; Serra and Sulpice, 1975). To determine the rock type, it is necessary to use specific materials including the study of well logs with high resolution and the dynamic data in that specific direction. A simplified connection must also be created between the petrophysical data and the facies statistics (Rebelle *et al*., 2009). In definition, the rock type is a facies collection with distinguished criteria incorporated in one group (Schlumberger, 1989; Rabiller, 2005; Ye and Rabiller, 2000, 2005). In this paper, efforts have been made to utilize Stoneley waves in the Mansouri oilfield in Bangestan reservoir to estimate permeability data with high accuracy from Stoneley waves as electrofacies detection. This method has been applied by other researchers (Uspenskaya *et al*., 2012).

Mansouri oilfield position

Mansouri oilfield is located in Khuzestan province, southwest of Iran. Without any outcrop, this field has been defined by surface seismicity. The trend in the structure of this field is similar to the adjacent fields such as the Ahwaz, Maroun and Shadegan oilfields, following the Zagros trend (Fig. 1).

The oil field understudy consisted of different reservoirs such as Asmari, Bangestan and Khami. The Bangestan reservoir (Cretaceous age), divided into two parts: the Ilam (limestone and shale, Santonian-Campanian), and Sarvak (limestone, Cenomanian-Turonian) formations as the upper and lower reservoirs respectively. These reservoirs are separated due to the Lafan shale at the base of Ilam Formation. According to geophysical survey maps, the Mansouri structure is 43 km in length and 6 km wide from the top of Ilam Formation.

Methods

In the present paper, Stoneley wave and electrofacies were used to evaluate the reservoir quality and to give a comparison between all estimated permeability data and electrofacies in the Bangestan reservoir.

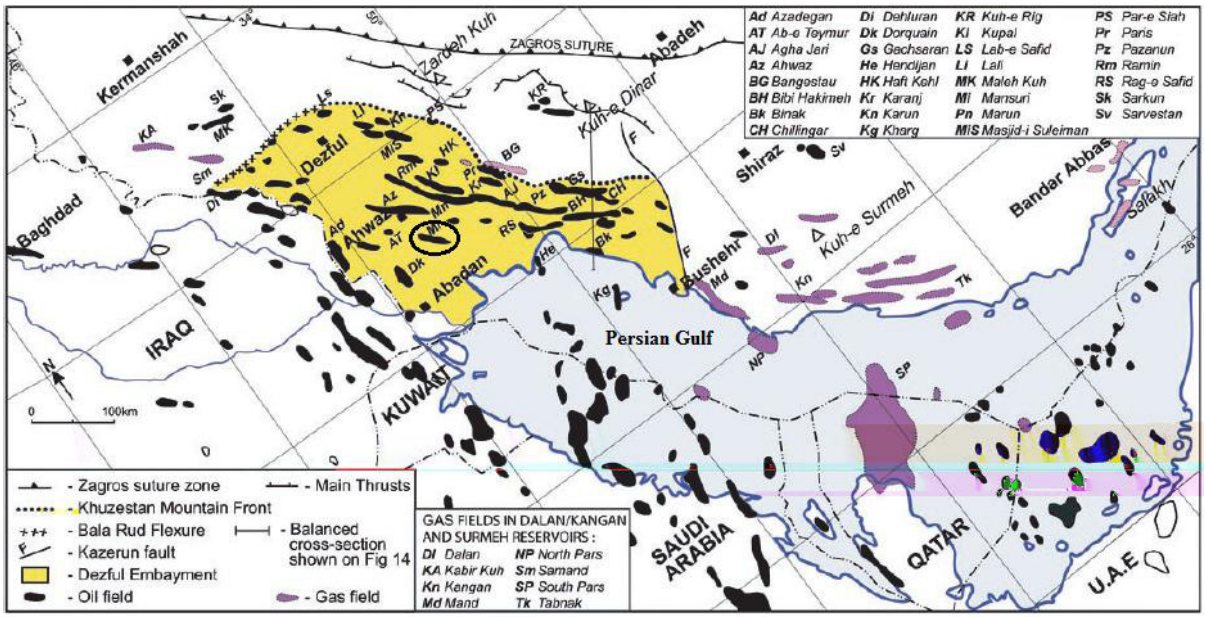

Figure 1. The Mansouri oilfield location map in the Zagros region (Bordenave & Hegre, 2005).

Stoneley waves are the type of sonic waves that are surface guided waveforms that propagate by "rolling" up the borehole wall. The Stoneley waveform has significant relevance in a number of applications although it can mask other waves due to its high amplitude. Other generated waveforms include borehole and surface guided waves typically formed by reverberation in the borehole. The Dipole sonic tools can fire the monopole transmitter at low frequency, specifically to generate Stoneley waves. These Stoneley waves can be used in fracture evaluation, for log quality control (LQC) dipole compression, and in shear waveforms studies. These waves exert pressure on the borehole wall and compress the formation fluids into porous media, creating a specific wave which is called Stoneley wave. In general, there are three types of waves including compression, shear and Stoneley, present in fast formations. However, only the compressional and Stoneley waves can be found in slow formations (Ellis and Singer, 2008).

In order to estimate permeability in slow formations, flexure waves are recorded by utilizing high technology logging tools that help finding permeability in slow formation reservoirs.

Dipole sonic tools use a directional source as well as directional receivers. The dipole source behaves like a piston, creating a pressure increase on one side of the borehole and a decrease on the other. This causes the borehole to flex. This flexing of the formation directly excites compressional and shear waves in the formation. Propagation of this flexural wave is parallel with the borehole, whereas displacement is at right angles to the borehole axis and in line with the transmitter. The source operates at a variety of low frequencies, 4 to 8 kHz standard dipole, 2 to 4 kHz medium frequency dipole, and 0.25 to 1 kHz low frequency dipole. The frequencies are chosen to optimize the excitation of the flexural waves in specific formations. The lower frequencies give optimum results in large boreholes and in very slow formations. In addition, the depth of investigation can be increased (Ellis and Singer, 2008).

The compressional and shear waves radiate straight out into the formation. There is, however, an additional shear/flexural wave propagating up the borehole. It creates a piston type (dipole-type) pressure disturbance in the borehole fluid. In fact, this pressure disturbance can be detected by the directional receivers. The shear/flexural wave, initiated by the flexing action of the borehole, is dispersive. At low frequencies, it travels at the same speed as the shear wave, but at higher frequencies it travels at a slower speed.

Advanced technology dipole sonic tools such as DSI, WSTT and XMAC are to be

utilized in order to estimate the permeability in all formations, which is called continuous permeability. The XMAC tool was used in the present study. In a situation where core samples are not taken in drilling wells, the permeability may be computed from dipole sonic logging tools. Moreover, core permeability measurements are reported point-to-point while dipole sonic permeability is a continuous process.

Stoneley waves are dispersive (velocity varies with frequency) and are generated from the interaction between borehole and formation (Fig. 2). At low frequencies, it is called a tube-wave. A Stoneley waveform has a frequency content of 0.1 to 3 kHz, with the highest amount of energy in late arrivals at about 500 Hz. Stoneley waves are usually detected between 0 to 20 ms on the sonic waveform. In contrast, the shear wave forms are usually detected between 0 to 5 ms and are concentrated around 4 kHz (Close *et al*., 2009).

Electrofacies analysis was carried out by thin sections, core analysis, and pressure capillary data (PC). The Electrofacies clustering of the Bangestan reservoir have been defined by all available data from 78 wells including GR, NPHI, RHOB, DT, SW and PHIE, which were simultaneously evaluated and interpreted.

Interpretation of well logs (Schlumberger, 1974) took a long time followed by applying the GEOLOG software with 91245 readings data and the self-organization map (SOM) technique (Vesanto, 1999). To study the electrofacies, 904 thin sections were prepared from those eletrofacies intervals. In order to decrease uncertainty during investigation, thin sections from the borderlines of each electrofacies were not considered during analysis. All the specifications of lithology and texture were studied using an optical microscope. Coring sample operation was carried out at 7 wells including 1, 4, 14, 24, 44, 54 and 96. The core samples of 3 of these drilled wells (14, 25 & 44) were subjected to SCAL analysis.

Discussion

There are different factors that affect the Stoneley wave. Its slowness increases due to fluid movement in porous media as well as the mud cake around the borehole. The mud cake effect on slowness is usually a constant shift if the mud cake thickness is constant or of one type. Grain modulus is another major factor affecting the Stoneley wave slowness. If the lithology is changing from pure calcite to dolomite or to more siliciclastic, the effect on slowness will be varied. The pore fluid modulus is also affected. For instance, if the fluid is changing from liquid to gas, the

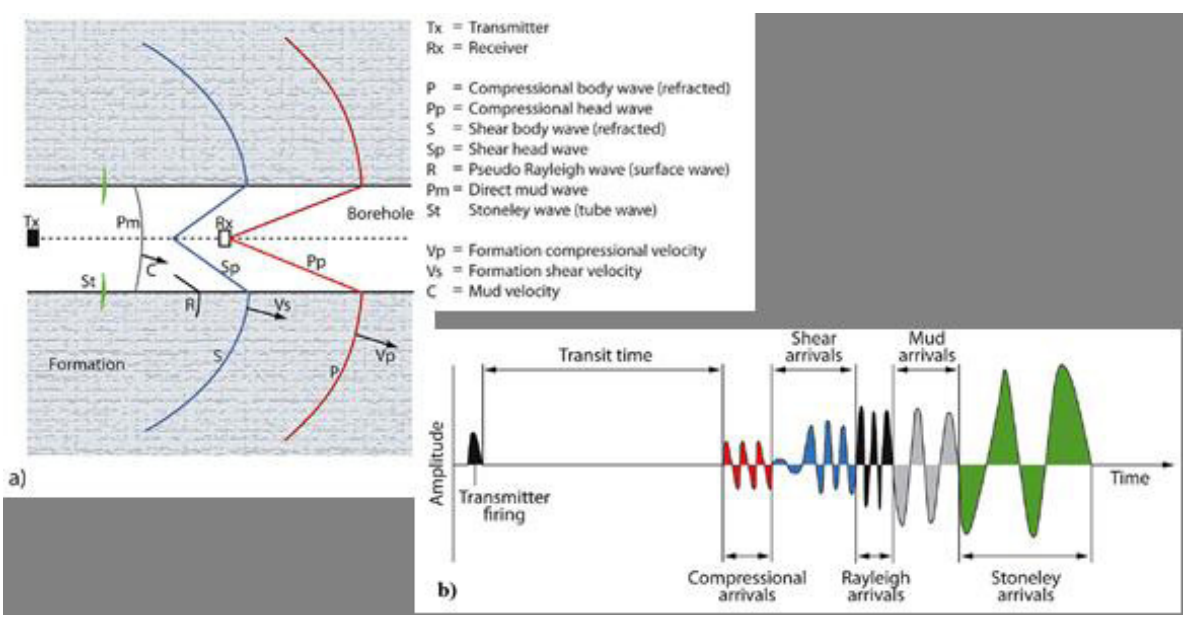

Figure 2. a) Important sonic waveform component propagation in a borehole as the P wave energy is detected; b) Schematic of the wave train detected at the receiver as a function of time (Close *et al*., 2009).

predicted permeability increases exponentially. A Stoneley wave is affected by porous media fluid and by shear modulus at low frequency. Stoneley wave slowness can be modeled in non-permeable zones (AL-Adani and Barati, 2003; Winkler *et al*., 1989) as follows:

$$DTST^2 = DTMF^2 + (DTSH^2 \times MFD)/RHOB$$

where

DTST = Stoneley wave slowness (μs/ft), DTSH= Shear wave slowness (μs/ft), DTMF= Mud filtrate slowness (μs/ft), MFD= Mud filtrate density (μs/ft), and RHOB= Density of the rock (g/cc).

By cross-plotting $DTST^2$ versus $DTSH^2/RHOB$ across a zero permeability zone, the slope of the straight line is MFD and the Y-intercept is $DTMF^2$ (AL-Adani and Barati, 2003). There must be one pattern on the linear fit plot: all data on the cross plot should be above or on the fitted line (Figure 3). This essential factor is observed in the present data.

The Stoneley permeability index is estimated by taking the ratio of actual measured Stoneley slowness and modeled slowness as per the above model. The formula can be written as follows:

$$KIST = DTST/\sqrt{[(DTSH^2 \times MFD/RHOB) + DTMF^2]}$$

This KIST model is still affected by variations in mud cake and formation fluid type. In addition, it does not provide a means to estimate mobility or permeability magnitude directly. Stoneley permeability index is not considered as the permeability estimation but it is an index of fluid movement in porous media around the borehole, since fluid movement is a function of pore throat distribution, pore shape, and pore size. Therefore the Stoneley permeability index is a tortuosity index only. These factors can be combined in a concept called Flow Zone Index (FZI). In fact, the Stoneley permeability index KIST is a direct measurement of FZI (Winkler *et al*., 1989):

$$FZI \; \alpha \; KIST$$

Since FZI approaches zero when the Stoneley permeability index approaches 1 in non-permeable zones and vice versa, and both of them approach infinity when permeability approaches infinity, then a simple relationship can be derived between FZI and STI, as follows (Wu and Yin, 2010):

$$FZI \; \alpha \; (1 - KIST)$$

$$FZI = IMF \; (KIST - 1)$$

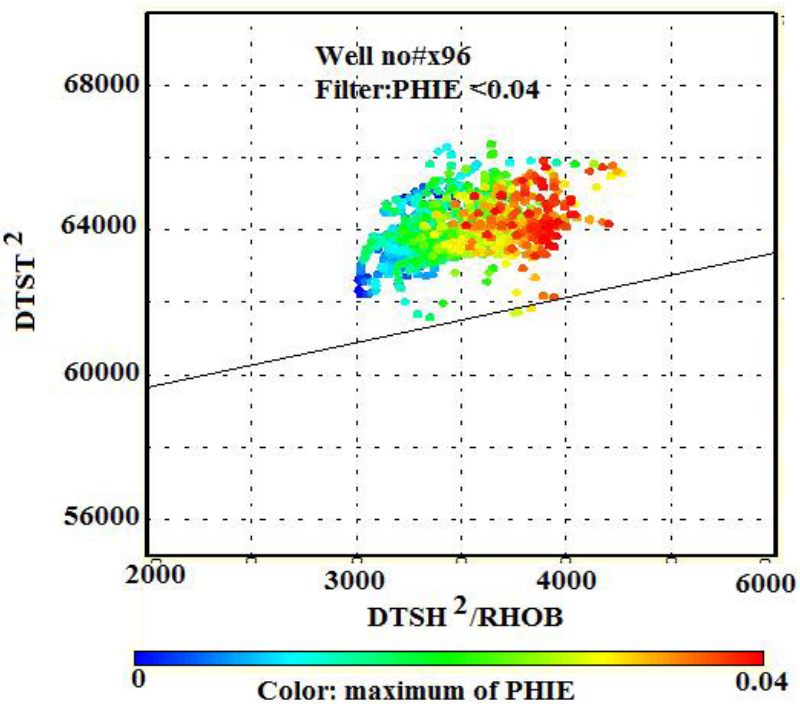

Figure 3. $DTST^2$ versus $DTSH^2/RHOB$ plot, the slop of the straight line is MFD and Y-intercept is $DTMF^2$

where:

FZI= Flow zone index

IMF= Flow zone index matching factor.

With this equation, the only empirical factor to match the actual permeability profile is IMF. Due to the effect of the grain modulus on Stoneley slowness, IMF can be computed in the probabilistic model by summing the volume weighted IMF for each individual mineral in the model:

$$IMF=\sum (IMFi.Vi).$$

The Stoneley permeability can be computed by using effective porosity and FZI according to the following equation (Amaefule *et al*., 1993):

$$K=1014.\ FZI^2.\ (\varphi^3/(1-\varphi)^2)$$

where:

K or KST: Permeability from Stoneley

method (md)

φ = Effective porosity

FZI= Flow zone index.

To conduct this method and get the effective data, the following conditions should exist:

-Single phase fluid should exist in porous media.

-Temperature variation is negligible.

-Mud type cake should be single with fairly constant mud cake thickness.

-Sufficient logs should be available for volumetric lithology modeling.

In the present area under study, core data, MDT permeability or down hole production profile with constant draw down are available. However, in bad holes or severely rough surface conditions, this method is not valid.

Timur permeability

Permeability can be estimated in several ways one of the commonest of which is the Timur Equation (Timur, 1968):

$$K= 0.136\ (\varphi^{4.4}/Sw_{ir}^{2})$$

By applying this method, Timur permeability estimation can be compared with core and Stoneley permeability, which are identical (Figure 4). The measured permeability from core analysis and estimated permeability of Stoneley method are also showing the best match. In this figure, a relationship is observed among fluid saturation, water saturation, oil saturation, EF, PHIE and PHI-core, and Stoneley predicted permeability variation. As shown in the figure, EFs-1 and 2 containing higher oil saturation, and in other electrofacies, Sw values are high. Therefore, EFs-1 and 2 have the best quality in this reservoir.

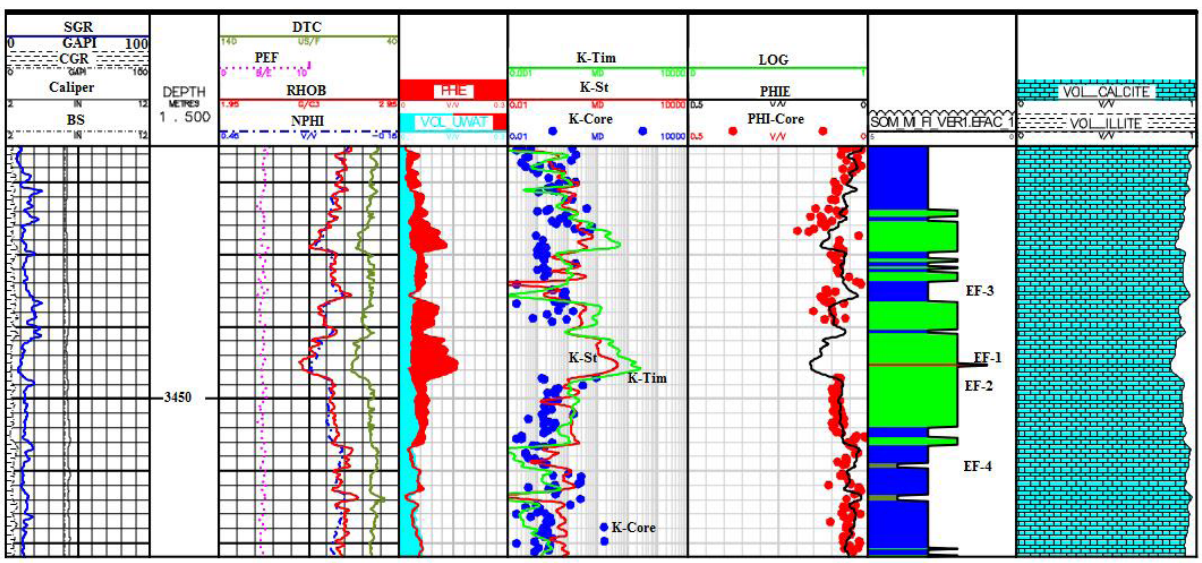

Figure 4. The comparison of permeability (K) data calculated from core analysis, Stoneley and Timur methods in one of the studied wells (Well#X96).

In order to differentiate reservoir zones from non-reservoir zones in the Bangestan field, all necessary data such as well logs, core samples, microscopic thin sections and geology software were used to determine electrofacies. All data were classified in 9 clusters by the SOM method. These rock types are plotted in the Bangestan reservoir in view of Sw vs PHIE (Figure 5). In general, capillary pressure (PC) is defined as the movement of fluids into pore throat and displacement of wetting fluids inside the pores (Jennings, 1987).

If the reservoir wetting fluid is constant, and supposing the size of pore remains the same, then capillary pressure will not change due to displacement of fluids. Therefore, by considering PC and water saturation data, it can be possible to combine some of the electrofacies together. According to the similarity of clusters and their combination, the 9 clusters were reduced to 4 clusters as the final clustering in the Bangestan reservoir of the Mansouri oilfield.

Electrofacies characterization

Petrophysical data average has been provided for each eletrofacies (Table 1) as GR, DT, neutron porosity, density, PHIE and Sw (Table-1). Statistical percentage of each electrofacies in this reservoir was plotted to present their frequencies (Figure 6A).

With respect to the electrofacies' depth and thickness, their distributions were analysed statistically. Comparison of electrofacies from a textural point of view clearly proved the fact that all electrofacies in the Bangestan reservoir consisted mainly of wakestone and packstone (Figure 6B). However, grainstone, dolostone and mudstone were also found in minor frequencies.

Drilling core analysis (Nelson, 2001) and Archie pore type classification (Archie, 1952) were applied to evaluate the reservoir quality. The study of core samples indicated that matrix porosity consisted of types I and III. The dominant porosity of EFs-1 and 2 is type B (visible by loop), EF-3 is type A (invisible porosity) and then followed by types B and D (vuggy and fracture porosity) in decreasing order. Most of the solution seems to have been found in EFs- 3 and 4. However, it is less frequent in EFs-1 and 2 (Figure 6C). This research has shown that vuggs are responsible for high reservoir quality in EFs-1 and 2 (Figure 7).

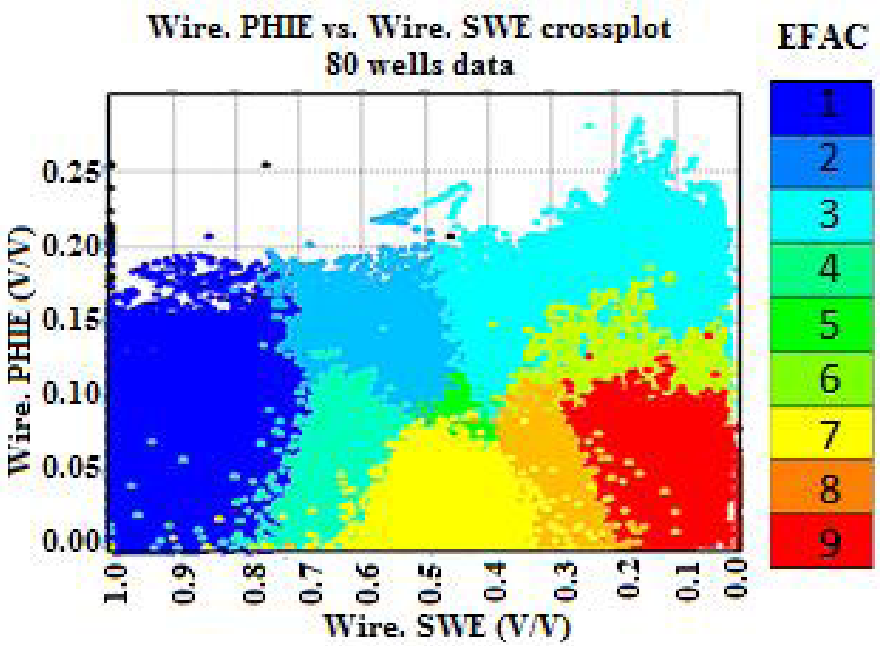

Figure 5. Presentation of the relation of nine EFs distribution in view of Sw and PHIE.

Table 1. The Petrophysical data average for four EFs in Bangestan Reservoir.

Electrofacies	GR °API	DT µs/f	Neutron porosity v/v	Density g/cc	PHIE v/v	Sw v/v
1	16.2	71	0.17	2.4	0.18	0.2
2	18.45	62	0.10	2.5	0.10	0.42
3	24.53	54	0.04	2.60	0.05	0.35
4	34.48	60	0.08	2.63	0.02	0.93

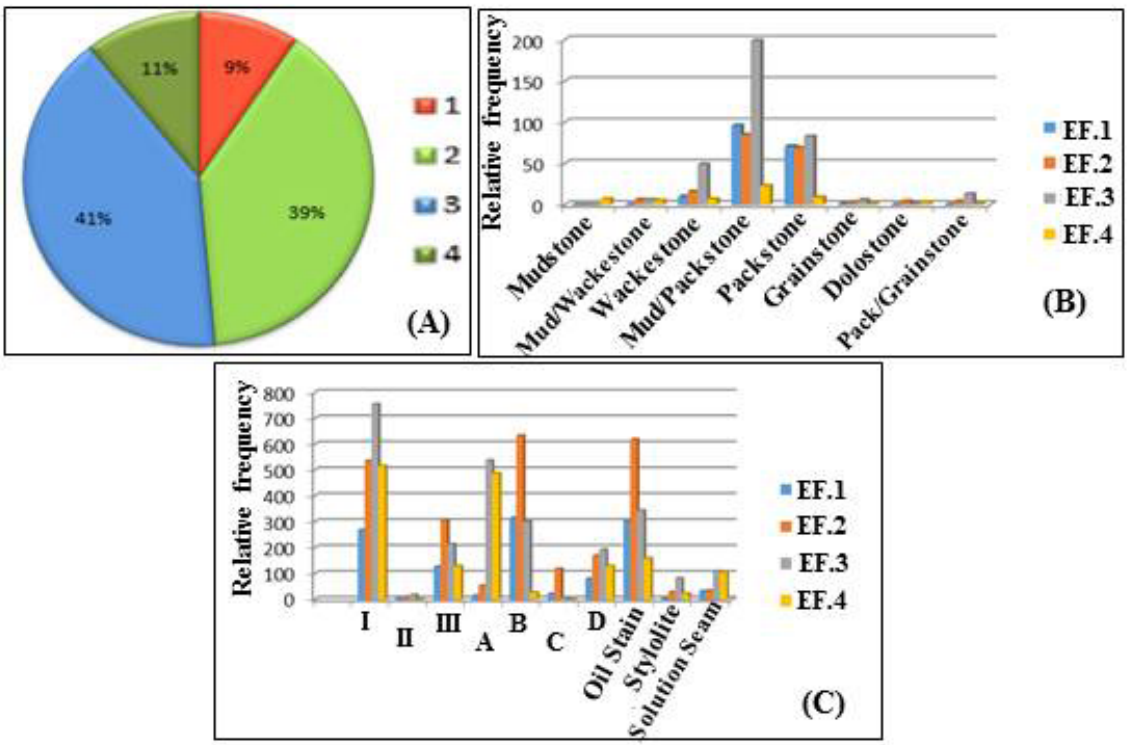

Figure 6. (A) The relative percentage of each electrofacies; B) Dunham textural variations and their distribution and C) The porosity type distribution based on Archie classification in all electrofacies of the Bangestan reservoir.

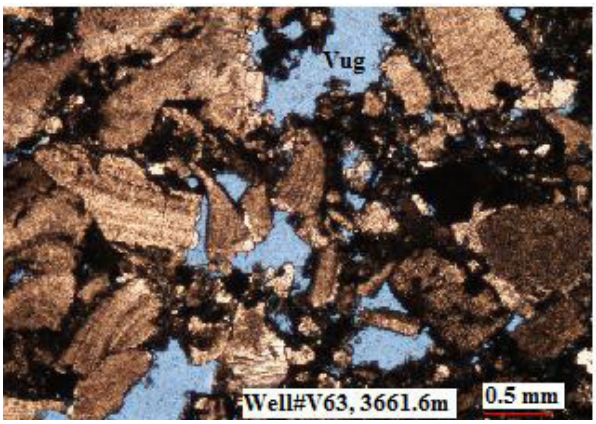

Figure 7. The presence of vuggy porosity type is the main reason of high reservoir quality.

Electrofacies from well logs and Stoneley wave

EFs determined from Stoneley and well logs in Well # C150 were compared and presented a good correlation between them (Figure 8). However, differences are observed between these methods as well. The differences can be attributed to the higher resolution of EFs according to Stoneley wave rather than EFs by GEOLOG using well log data in some horizons (upper part).

As observed in this figure, EFs distribution is different from other plots related to heterogeneity and scarcity patterns in the reservoir. This issue can be controlled by lateral facies changes or diagenetic intensity such as dolomitization. Therefore, some caution should be exercised in field development programs.

Permeability variation compared to Electrofacies

To check the permeability data of core and Stoneley wave, the results of well # X96 (where core data and dipole sonic data were available), due to its special position, were compared and a harmonic and uniform pattern in variation was observed (Figure 4). Permeability estimated by the Timur method also indicated a reaseaonable match. The effective porosity also shows a direct relation with the permeability (Figures 9-11). The porosity changes are also showing the same impacts on all K-plots, Stoneley, core, and Timor. This has been verified in different wells.

The permeability predicted by the Stoneley and Timor methods and the core data were

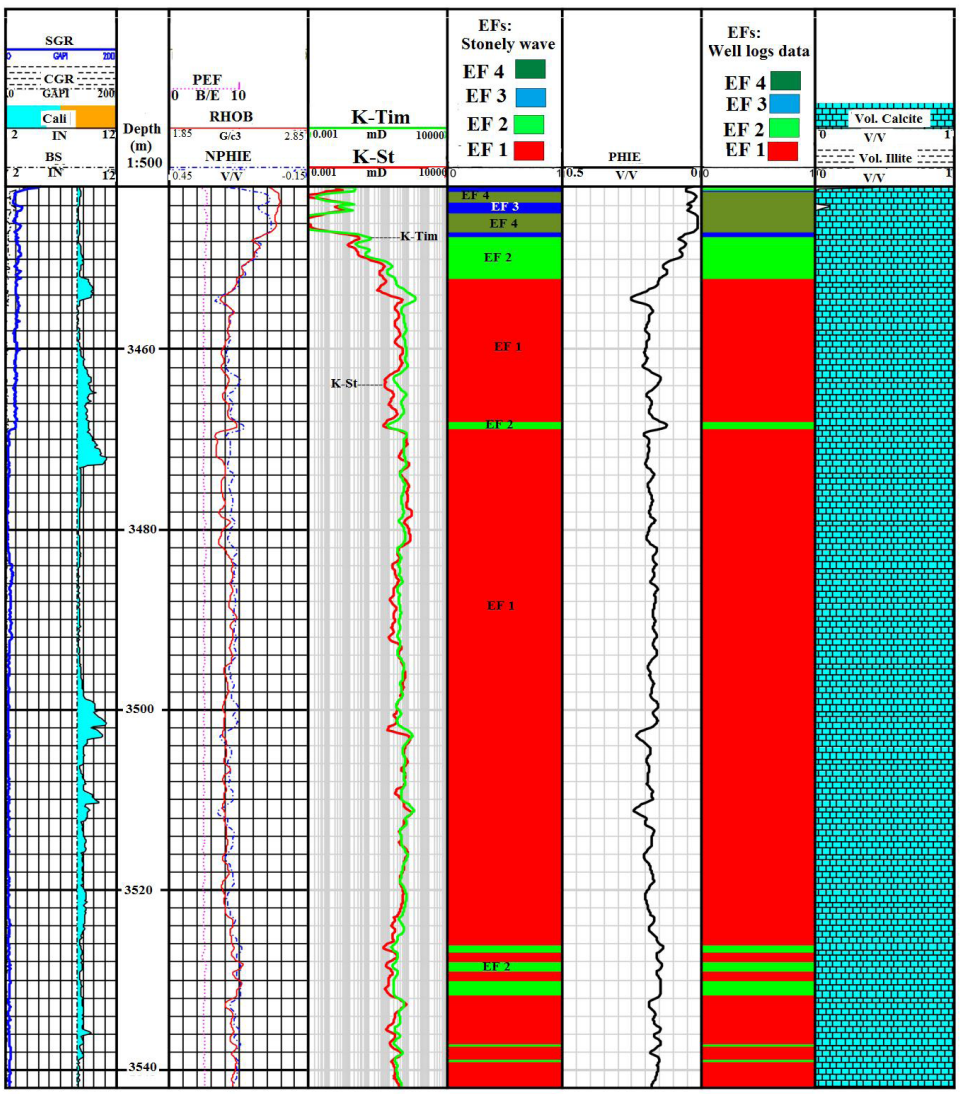

Figure 8. The comparison of EFs from Stoneley and EFs from well logs in Well# C150.

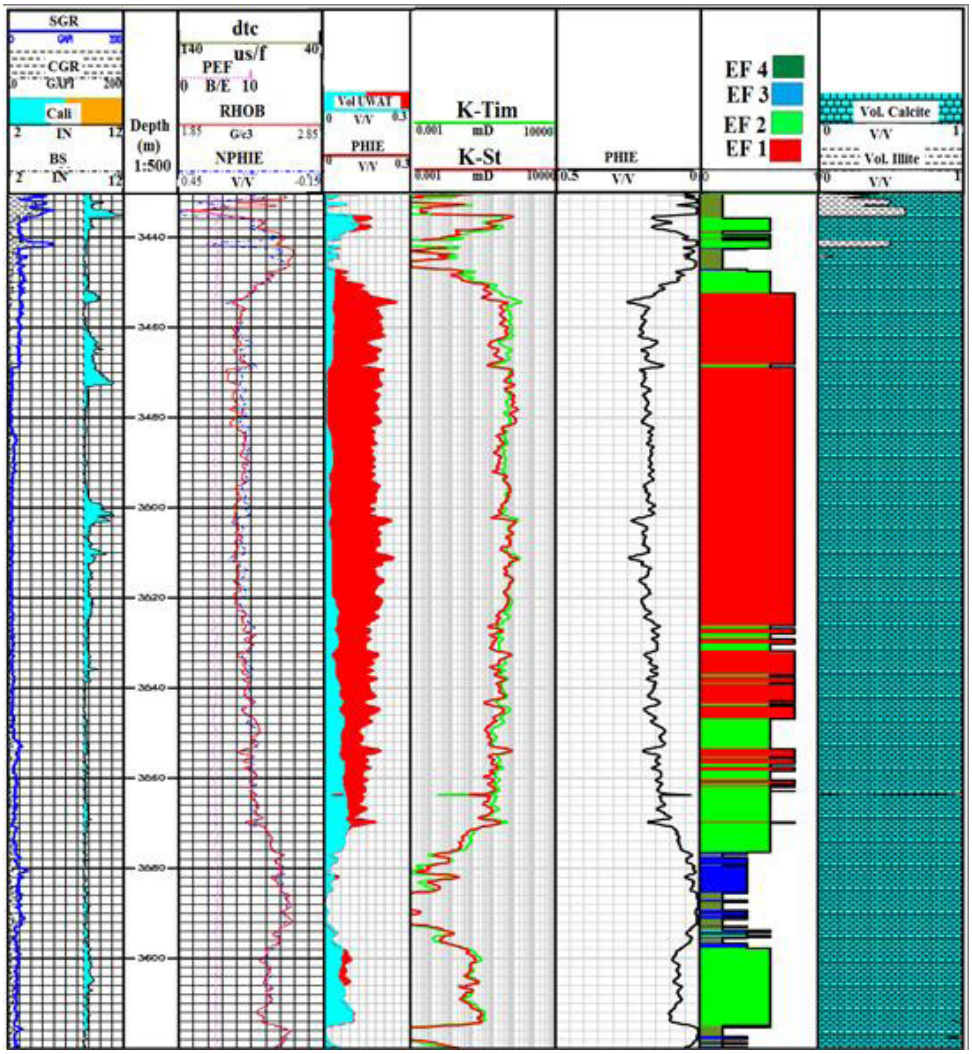

Figure 9. The comparison of K- ST and K- TIM permeabilities with EFs in Well#XY54.

also considered in all electrofacies. The study revealed that EFs 1, 2, and 3 can be classified as very good in quality but EF4 should be reagrded as a non reservoir zone. The permeabilty predicted by Stoneley wave emphasized the same results. Therefore, those horizons or rock types with high permeability values by either core, Timor or Stoneley can be recognized immediately. Thus the Stoneley wave method can be used as an alternative tool to predict the permeabiltsy of the horizons in the wells in which the core process is not successful or has not been run. This wave can also be employed to differentiate the rock type or electrofacies in high resolution and to evaluate the reservoirs (Figure 8). The ranges of predicted Stoneley permeabilty may be suggested to recognize the electrofacies in the Bangestan reservoir of Mansouri oilfield (Table 2).

Table 2. Detected electrofacies (EFs) and correlated to predicted Stoneley permeability.

EFs	Stoneley permeability relatively range (mD)
1	> 10
2	0.1-10
3	0.01-0.1
4	0-0.01

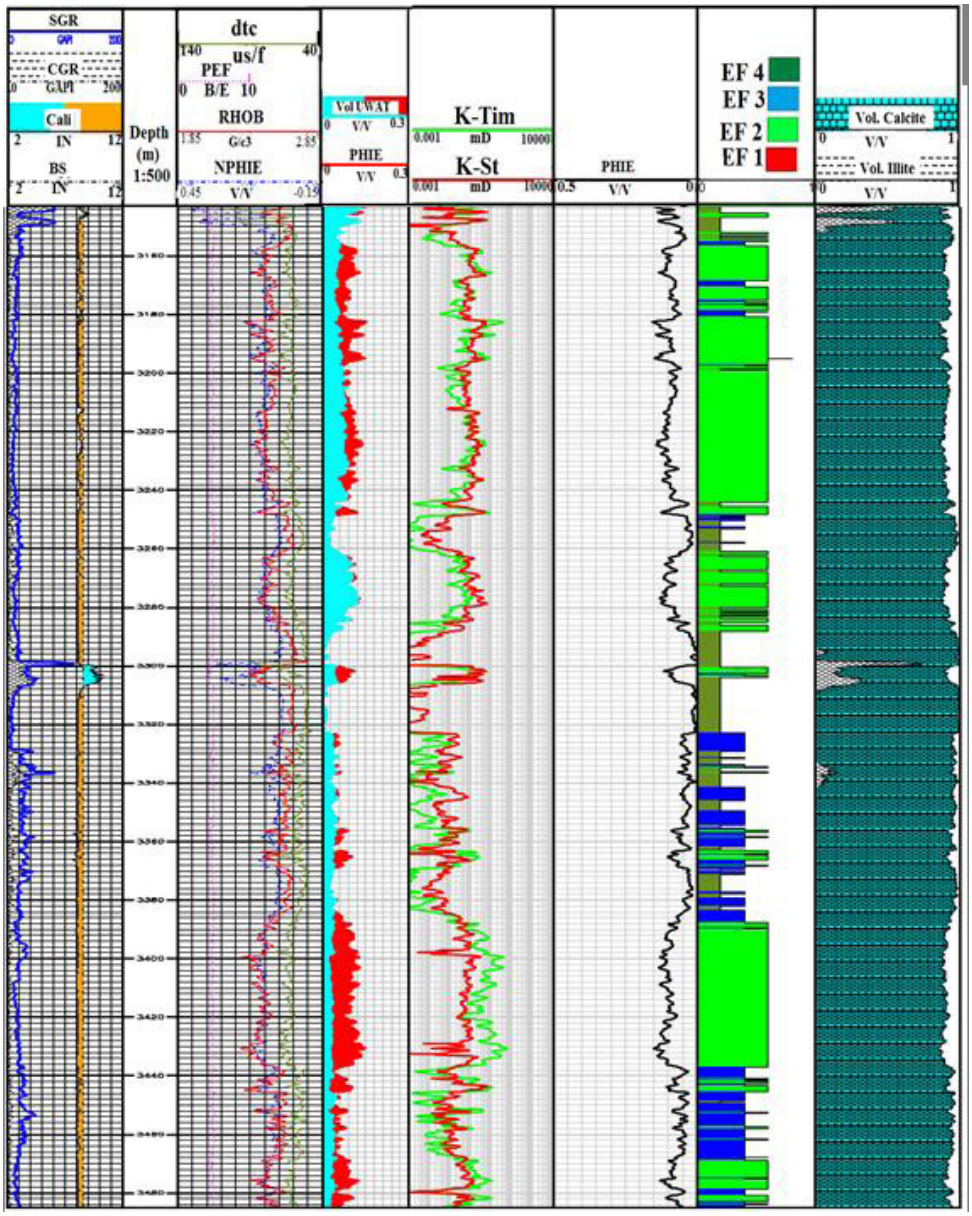

Figure 10. The comparison of K- ST and K- TIM permeabilities with EFs in Well#Z90.

Conclusions

Analysis and application of Stoneley waves as a unique way to predict reservoir permeability and its comparison with other provided electrofacies constitute the main goals of the present study. These were used to characterize the reservoir of Bangestan in the Mansouri oilfield, SW Iran. Comparison of the predicted Stoneley permeability logs with the core permeability indicated that they are in close match with each other. Due to the lack of core data in some wells, dipole sonic logs as an alternative tool can be substituted in order to estimate the permeability.

To find and separate heterogeneity of the reservoir in the Bangestan, electrofacies classification was used based on gamma ray, density, neutron, sonic, water saturation and PHIE data. A single model was given for the 78 wells studied. In this model, 4 electrofacies were summarized and recognized. EFs-1, 2 and 3 are showing very good to moderate reservoir quality and also with decreasing order. EF-4 was considered as a non-reservoir facies. The reason for high permeability in EFs-1 and 2 is attributed to the existence of abundances of vuggs.

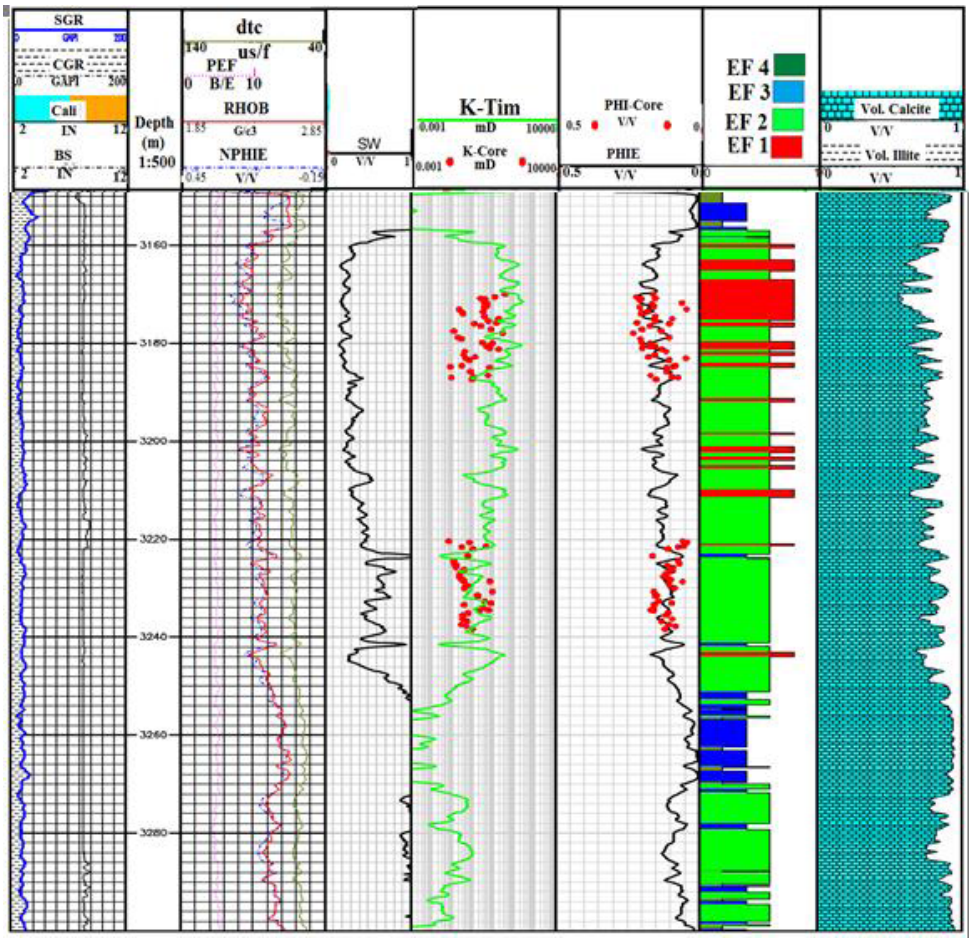

Figure 11. The comparison of K- TIM and K- core permeabilities with EFs in Well#W44.

All the studied intervals categorized in EFs-1and 2 are indicating high permeability. Therefore, any future development wells drilled in those intervals containing EFs-1 and 2 will confirm high potential and production rates. EF-3 which contains less vuggs is considered as the third order of reservoir quality after EFs-1 and 2. EF-4 should not be considered in view of permeability as having no reliable reservoir characteristics, so it will be defined as a non-reservoir zone. It can be concluded that the existence of vuggs is the main reason for increasing the permeability and the reservoir quality.

Stoneley wave logs, the Timor method and core data correlated well in all electrofacies. It can be suggested that the Stoneley results represent a good candidate for core analysis and a reasonable method to differentiate electrofacies in the reservoirs specific to those horizons/wells where the coring process is not successful.

Acknowledgments

The authors would like to acknowledge the support and advice of colleagues at National Iranian Oil Company (NIOC), Geological development section, and the Research Manager of Shahid Chamran University of Ahvaz for their encouragements. We should also express special thanks to our colleague, Dr. Mahmood Validy, assistant professor of English in the English Department at Shahid Chamran University of Ahvaz for his corrections and editing. We would also like to express frankly thanks to anonymous referees for their critical points to improve the quality of the paper.

***Nomenclature* defining symbols**

DTST = Stoneley wave slowness (μs/ft),
DTSH= Shear wave slowness (μs/ft),
DTMF= Mud filtrate slowness (μs/ft),
EF= electrofacies
FZI= Flow zone index
IMF= Flow zone index matching factor

K or KST= Permeability from stoneley method (md)
ms = millisecond
MFD= Mud filtrate density (μs/ft),
RHOB= Density of the rock (gr/cc)
φ = Effective porosity
LQC= Log quality control

References

Abbaszadeh M, Fujii H, and Fujimoto F (1996) Permeability prediction by hydraulic flow units - Theory and applications: *SPE Formation Evaluation.* 11

Al-Adani N, and Barati A (2003) New hydraulic unit permeability approach with DSL.*SPWLA 9th Formation Evaluation symposium*, Japan, September, 25-26.

Amaefule JO, Altunbay M, Tiab D, Kersey DG, and Keelan DK (1993) Enhanced reservoir description: Using core and log data to identify hydraulic (flow) units and predict permeability in uncored intervals/wells. *68th SPE Annual Technical Conference and Exhibition*, Houston, Texas. SPE26435.

Anissofira A and Latief FDE (2015) Permeability estimation of crack type and granular type of pore space in a geothermal reservoir using lattice boltzmann method and Kozeny-Carman relation, *Proceedings World Geothermal Congress 2015, Melbourne*, Australia, 19-25 April.

Anovitz LM and Cole DR (2015) Characterization and analysis of porosity and pore structures, *Reviews in Mineralogy & Geochemistry*, **80,** 61-164.

Archie, G.E. (1952) Classification of carbonate reservoir rocks and petrophysical considerations. AAPG Bulletin, 36, 2, 278-298.

Bagheri AM and Biranvand B (2006) Characterization of reservoir rock types in a heterogeneous clastic and carbonate reservoir. *JSUT***, 32, 2,** 29-38.

Batzle M and Wang Z (1992) Seismic properties of pore fluids. *Geophysics*, **57**, 11, 1396-1408.

Bordenave ML and Hegre JA (2005) The influence of tectonics on the entrapment of oil in the Dezful Embayment, Zagros fold belt, Iran, *J. Petrol. Geol.*, **28**, 4, 339 – 368.

Brown, A.A., 2015, Interpreting permeability from mercury injection capillary pressure data, *AAPG 2015 Annual Convention and Exhibition*, Denver, Colorado, May 31 – June 3, 2015.

Close D, Cho D, Horn F, and Edmundson H (2009) The Sound of Sonic: A historical perspective and introduction to acoustic logging, *CSEG Recorder*, **34**, 5, 34-43.

Collet O and Gurevich B (2013) Fluid dependence of anisotropy parameters in weakly anisotropic porous media. *Geophysics*, **78**, 5, WC137–WC145.

Eigmati MM, Zhang H, Bai B, and Flori R (2011) Submicron-pore characterization of shale gas plays. *Soc Petrol Eng SPE*-144050-MS.

Ellis DV, and Singer JM (2008) *Well logging for earth Scientist*, 2nd edn., Springer, 692P.

Gao, Z., and Hu Q (2013) Estimating permeability using median pore-throat radius obtained from mercury intrusion porosimetry, J. Geophys. Eng., 10, 1-7.

Green DP (2009) *Extracting Pore Throat size and relative permeability from MRI-based capillary pressure curves,* The International Symposium of the Society of Core Analysts held in Noordwijk, The Netherlands 27-30 September, SCA2009-46, 6P.

Gupta R, and Maloney D (2015) *Application of the intercept method to correct steady-state relative permeability for capillary end-effects,* SCA2015- 001, 12P.

Jennings, JB (1987) Capillary pressure techniques: Application to exploration and development geology. AAPG Bulletin, 71, 10, 1196-1209.

Josh M, Esteban L, Piane CD, Sarout J, Dewhurst DN, Clennell MB (2012) Laboratory characterization of shale properties*. Journal of Petroleum Science and Engineering,* **88–89,** 107–124.

Lake LW (1989) *Enhanced oil recovery,* Englewood Cliffs, N.J.: Prentice Hall, New Jersey, 550P.

Lucia JF (2007) *Carbonate reservoir characterization- An integrated approach,* Springer-Verlag, Berlin, Heidelberg, 2nd edn., 336P.

Luijendijk E and Gleeson T (2015) How well can we predict permeability in sedimentary basins? Deriving and evaluating porosity–permeability equations for noncemented sand and clay mixtures, *Geofluids,* **15**, 67-83.

Malembo CL (2015) Effective anisotropy from thinly layered reservoir versus fluid saturation, *MSc Thesis, NTNU Norwegian Uni. of Sci.Tech.,* Faculty of Eng. Sci.Tech., Dept. Petrol. Engin. Appl. Geophy., 60P.

Nelson RA (2001) *Geologic analysis of naturally fractured reservoirs,* 2nd edn, Gulf Professional Publishing, 332P.

Ortega C, Aguilera R (2014) a complete petrophysical evaluation method for tight formations from drill cuttings on in the absence of well logs. *SPE J,* Aug, 636–647.

Rabiller P (2005) *Facies prediction and data modeling for reservoir characterization,* 1st ed. Rabiller Geo-consulting.

Rebelle M, Umbhauer F and Poli E (2009) Pore to grid carbonate rock-typing, *International Petroleum Technology Conference,* Doha, Qatar.

Sadeq QM, Bhattacharya SK and Wan Yusoff WIB (2015) Permeability estimation of fractured and vuggy carbonate reservoir by permeability multiplier method in Bai Hassan oil field Northern Iraq. *Petroleum Environmental Biotechnology,* **6**, 4, 1-7.

Schlumberger (1989) *Log interpretation principles/applications,* 8th Printing Feb.

Schlumberger (1974) *Log interpretation-applications*: New York, Schlumberger Limited. 2, 116P.

Serra O (1986) *Fundamentals of well log interpretation: Volume the interpretation of logging data:* Amsterdam (Elsevier).

Serra O and Abbott HT (1982) The contribution of logging data to sedimentary sedimentology and stratigraphy. *Society of Petroleum Engineers J.*, **22,** 1, 117-131.

Serra O and Sulpice L (1975) Sedimentological analysis of shale-sand series from well logs, *Transactions of the SPWLA 16 Annual Logging Symposium PWLA.*

Tiab D and Donaldson EC (2004) Petrophysics: *Theory and practice of measuring reservoir rock and fluid transport properties,* 2nd Ed., Elsevier. Gulf Professional Publishing: 915P.

Timur A (1968) An investigation of permeability, porosity and residual water saturation relation for sandstone reservoir. *Log Analyst,* **9**, 4 p.

Uspenskaya LA, Kalmykov GA, and Belomestnykh AA (2012) Evaluation of formation permeability from borehole Stoneley wave with lithological composition, *Moscow Univ. Geol. Bull.* , **67**, 3, 202-207.

Vesanto J (1999) SOM-based visualization methods. *Intelligent data analysis,* **3**, 111-126.

Wang T, Huang Y, Chen X, and Chen X (2016) Using grain-size distribution methods for estimation of air permeability**,** *Ground Water***, 54**, 1, 131-142.

Wei DF, Liu XP, Hu XX, Xu R, and Zhu LL (2015) Estimation of Permeability from NMR logs based on formation classification method in tight gas sands, *Acta Geophysica.* **63**, 5, 1316–1338.

Winkler KW, Liu HL, and Johnson DL (1989) Permeability and borehole Stoneley waves: Comparison between experiment and theory. *Journal of Geophysics,* **54,** 66-75.

Wu X and Yin H (2010) Method for determining reservoir permeability from borehole stoneley-wave attenuation using Biot's poroelastic theory,*US patents. USPC Class: 16625002,* Patent application number: 20090145600.

Ye SJ and Rabiller PhA (2000) New tool for electrofacies analysis: multi resolution graph based clustering, *SPWLA, 41 Annual Logging Symposium*, June 4-7.

Ye SJ and Rabiller PH (2005) Automated electrofacies ordering, *Petrophysics,* **46**, 6, 409-423.

Geofísica Internacional (2018) 57-2: 121-138

Original paper

The recent instrumental seismicity of Syria and its implications

Mohamad Khir Abdul-Wahe* and Jamal Asfahani

Received: March 14, 2017; accepted: March 06 2018; published on line: April 02, 2018

Resumen

Esta contribución es un intento por ampliar el conocimiento actual sobre la reciente sismicidad instrumental que fue registrada durante el período 1995-2012 por la red sismológica nacional Siria, así como sus escenarios sismotectónicos. La reciente sismicidad instrumental ha demostrado que se han producido un pequeño número de eventos de baja magnitud. En consecuencia, en comparación con la sismicidad histórica, esto indica que la actividad está pasando por una relativa inactividad.

La correlación entre la sismicidad instrumental y las características sismotectónicas se realizó mediante el análisis de distribuciones espaciales de eventos sísmicos y mecanismos focales de algunos eventos más fuertes. Los resultados actuales permiten observar muchos tipos de actividad sísmica de la siguiente manera: tipo de enjambre, tipo de conglomerado y tipo ocasional, lo que podría mejorar la comprensión del comportamiento de las fallas sismicamente activas. Los largos períodos de retorno de grandes terremotos (M≥5) y la brevedad de la sismicidad instrumental nos impiden distinguir por completo la actividad sísmica y descubrir todas las fallas activas en el país.

Palabras clave: sismicidad instrumental, Sistema de falla del Mar Muerto, Swarm, Siria.

Abstract

This contribution is an attempt to enlarge the current knowledge about the recent instrumental seismicity, recorded during the period 1995-2012 by the Syrian national seismological network, as well as the seismotectonic settings in Syria. The recent instrumental seismicity has shown that the earthquake activity has produced a little number of low magnitude events. Consequently, it indicates that this activity is actually passing through a relative quiescence in comparison with the historical seismicity.

The correlation between the instrumental seismicity and the seismotectonic features was performed by analyzing spatial distributions of seismic events and focal mechanisms of some strongest events. The current results, allow observing many types of the seismic activity as follows: Swarm-type, Cluster-type, and Occasional-type, which could improve the understanding of the behavior of the seismically active faults. The long return periods of large earthquakes (M≥5) and the shortness of instrumental seismicity, prevent us to completely characterize the seismic activity and to discover all the active faults in the country.

Key words: Instrumental seismicity, Dead Sea Fault System, Swarm, Syria.

M. K. Abdul-Wahed*
Jamal Asfahani
Dept. of Geology the Atomic Energy Commission of Syria (AECS
P.O. Box 6091 Damascus–Syria

**Corresponding author:* cscientific@aec.org.sy

Introduction

Syria has suffered from several destructive earthquakes along the history, where the historical documents show many large earthquakes along the Dead Sea Fault System (DSFS). During the past decade, palaeoseismic investigations along the DSFS have proven successful in identifying surface ruptures associated with historical earthquakes (Gómez *et al*., 2003; Wechsler *et al*., 2014), and in documenting evidences for long-term earthquake behavior such as temporal clustering (Klinger *et al*., 2015; El-Isa *et al*., 2015). The focus in the present study corresponds to the recent instrumental seismic activity in Syria. The Syrian National Seismological Network (SNSN) has been installed in 1995 and covered the Syrian territories. Thanks to the SNSN, this work intends to be the first careful and detailed analysis of the recent instrumental seismicity of Syria, which has been recorded during the period from 1995 to 2012. The main purpose of this work is to characterize the seismicity pattern of Syria by locating earthquakes and calculating the focal mechanism of some strongest events, and then, relate the earthquake activity with the well-known tectonic structures in the region. This would improve and strengthen the knowledge of the actual seismotectonic deformations taking place now. Thereby, the instrumental seismic activity should be documented, and it is hoped to improve the seismic hazard assessment and the development of appropriate risk-mitigation strategies.

Seismotectonic setting

Syria is located on the northern part of the Arabian plate (Figure 1). It is bounded from the west by the northern section of the DSFS. Northeast of Antioch, the DSFS intersects the Eastern Anatolian Fault System (EAFS) and the Bitlis Suture zone, both of which comprise the northern border of the Arabian plate. At a gross scale, Syria can be spatially divided into four major 'tectonic zones' and intervening structural highs include the Palmyrides Fold Belt (PFB), the Abd-el-Aziz Faults, the Euphrates Fault System (EFS) and the DSFS (Figure 2). These major structural zones have accommodated most of the tectonic deformation in the country throughout the Phanerozoic, whereas the intervening stable areas remained structurally high and relatively undeformed (Barazangi *et al*., 1993; Brew *et al*., 2001). Additionally, the style of structural reactivation, in Syria, is dependent on the orientation of the aforesaid tectonic regions to the prevailing stress

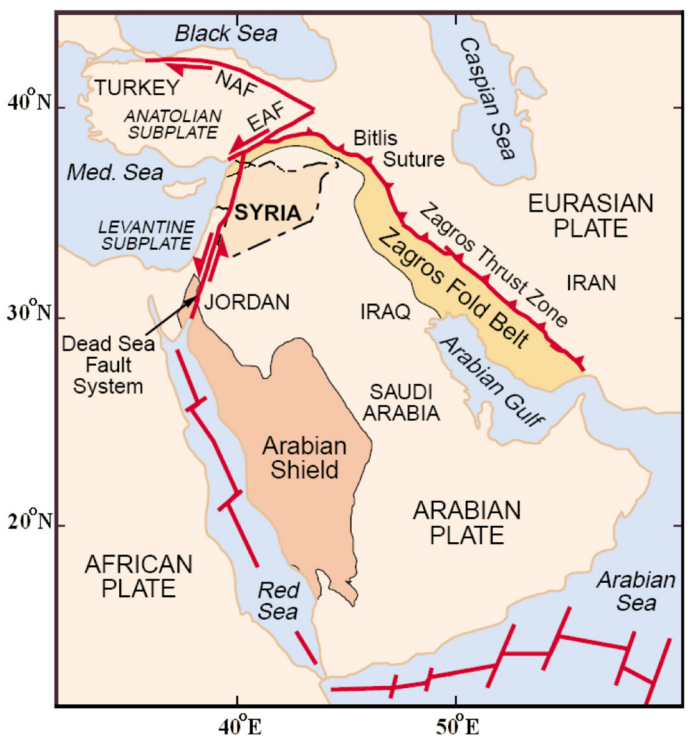

Figure 1. Map showing simplified tectonic setting of the Arabian plate and nearby tectonic features around Syria. Abbreviations: EAF: Eastern Anatolian Fault system, NAF: Northern Anatolian Fault system, Med: Mediterranean.

pattern. Furthermore, (Barazangi *et al*., 1993) inferred that the tectonism within the country is concentrated in those four major tectonic zones, which include a fold and thrust belt, a plate boundary transform fault, inverted basins and an extensive aborted rift. The DSFS is an extremely important tectonic feature, which accounts for the bulk of seismic activity in the eastern Mediterranean and accommodates the relative sinistral motion between the African and Arabian plates (Reilinger and McClusky, 2011). Recent GPS studies have characterized the first order geodetic velocity field around the DSFS (Alchalbi *et al*., 2010; Al-Tarazi *et al*., 2011; Saleh *et al*., 2012; Mahmoud *et al*., 2013; Masson *et al*., 2015). Focal mechanisms of moderate-to-large earthquakes show a sinistral motion along the DSFS (Salamon *et al*., 1996; Hofstetter *et al*., 2007). The state of stress is characterized by the coexistence of a normal faulting stress regime with the primarily strike-slip one (Palano *et al*., 2013). In a review of the slip and seismicity of the DSFS, Garfunkel (2011) concludes that the slip rate is slowing from an average rate of 6–7 mm/year over the last 5 Ma to 4–5.5 mm/year in the Pleistocene together with a slight eastward shift of the Euler pole of rotation between Sinai and Arabia. A quick review of the historical seismic activity in the eastern Mediterranean clearly demonstrates that this part of the world has been shaken since 2000 B.C. by strong earthquakes that destroyed thousands of structures, and caused severe casualties and loss of human life (Darawcheh *et al*., 2000; Khair *et al*., 2000; Guidoboni *et al*., 2004; Guidoboni & Comastri, 2005). The return periods of large earthquakes (M≥5) in Syria was estimated to be about 200-350 years (Ambraseys and Barazangi, 1989).

Data and Methods

In 1985 the General Establishment of Geology and Mineral Resources (GEGMR), responding to an initiative proposed by the Program for Assessment and Mitigation of Earthquake Risk in the Arab Region (PAMERAR), started the design and implementation phases for the construction of the SNSN. The network's design objective was to monitor all discernible earthquake activity along the DSFS and its related branches in Syria and nearby Lebanon such as Serghaya fault. The 9 seismic stations of the southern sub-network became operational in late 1994 and early 1995

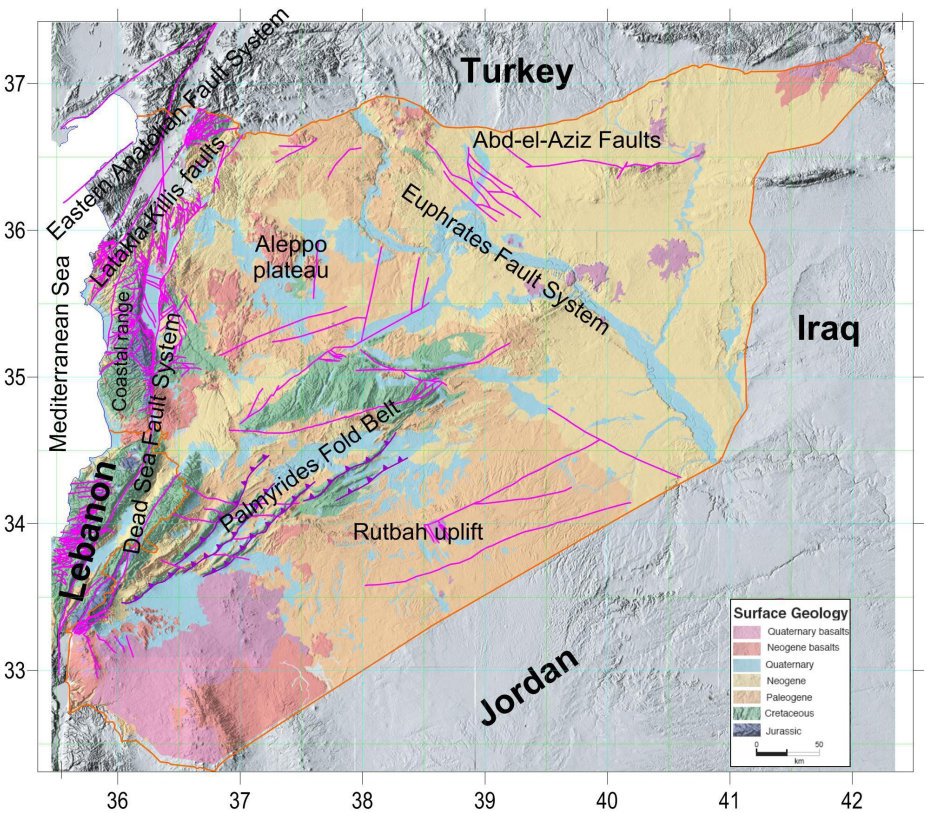

Figure 2. Tectonic zones of Syria (modified from Brew *et al*. (2001).

and allowed to record the micro-earthquake activity that occurred on November 22, 1995, along the Serghaya fault. The 11 stations of the northern sub-network followed the next year to complete the 20 stations of the western SNSN. The SNSN has been officially operated since January 14, 1995 (Dakkak *et al*., 2005). The 7 eastern stations were added in April 2002, where 2 of them were three-component seismic stations. In 2003, the SNSN consists of 27 short period (1 Hz) stations of ~50 km seismograph spacing (Figure 3). More information about the SNSN data, such as acquisition, transmitting, processing, recording, can be found in (Dakkak *et al*., 2005).

The SNSN has provided the local instrumental data for the first time in Syria. During the study period 1995-2012, the SNSN has digitally recorded about 5000 local events. Hypocentral locations for the recorded local events were determined using a program based on HYPO71 algorithm (Lee, 1990), in which, the change in the arrival time due to change in hypocentral position is linearized. This program takes the station locations, crustal seismic velocity model, and the phase information in the input file. It assumes a trial origin time and hypocentral location for the earthquake, and improve the origin time and hypocentral location by iteratively minimizing the least square error of the travel time computed from the input station, crustal seismic velocity model and phase information. Because of the linearization of the problem several iteration steps are necessary to obtain the smallest misfit of observed and predicted travel-times, which is represented by the minimum average location root mean square error (RMS).

The hypocentral coordinates and the origin time are iteratively estimated using stepwise statistical regression procedure. That is an inversion process, which need many control parameters. Some of them have been fixed as the following: minimum number of stations to attempt a solution to be 4, minimum number of phases to be 3, cut-off RMS value to be 0.99 s, maximum number of iterations to be 99.

It is very common to express the overall location quality by the RMS as a value of the error parameters. Since seismic events are located with arrival times that contain observational errors and the travel times are calculated under the wrong assumption that the exact model is known, all hypocenter determinations will have errors. The RMS of the final solution is very often used as a criterion for 'goodness of fit'. Although it can be an indication, RMS depends on the number of stations and does not in itself give any indication of errors. It is therefore not sufficient to give one number for the hypocenter error since it varies spatially in horizontal and vertical

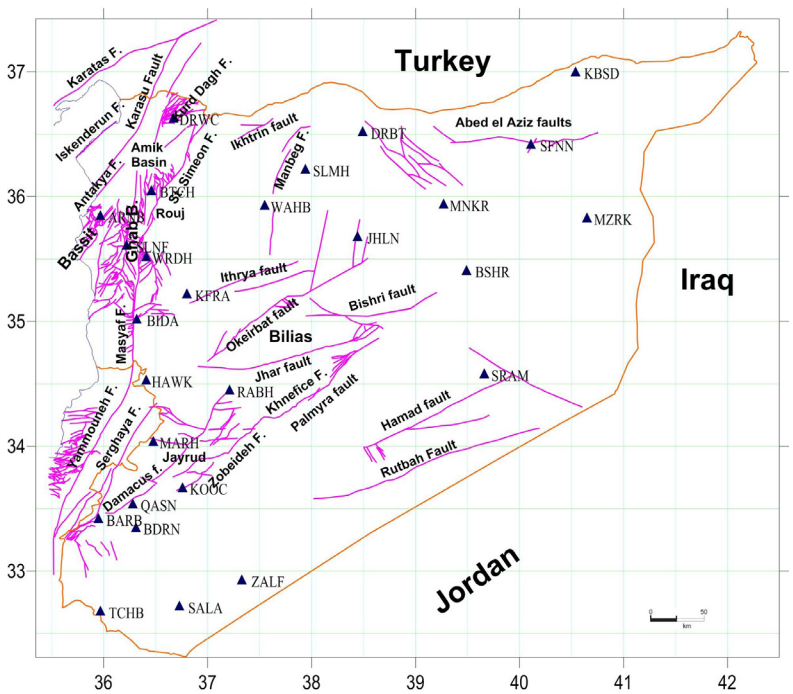

Figure 3. Map showing geographical distribution of the Syrian National Seismological Network (▲) and the principal faults. Fault geometry is summarized from Brew *et al*. (2001). Abbreviations: fault (F.), basin (B.).

directions. The accuracy of events' location is a critical factor for reliably identifying faulting parameters. To improve the accuracy of location, the records were filtered by using Butterworth order 3 filter, in order to get the best signal-noise ratio, where all P and S phases were manually picked. As a result, the number of arrival time readings was increased. Events were relocated with the new arrival times.

The magnitudes have been calculated from the coda wave duration via the formula (Bulletin of SNSN, 1995-2009):

$$M_C = -3.0 + 2.6 * \log (T) + 0.001 * D \quad (1)$$

where T is the coda duration (in sec) and D is the epicentral distance (in km).

A quantitative idea about magnitude and frequency of events could be obtained by adopting the empirical Gutenberg and Richter relation:

$$\log N = a - bM \quad (2)$$

where N is the number of earthquakes of magnitude equal or greater than M, and a and b are constants for the region, where a is a measure of the level of seismic activity and b (b-value) is the rate at which events occur within a given magnitude range. Different methodologies for assessing the b-value of the Gutenberg and Richter relation are available in literature. The least-squares method (LSM) is often used, although not formally suitable since magnitude is not error free, cumulative event counts are not independent, and the error distribution of the number of earthquake occurrences does not follow a Gaussian distribution. The maximum likelihood method (MLM) has been widely applied to assess the b-value. In this study, the Gutenberg and Richter relation is evaluated from the available recorded events by the LSM and MLM methods using the code "bvalue.exe" from the SEISAN 10.3, software (2015).

The low seismicity in Syria and the insufficient coverage of seismic stations of SNSN (Dakkak *et al*., 2005) limit the number of fault plane solutions that can be obtained from the available records. The greater the magnitude, the better the seismogram trace and the higher number of seismic stations registering the event, are allowing an improved location and a more reliable focal mechanism determination. However, small events often exhibit a large scatter due to local structure and stress perturbations and are poorly representative of the regional stress field. Therefore, a probabilistic method, proposed by Zollo & Bernard (1991), was applied to calculate the focal mechanisms of some largest events. This non–linear inversion method assumes a double-couple point-source model, a well determined earthquake location, and the model parameters to be the fault angle orientations: strike, dip and slip (or rake). The posterior probability of these parameters for the given observational data set, P-wave polarities, is computed by using Bayesian approach. The method is based on the estimation, by an exhaustive search of the posterior probability, of model parameters. The maximum likelihood solutions are only represented by its lower hemisphere projection. The available data and the reliability of the solutions are carefully examined in order to get the best results.

Detailed analysis of results

The availability of recent instrumental data, allows the knowledge about the seismotectonic of Syria to be improved. For this instance, the spatial analysis is an important key, where a spatial comparison between seismicity and mapped fault locations allows to assess the possible activity along a given fault or group of faults. The hypocentral locations for the recorded events have been determined with a location uncertainty of less than 10 km (Figure 4). Thus, the epicentral map (Figure. 5) can be considered reliable for the following interpretation of the present work. According to the epicentral map, the recent instrumental seismicity inside Syria is characterized by many clusters of weak events (M<4). Most of the recorded events are low magnitude and can be qualified as weak, where their average magnitude is approximately 2.0 (Figure 6). The focal mechanism of some strongest events (Figure 7) could be helpful to relate the earthquake activity with the well-known tectonic structures in the region. A detailed analysis on the recent instrumental seismicity, carried out in the present paper, allows observing some seismic types as follows: Swarm-type, Cluster-type, Occasional-type. This classification could help to present in detail the properties of seismic activity and its relationship with the tectonic features of some specific areas, and to focus on the most important fault zones.

1- Swarm-type seismic activity

Earthquake swarms are generally observed in volcanic regions, and defined as prolonged series of earthquakes of small to moderate magnitude without a distinct major event and strike in a relatively short period of time. The seismicity of the Jordan Dead Sea Transform

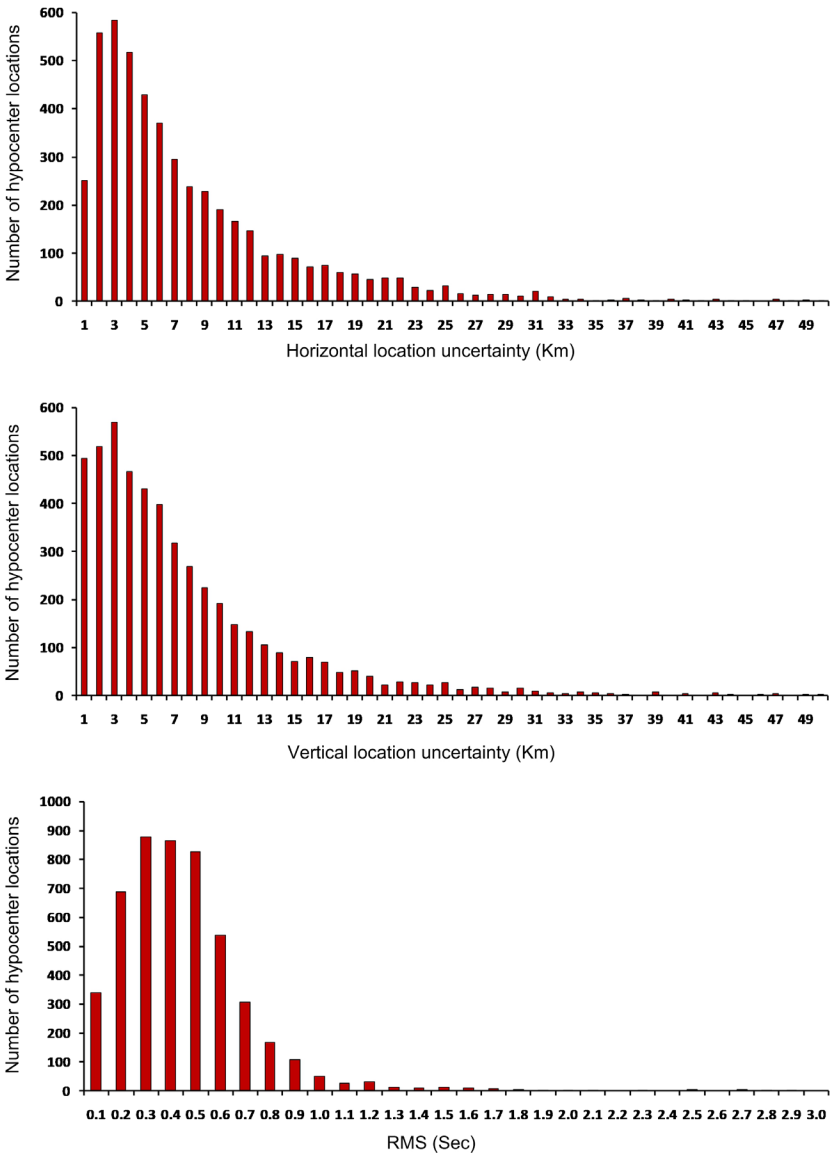

Figure 4. Histograms of location uncertainty in horizontal and vertical directions, and the RMS.

region is characterized by a relatively high proportion of seismic sequences and swarms, some of which are related to subsurface volcanic activities (El-Isa, 2012; Salamon, 2009). About 57 % of historical seismicity along the DSFS occurred in the form of sequences and swarms that lasted for variable periods of time, ranging from a few hours to a few days, weeks, months, and a few years (El-Isa *et al*., 2015). Relying on the instrumental seismicity of the Gulf of Aqaba region, El-Isa (2012) deduced that not less than 98 % of the local seismicity occurred in form of sequences and swarms. Swarms are often characterized by multiple or double earthquakes with very similar waveforms. The multiples or doublets have been interpreted as repeated slip on fault asperities or clusters of asperities. It offers the opportunity to re-examine the relationship between pre-existing fault zones and current seismicity in order to improve thereafter our understanding of the intracratonic seismicity patterns (Uski *et al*., 2006). Many swarms were observed in the recent instrumental seismicity in Syria, where the correlation between the observed swarms and the nearby faults was interpreted and analyzed through the spatial distributions of the hypocenters, as follows:

a- Serghaya fault

The NE–SW striking Serghaya fault branches out from the main transform of DSFS. It is a prominent structure located approximately along the Syrian–Lebanese border. Combined field investigations in geomorphology and paleoseismology have detected young fault scarps, mole tracks, pressure ridges and offset

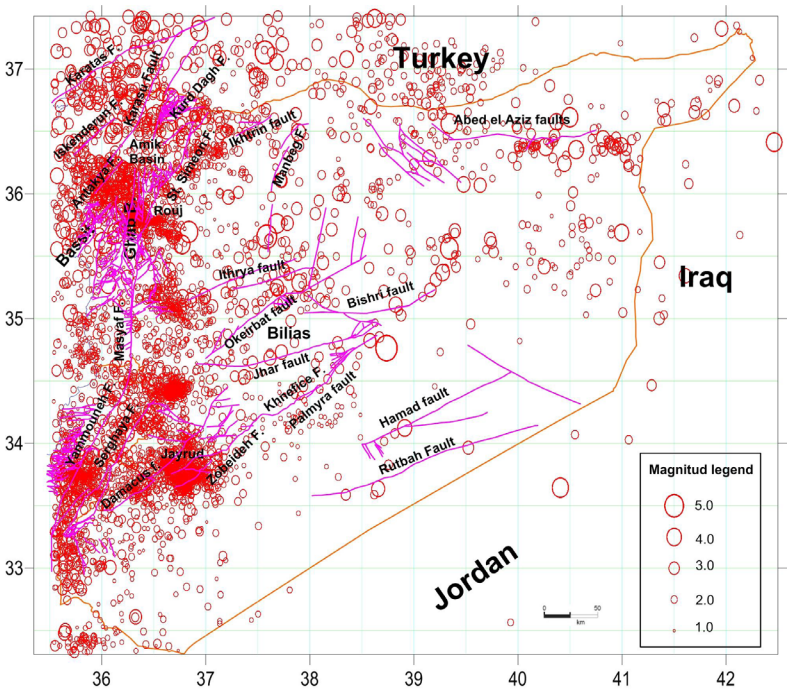

Figure 5. Earthquake activity in Syria and nearby countries recorded by Syrian National Seismological Network from 1995 to 2012.

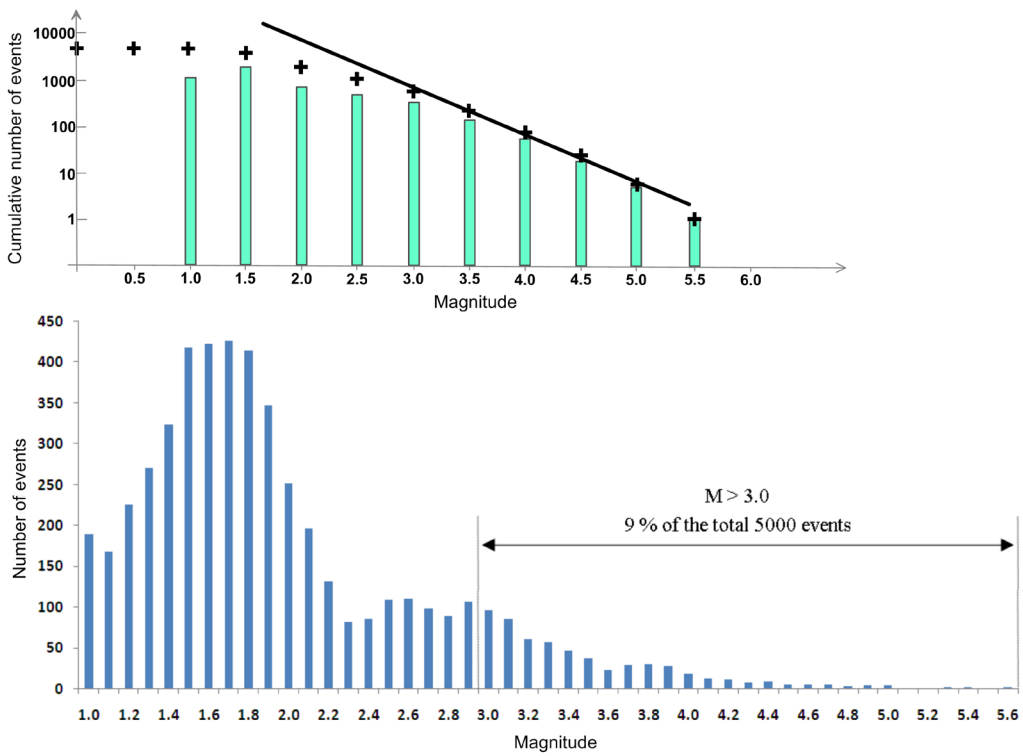

Figure 6. Frequency-magnitude distribution of the recorded events during the period of 1995-2012 in cumulative and non-cumulative plots.

streams along the fault trace, which attest to recent coseismic ruptures (Nemer *et al*., 2008). The results of trenching (Gómez *et al*., 2001; 2003) demonstrated that the Serghaya fault has important implications in terms of regional tectonics and earthquake hazard. Serghaya fault was generally regarded, until 1995, as inactive since the Pliocene (Walley, 1988; Girdler, 1990; Butler *et al*., 1997). Asfahani and Abdul-wahed (2012) established an instrumental earthquake catalogue for the Serghaya fault for the period extending from 1995 till 2009, in order to characterize and evaluate its seismic hazard and behavior. They found that the earthquake activity of this fault produces little number of low magnitude events, at least during the study period. On November 22, 1995, a swarm of events was observed along the Serghaya fault (Figure 8). Mohamad *et al*. (2000) reported that this swarm was immediately triggered following the 1995 Aqaba earthquake at a distance of about 500 km. A total of 21 events occurred as swarms during the first three and half hours following the mainshock of Aqaba, where the strongest one was of magnitude M_S=3.7. The Serghaya swarm is the first instrumentally swarm recorded by SNSN. The similarity of waveforms between the swarm events was examined, where a multiplet of 9 earthquakes and 3 of double earthquakes were found (Abdul-Wahed *et al*., 2006; Abdul-Wahed, 2007; Abdul-Wahed *et al*., 2011). The composite focal mechanism of the biggest multiplet (Fig. 7) demonstrates a good agreement between the fault plane solutions with NE Serghaya sinistral fault motion.

b- Southwest of Palmyrides fold-thrust belt

The Palmyrides fold-thrust belt, a NE-SW-trending ~400 km long and 100 km wide, is divided into southwestern and northeastern regions separated by Jhar fault (Figure 2). In the southwest of Palmyrides fold-thrust belt, 3 swarms of events were observed in 2004 in the west of Jayrud city (Figure 8). The first swarm occurred on February 8, 2004, including 6 events. The second occurred in the same site on May 16 and 17, 2004, including 22 events. In spite of the small size of the events (Mc=2.6-3.3), this swarm was widely felt at Ma'alula city and its surroundings. The third swarm of

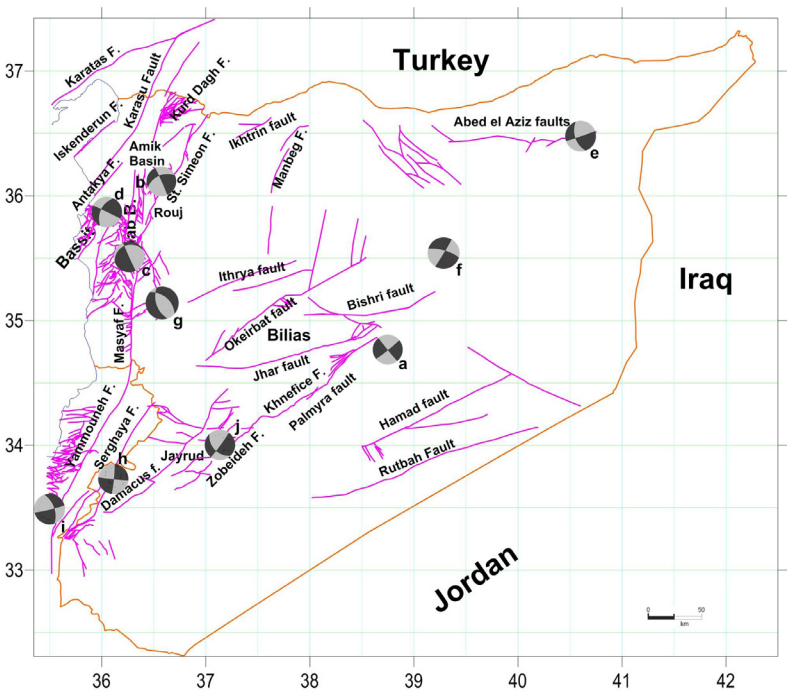

Figure 7. The focal mechanisms map of some largest events: a) an earthquake of Palmyra which happened on December 24, 1996 Mc=5.6, b) an event from the Rouj basin on May 20, 2003 Mc=4.0, c) an event from the Ghab basin on January 3, 1997, Mc=3.5, d) an event from Latakia-Killis faults system on July 19, 1996 Mc=3.9, e) an event from Abd-el-Aziz uplift faults on January 11. 1996 Mc=3.5, f) an earthquake of Bishri fault on December 18, 1994 Mc=5.0, g) the composite focal mechanism of the detected multiplet in Asharneh Plain, h) the composite focal mechanism of the biggest multiplet detected in Serghaya swarm on November 22. 1995, i) an earthquake of Roum fault on March 26, 1997, Mc=4.9, j) the composite focal mechanism of the detected doublet in Zobeideh fault. Mc: coda magnitude.

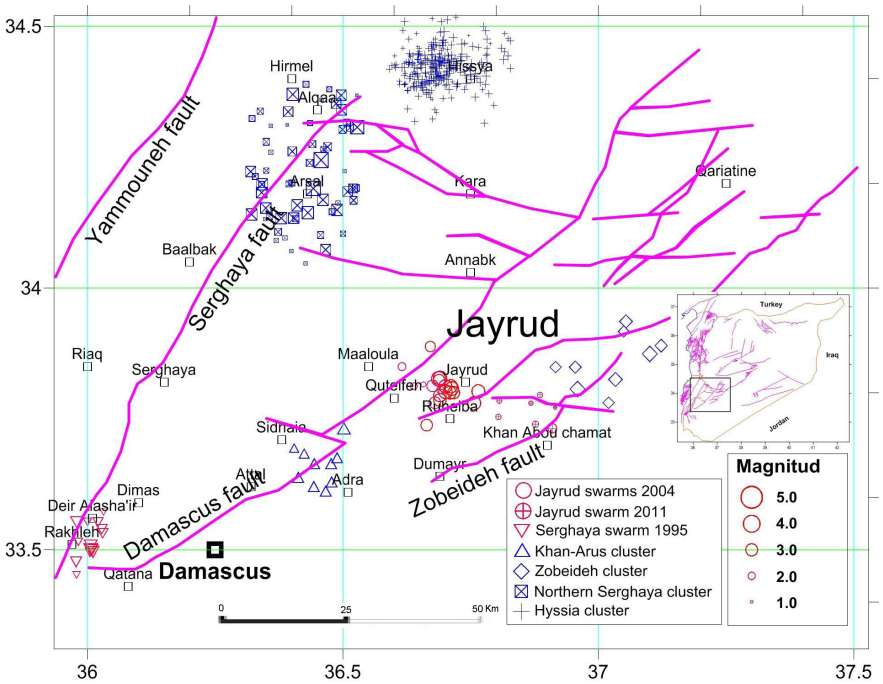

Figure 8. Detailed epicenters map of some important seismic activities observed in Damascus region.

8 events occurred on June 7, 2004, in which, an event attend the magnitude of 3.9. Another swarm of 8 events was observed on April 21, 2011, in Jayrud region. Those swarms can be related to southwest of Palmyrides faults as an extension of Damascus NE fault.

c- Baer-Bassit region faults

The Baer-Bassit region is located in a critical region near the boundary of the African and the Eurasian plates and the interaction between DSFS and EAFS. A Latakia-Killis faults system (Figure 2) was mapped as a thrust fault bordering the Baer-Bassit massif to the northeast, parallel to EAFS, where unusually steep dips were noted. This system was seen as connecting Latakia city area to the town of Killis in southern Turkey and the Kurd Dagh region, ~150 km to the northeast. The Baer-Bassit region is seismically considered as the most active in Syria (Figure 5) with high density of faults extending in the sea toward the southwest according the Cyprus arc. A swarm of 4 events started on June 3, 1996, in the sea against the Baer-Bassit region, where the biggest one has a magnitude of 4.5 and was felt in the whole costal region (Sbeinati and Darawcheh, 1997). Three swarms have been observed around Kassab city. The first of 5 events occurred on June 19, 1996. The second swarm of 6 events occurred on January 3, 2003, in which, an event had magnitude of 4.1. The third swarm of 3 events occurred on February 1, 2007. These swarms have been probably generated on Latakia-Killis faults system.

d- Kurd-Dagh region faults

The Kurd-Dagh region is located in the northwest of Aleppo plateau (Figure 2). This region is seismically active with high density of faults extending toward the northeast according to Latakia-Killis faults system. A swarm of 5 events started on March 23, 2010, in the southwest of Rajo city, and a swarm of 3 events occurred on September 21, 2011, in the south of Afrin city. Another swarm of 4 events occurred on November 20, 2011, in the south of Azaz city. Although the events of those swarms are of low magnitude, however, they indicate the activity of Kurd-Dagh region.

e- Roum fault

Fresh fault scarps and pressure ridges visible along the Roum fault trace attest to recent coseismic ruptures (Nemer and Meghraoui, 2006). On this fault, branching out from the DSFS in south Lebanon at the southern deflection point of the Yammouneh bend, a swarm of events started on March 26, 1997, by two events, with magnitudes 4.9 and 4.5, followed by 6 micro-events the next day. The first two events were felt in western Damascus (about 50 km far away), where the felt effects

were rattling of windows till some windows were broken in Serghaya (Sbeinati and Darawcheh, 1998). The composite focal mechanism of these two events (Abdul-Wahed and Al-Tahan, 2010) shows a good agreement between the fault plane solutions, and the NW Roum fault indicating a left-lateral motion on an NW striking fault (Figure 7).

2- Cluster-type seismic activity

The seismicity inside Syria (Figure 5) is characterized by many clusters of weak events (M <4) such as on southwest Aleppo plateau faults. The correlation between different seismic clusters and the seismotectonic features is analyzed through the spatial distributions of seismic events and the focal mechanisms. The cluster-type seismic activity allows to distinguish between the next faults:

a- Latakia-Killis faults system

Many clusters of events can be associated to this faults system and some of them extend in the sea toward the southwest according to the Cyprus arc. The focal mechanisms of many events demonstrate a sinistral strike slip common mechanism trending NE in agreement with the known fault system (Figure 7).

b- Northern segments of DSFS

The epicentral map (Figures 5 and 9) has shown that the instrumental seismicity is very low along the northern segments of DSFS: Masyaf, Apamea and Ghab. A cluster of 4 events was located in the middle of the Ghab basin. One event of the cluster had a normal mechanism (Abdul-Wahed, 2012) in agreement with the NW normal fault associated with the local trans-tensional features observed by Brew *et al*. *(*2001b). The Rouj basin, ~24-km-long and up to ~5-km-wide, is bounded by left-lateral faults (Fig. 3). A cluster of 42 events was observed in this basin (Figure 9). The focal mechanism, calculated for the biggest events, has shown a sinistral mechanism trending NE in agreement with the main existent faults (Figure 7). A cluster of 17 events was observed at the northeast extension of St. Simeon fault around Shran city. At the northern end of the Ghab Basin, the El-Wastani mountain is bounded by Armanaz fault and Salqin fault in the east and west respectively. A cluster of 41 events was observed at the El-Wastani mountain This cluster could be related to Salqin-Armanaz faults. Asharneh plain is located in the east of the south part of the Ghab basin (25 Km northwest of Hama city) (Figure 9). A cluster of about 20 events was located in the Asharneh plain. Three of them were aligned in the NW direction and form a multiplet. The composite focal mechanism of these 3 events shows a normal fault mechanism (Figure 7) which could also be associated with local trans-tensional features. A cluster of 142 events was located between Hama and Rastan cities and aligned in the NW direction. It could be related to unmapped Hama fault.

c- Abd-el-Aziz uplift faults

The Abd-el-Aziz uplift faults, in the northeast of Syria, were roughly east-west striking and were active almost exclusively in the latest Cretaceous. These faults extend from the west

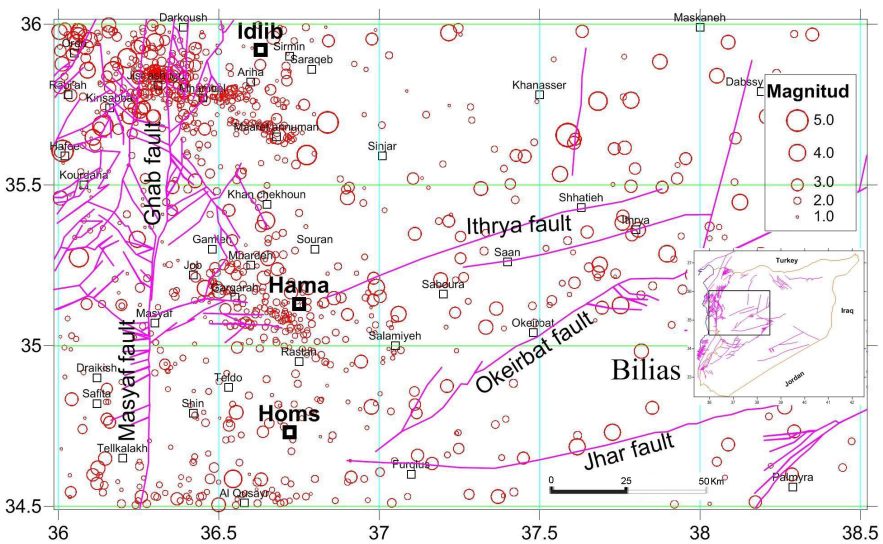

Figure 9. Detailed epicenters map of the seismic activity recorded in central part of Syria.

through Abd-el-Aziz mountain (~100 km length, max. elevation 920 m) and eastwards well into Iraq (Figure 2). The most recognized earthquake along the Abd-el-Aziz uplift faults occurred in 1975 with magnitude of M≈5.2 (Ahmad, 2013). A cluster of 43 events was observed in the middle part of the Abd-el-Aziz uplift faults (Figure 5), where an event reached magnitude 4.7. Another cluster of 31 events was observed in the eastern part. Four events, aligned in the EW direction along the Abd-el-Aziz uplift, show nearly identical source mechanism solutions and have a sinistral mechanism trending EW (Figure 7). They might indicate shearing process in this direction.

d- Palmyrides Faults

The Palmyrides fold-thrust belt separates the Rutbah uplift to the south from the Aleppo plateau to the north (Figure 2). Many sets of weak events were located in the northern region of Palmyrides. They could be related to the faults: Ithrya, Okeirbat, Bishri, Jhar, Khnefice, Palmyra and others. The scattered seismicity, observed in the current study (Figure 5) and the previous ones (Brew *et al*., 2001) suggests that the Palmyrides region is still tectonically active. The Bishri fault system is probably a dextral strike-slip fault similar to the Jhar Fault. A magnitude Ms=4.9 earthquake, occurred on November, 20, 1994, was located near this fault, at a depth of 15 km, northeast of the mapped extent of the fault (Litak *et al*., 1997). The focal mechanism for a 1970 earthquake (Mb=4.8) was determined to be dextral but the initial solution for the 1994 event suggests sinistral motion (Dziewonski *et al*., 1995). Moreover, field evidence and kinematic models (Chaimov *et al*., 1993) are consistent with dextral motion along the Bishri fault. The strongest event that occurred on December 18, 1994 (Mc=5.0), was located at the northeast of Bishri mountain. It shows dextral motion on the NE striking nodal plane (Figure 7). It could be related to the Bishri fault. A cluster of 20 events was observed during the study period in the northeast of the mapped extent of the fault (Figure 5). In the southwestern regions of Palmyrides, a cluster of 10 events is located at the northeast extension of Damascus fault near Khan-Arus site (Figure 8), where this fault interacts with a secondary north-west fault. This cluster might indicate the activity of the secondary fault rather than Damascus fault. Another cluster of 7 events are aligned in the NE direction and located along the Zobeideh fault (Figure 7), where a doublet has been detected. This doublet has a sinistral mechanism trending NE, in agreement with the Zobeideh fault (Abdul-Wahed *et al*., 2011).

A cluster of 773 micro-events has been observed in Jayrud region. In this cluster, 660 micro-events have a magnitude of less than 2.0, they could be therefore induced by quarrying exploitation. The early works in Jayrud's quarries started in 2001 (Al-Tahan, 2014) but the induced seismicity didn't appear until 2003 (Figure 10), where the exploitation has been extended to many quarries. Similarly, a cluster of 304 micro-events has been observed around Hyssia city and could be induced by quarry exploitations.

e- Northern extension of Serghaya fault

Serghaya fault can be traced approximately 125 km through the Anti-Lebanon mountains to the eastern edge of the Bekaa valley (Figures 8 and 10). Field evidence for Quaternary strike-slip faulting along the Serghaya fault is observed as far north as the village of Arsal, near the edge of the Bekaa valley (Gómez *et al*., 2003). The trace of the Serghaya fault is obscure towards to the north of this point. Its northern termination suggests a possible linkage with the Jhar fault as an oblique ramp or tear fault that bounds the Palmyrides fold belt (Gómez *et al*., 2006). Walley (1998) suggested that the Serghaya fault continues also in NNE into Syria, past Al Qusayr and SE of Homs, before splaying into the Jhar and Bishri faults within the Palmyrides fold belt. However, geological mapping in the vicinity of Al Qusayr has revealed no evidence of any such fault, and none has been noted during recent fieldwork in this area (Bridgland *et al*., 2003). In this study, a cluster of 60 events, aligned to the NE until the village of Alqaa near the Syrian-Lebanese border, was observed around the village of Arsal (Figure 8). This cluster could be associated to the northern part of Serghaya fault. The seismic activity in northern Lebanon, shown on the epicenters map, is concentrated on the northern part of Serghaya fault, which supports the finding of Walley (1998). Other cluster of 5 events was observed around Al Qusayr and makes probable the suggestion of linkage of the Serghaya fault with the Jhar and Bishri faults.

f- Aleppo plateau

The Aleppo plateau forms a central more stable region of low relief (Figure 2). The eastern and western margins of the plateau are poorly defined, especially near the DSFS, where several N–S to NE–SW strike-slip and normal faults splay out from the master fault. The Aleppo plateau is regarded as a platform with minor amounts of deformation compared to the Palmyrides (Zanchi *et al*., 2002). It is cut by some NE–SW faults which are probable zones

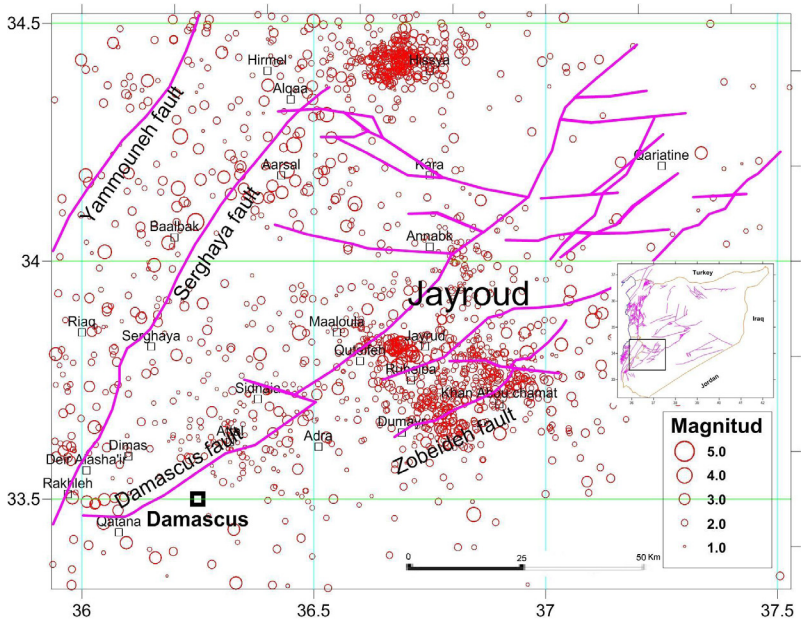

Figure 10. Detailed epicenters map of the seismic activity observed in Damascus region during the period 1995-2012.

of strike-slip (Al-Saad *et al*., 1992). The recently known earthquake in this plateau occurred in 1987 with magnitude of 4.8 (Ahmad, 2013). The seismic activity in the western margin along the DSFS, discussed above, could be considered as relatively high (Figure 11). However, it is very low in the eastern margin. In northern Aleppo, a cluster of 102 events is aligned in the NE direction and could be associated with NE Ikhtrin fault; another cluster of 26 events could be related to Manbeg fault. In the west of Aleppo plateau, Az-zawiyeh mountain overlooks the Ghab basin. It is bounded by NE-striking sinistral strike-slip fault. In this mountain, a cluster of 100 events was located.

g- Golan plateau faults

The Golan, situated at the SW of Syria, is an elevated basalt-covered plateau. To the north, it is bounded by the Hermon mountain anticline. About 180 events are located in Golan plateau and could be associated to DSFS. Some of them formed multiplets with events aligned in

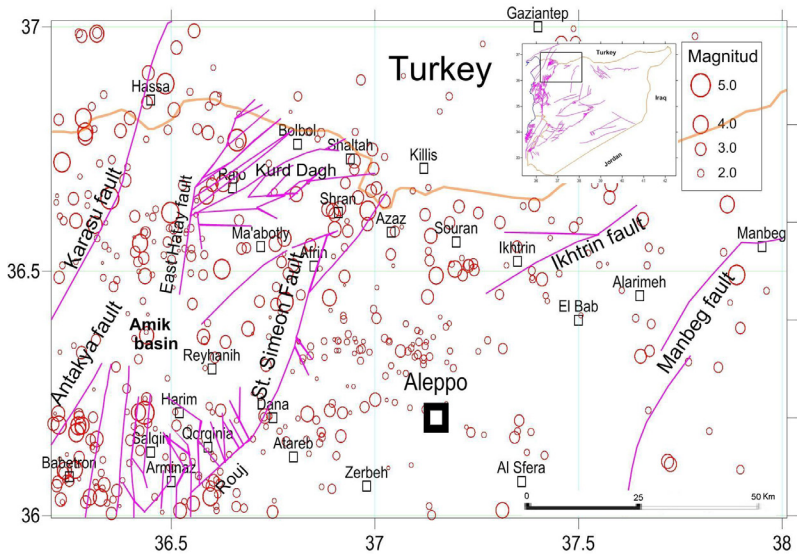

Figure 11. Detailed epicenters map of northern Aleppo.

NS direction. Two multiplets have a sinistral mechanism trending NS in agreement with DSFS (Abdul-Wahed *et al*., 2011). Another multiplet has a normal mechanism trending NE and could be related to local trans-tensional faults that extend along the margins of DSFS.

h- Coastal range

The Syrian coastal range, occupies most of the Syrian onshore area at the west of the DSFS and Ghab basin. The stratigraphic relationships indicate that the uplift of the coastal range is a part of the extensive Syrian arc deformation (compressional folding along the eastern Mediterranean coast), documented in the Levant (Walley, 2001; Salamon *et al*., 2003, 2007; Yolsal *et al*., 2007; Carton *et al*. 2009; Eyal, 2011). The coastal range has clearly been affected by the propagation of the DSFS and the formation of the Ghab basin, resulting in the steep eastern limb (Brew *et al*., 2001), that created the extremely steep scarp on the eastern face of the coastal range alongside the Ghab basin. A cluster of about 46 events is located in northern of Tartous city. Another cluster of 81 events is located in south and south east of this city.

3- Occasional-type seismic activity

Some significant events can be classified as individual such as the earthquake of Palmyra 1996 and the events of Rutbah uplift. Those events seem to be apparently scattered during the study period, but they might be in reality linked with other events that occurred before or after this period. The study period of about 17 years, from 1995 to 2012, is very short in comparison with the estimated long return period for whole Syria of 200-350 years (Ambraseys and Barazangi, 1989). It is therefore not possible to conclude that some faults, such as the northern segments of DSFS, are inactive, depending on the recent instrumental seismicity qualified as short term observations. The high magnitude of some events of occasional-type, such as the earthquake of Palmyra, 1996, could be interpreted by accumulation the seismic energy during a long period of quiescence. One can conclude that the long period of quiescence along the northern segments of DSFS might accumulate the seismic energy and could at any time produce a big earthquake especially for the reasons mentioned above (geomorphic evidence for Pliocene, recent tectonic activity on the fault together with historical seismicity and GPS measurements). The scattered seismicity in the Palmyrides fold belt suggests that this region is still tectonically active.

Discussion

During the period of studyd 1995-2012, about 5000 local events have been recorded by the SNSN (Bulletins of SNSN, 1995-2012 2009 on the reference list!!!!). In total, nearly 3800 earthquakes were located with a location uncertainty of less than 10 km. Figure 4 shows that about 50% of the entire events are reliable locations with an average location uncertainty less than 5 km in horizontal and vertical directions. The average RMS for the whole dataset is about 0.5 sec. Most of the recorded events are located within the network and have relative small location uncertainty values. Therefore, locations of these events can be considered reliable for the following interpretation of the present work. The epicentral map (Figure 5) presents the geographical distribution of the seismic activity. The study of this local instrumental data has illuminated the general appearance of the recent seismicity in Syria and spotlighted some important observations:

- The little amount of events, where the annual average of recorded events is about 292, which could be considered very low as compared with other parts of DSFS, such as Yammounah or Aqaba Gulf, indicates that Syria is actually passing through a relative quiescence period. For example, 2414 events were recorded in Aqaba Gulf in 1995 (Jordan Seismological Observatory, 1995) and 948 events in 1997 (Jordan Seismological Observatory, 1997). Furthermore, the instrumental seismicity of the eastern Mediterranean region shows that the southern part of DSFS is seismically the most active (Hofstetter *et al*., 2007; Imprescia, 2010; Imprescia *et al*., 2012). The most active area since the early 1980s was the Gulf of Aqaba, where thousands of small cluster earthquakes occurred in different regions of the Gulf of Aqaba during several months to few years (Baer *et al*., 1999; Klinger *et al*., 1999).

- The epicentral map has shown that the main instrumental seismicity with many moderate earthquakes (Mc>4) is apparently concentrated on the Syrian borders: along the EAFS extending on the northwest borders and along the central segments of DSFS in Lebanon such as Yammouneh and Roum. The EAFS, including Latakia-Killis faults system, could be characterized by the highest instrumental seismicity in Syria.

- The seismic activity inside Syria has produced events of low magnitude (Fig.

6), which consequently indicates that it is actually passing within a relative quiescence period as compared with other parts of DSFS (Meghraoui *et al*., 2003). Most of the recorded events are qualified as weak, where their average magnitude is approximately 2.0. Fig. 6 shows the frequency of the recorded events according to their magnitude, which varies between 1.0 and 5.6. Only 49 events have exceeded the magnitude of 3.0 during the period 1995-2003 (Abdul-Wahed and Al-Tahan, 2010). In the present study, only 470 events, which make 9% of the total 5000 events, have exceeded the magnitude of 3.0 during the period 1995-2012. The fitting Gutenberg and Richter relation to the observed frequency-magnitude distribution has shown a magnitude completness down to $M_{completness}$ =2.5 (Figure 6). This indicates that not all micro-earthquakes (Mc<2.5) have been detected by the SNSN. Some events could be too small to be recorded on a sufficiently large number of stations to trigger the recording system in the SNSN, to initiate the location procedure, and thus the report of the event. The network operators decided that some micro-earthquakes below a certain threshold (Mc<2.5) are not of interest. The constants of the empirical Gutenberg and Richter relationship, a- and b- values, were evaluated using the LSM method (log N= 5.43-0.91M) and MLM method (log N= 5.2-0.73M).

- According to the epicentral map, the recent instrumental seismicity inside Syria is characterized by many clusters of weak events (M<4) such as in southwest of Aleppo plateau. Some clusters were observed as swarm indicating the behavior of some faulting zones such as Serghaya fault, southwest Palmyrides faults and Bassit region faults (Figure 2).

- The most important event was the earthquake of Palmyra which happened on December 24, 1996, with a magnitude of about 5.6 (Tan and Taymaz, 2003; Alchalbi, 2004). This event is located in Palmyrides fold belt that separates two relatively stable zones, Rutbah uplift, in the southeastern of Syria from Aleppo plateau in the northwestern of Syria. The earthquake of Palmyra has a sinistral mechanism trending NE (Figure 7), and can be related to Palmyra fault (Abdul-Wahed, 2012).

Conclusion

The instrumental seismicity of Syria during the period 1995-2012, has been characterized and documented in the present paper. In total, nearly 3800 micro-earthquakes were located with a location uncertainty of less than 10 km. Therefore, locations of these events can be considered reliable for the following interpretation. The correlation between the instrumental seismicity and the seismotectonic features was performed through the analysis of spatial distributions of seismic events and some focal mechanisms, where most epicenters appear to correlate with the regional strike-slip faults. The epicentral map has shown that the main instrumental seismicity with many moderate earthquakes (M>4) is apparently concentrated on the Syrian northwest borders along the EAFS, including Latakia-Killis faults system, where the highest instrumental seismicity in Syria has been observed.

This research allowed observing many types of seismic activity as follows: Swarm-type, Cluster-type, and Occasional-type. Many observed swarms have been correlated through the spatial distributions of the hypocenters with some active faults, such as Serghaya fault and the southwest of Palmyrides. The seismicity inside Syria was characterized by many clusters of weak events (M<4) such as the clusters on Latakia-Killis faults, Rouj basin faults, and northern Aleppo plateau faults. However, some significant events could be classified as individual, such as the earthquake of Palmyra, 1996, regarding the shortness of the study period. The geographical distribution of epicenters of a cluster could be related to an active fault. This correlation could be confirmed by the focal mechanism of some strongest events. As a consequence, many faults can be considered active in Syria. The observed swarms could give an insight on the seismic behavior of some active faults such as Serghaya fault, where many events striking in a relatively short period of time are followed by a long period of quiescence. The occasional-type of seismic activity could be interpreted as a very long behavior of some active faults.

The instrumental seismicity of Syria could be classified in general as low magnitude events. Most of the recorded events are qualified as weak, where their average magnitude is approximately 2.0. In the present study, only 470 events, which make 9% of the total 5000 events, have exceeded their magnitude of 3.0 during the period 1995-2012. The fitting Gutenberg and Richter relation to the observed frequency-magnitude distribution has shown a magnitude completness down to 2.5. This indicates that not all micro-earthquakes (Mc<2.5) have been detected by the SNSN. Regarding the low magnitude level of the recorded events, we can deduce that the seismic activity in Syria is

actually passing by a relative quiescence. Such result may therefore be taken to support the finding of previous studies indicating that the seismicity in Syria tends to fade out with time, in line with the decrease of major seismic intensity which has occurred during the last millennium. This view, however, is inconsistent with both the historical records of large, devastating earthquakes, and the field observations that attest to the seismic activity and seismogenic potential of the DSFS. The discrepancy between measured rate of small-magnitude earthquakes (M <4) from instrumental records and large earthquake rates from paleoseismic records, as also observed on other faults, makes the fault's behavior unpredictable. This discrepancy can be explained if we consider that the instrumental record lacks both moderate-to-large events and their aftershocks. Since the beginning of instrumental seismicity, the DSFS experienced only one large earthquake (M=7.2) that occurred in the Gulf of Aqaba on November 22, 1995.
The characterization of the recent seismic activity in Syria is not an easy task, due to the long return periods of large earthquakes, estimated in previous studies to be about 200-350 years, and to the shortness of instrumental seismicity, about 17 years. It is therefore difficult to discover all the active faults in the country. The long period of quiescence along some faults, such as the Ghab fault, accumulates probably the seismic energy and could produce a big earthquake at any time. The nonperiodic behavior of the DSFS over the millennial timescale makes it more difficult to meaningfully predict the probability for a large earthquake soon. Therefore, it is imperative to prepare for a large earthquake on the DSFS, which will occur sooner or later. The actual results, documented in this research, highlight the need and necessity of more detailed researches for a longest possible period of time.

Acknowledgements

The authors wish to express their thanks to Prof. Ibrahim Othman Director General of the Atomic Energy Commission of Syria for his constant support. They also wish to thank the General Establishment of Geology and Mineral Resources for providing some important information and data. The anonymous reviewers are cordially thanked for their constructive remarks and suggestions that considerably improve the quality of this paper.

References

Abdul-Wahed M. K., 2012, The focal mechanism of recent largest seismic events in Syria. The 7th Gulf Seismic forum, Saudi Geological Survey; 22-25 January 2012, Jeddah, Saudi Arabia.

Abdul-Wahed M. K., Asfahani J., Al-Tahan I., 2011, A combined methodology of multiplet and composite focal mechanism techniques for the identification of the seismological active zones in Syria. *Acta Geophysica*, 59, 967-992, DOI:10.2478/s11600-011-0024-2.

Abdul-Wahed M. K. & Al-Tahan I., 2010, Preliminary outlining of the seismological active zones in Syria. *Annals of geophysics*, 53, 1-9.

Abdul-Wahed M. K., 2007, The multiplet analysis and some of its applications. The 4th Gulf Seismic forum, Kuwait Institute for Scientific Research; Kuwait, 24-27 March, 2007.

Abdul-Wahed M. K., Al Heib M., Senfaute G., 2006, Mining-induced seismicity: Seismic measurement using multiplet approach and numerical modeling. *International Journal of Coal Geology*, 66, 137-147.

Ahmad R. A., 2013, Seismic Hazard Assessment of Syria. *Journal of Seismology and Earthquake Engineering*, 15, No. 1.

Alchalbi A., 2004, Workshop on "Earthquake Hazard Assessment in Syria and Lebanon", September 7-9 , 2004, Damascus – Syria.

Alchalbi A., Daoud M., Gómez F., McClusky S., Reilinger R., Romeyeh M. A., Alsouod A., Yassminh R., Ballani B., Darawcheh R., 2010, Crustal deformation in northwestern Arabia from GPS measurements in Syria: slow slip rate along the northern Dead Sea Fault. *Geophys. J. Int.*, 180, 125–135.

Al-saad D., Sawaf T., Gebran A., Barazangi M., Best J. & Chaimov T., 1992, Crustal structure of central Syria: The intracontinental Palmyride mountain belt. *Tectonophysics*, 207, 345–358.

Al-Tahan I., 2014, Personal communication. General Establishment of Geology and Mineral Resources.

Al-Tarazi E., Abu-Rajab J., Gómez F., Cochran W., Jaafar R., Ferry M., 2011, GPS measurements of near-field deformation along the southern Dead Sea Fault System. *Geochem. Geophys. Geosyst*. 12, Q12021, http://dx.doi.org/10.1029/2011GC003736.

Ambraseys N. N. & Barazangi M., 1989, The 1759 Earthquake in the Bekaa Valley: implications for earthquake hazard assessment in the

Eastern Mediterranean region. *J. geophys. Res.*, 94, 4007–4013.

Ambraseys N. N. and C. P. Melville, 1995, Historical evidence of faulting in Eastern Anatolia and Northern Syria. *Annali Di Geofisica*, 38, 337.

Asfahani J. and Abdul-wahed M. K., 2013, Evaluation of Earthquake Activity Along the Serghaya Fault, Syria, from Instrumental Seismic Data, *Acta Geophysica*, 61, 37-59, DOI: 10.2478/s11600-012-0059-z.

Baer G., Sandwell D., Williams S., Bock Y., Shamir G., 1999, Coseismic deformation associated with the November 1995, Mw=7.1 Nuweiba earthquake, Gulf of Elat (Aqaba), detected by synthetic aperture radar interferometry. *J. Geophys. Res.*, 104, 25221– 25232.

Barazangi M., Seber, D., Chaimov, T., Best, J. and Sawaf, T., 1993, Tectonic evolution of the northern Arabian plate in western Syria. In, E. Boschi, E. Mantovani and A. Morelli (Eds.), Recent Evolution and Seismicity of the Mediterranean Region. Kluwer Academic Publishers, p.117–140.

Brew G., Barazangi M., Al-Maleh A. K., Sawaf T., 2001, Tectonic and geologic evolution of Syria, *GeoArabia*, 6, 573-616.

Brew G., J. Lupa, M. Barazangi, T. Sawaf, A. Al-Imam and T. Zaza, 2001b, Structure and tectonic development of the Ghab Basin and in Dead Sea Fault System Syria. *Journal of the Geological Society London*, 158, 665-674.

Bridgland D. R., Philip G., Westaway R., White M., 2003, A long Quaternary terrace sequence in the valley of the River Orontes, near Homs, Syria. *Current Science*, 84, 1080–1089.

Bulletin of the Syrian National Seismological Network (SNSN), 1995-2009, National Earthquake Center, Ministry of Petroleum and mineral resources, Syrian Arab Republic.

Butler R. W. H., Spencer S. & Griffiths H. M., 1997, Trans current fault activity on the Dead Sea Transform in Lebanon and its implications for plate tectonics and seismic hazard. *J. geol. Soc. Lond.*, 154, 757–760.

Carton H., S. C. Singh, P. Tapponnier, A. Elias, A. Briais, A. Sursock, R. Jomaa, G. C. P. King, M. Dae¨ron, E. Jacques, and L. Barrier, 2009, Seismic evidence for Neogene and active shortening offshore of Lebanon (Shalimar cruise). *J. Geophys. Res.*, 114, B07407, doi:10.1029/2007JB005391.

Chaimov T.A., M. Barazangi, D. Al-saad, T. Sawaf and M. Khaddour, 1993, Seismic fabric and 3-D structure of the southwestern intracontinental Pa1myride fold belt, Syria. *Am. Assoc. Petro Geol. Bull.*, 77, 2032-2047.

Dakkak R., Daoud M., Mreish M., Hade G., 2005, The Syrian National Seismological Network (SNSN): Monitoring a major continental transform fault. *Seismological Research Letters*, 76, 437-445.

Darawcheh R., Sbeinati M. R., Margottini C. & Paolini S., 2000, The 9 July 551 AD Beirut earthquake, eastern Mediterranean region. *J. Earthquake Eng*., 4, 403–414.

Dziewonski A. M. , G. Ekström, M. P. Salganik, 1995, Centroid-moment tensor solutions for October-December 1994. *Physics of the Earth and Planetary Interiors*, 91, 187-201.

El-Isa Z. H., 2012, Seismicity and seismotectonics of the Gulf of Aqaba region. *Arab J Geosci.*, doi:10.1007/s 12517-012-0604-8.

El-Isa Z. H., S. McKnight & D. Eaton, 2015, Historical seismicity of the Jordan Dead Sea Transform region and seismotectonic implications. *Arab J Geosci.*, DOI 10.1007/s12517-014-1483-y.

Eyal Y., 2011, The Syrian Arc Fold system: Age and rate of folding. *Geophysical Research*, 13, EGU2011-7401, 2011, EGU General Assembly 2011.

Garfunkel Z., 2011, The long- and short-term lateral slip and seismicity along the Dead Sea Transform: an interim evaluation. *Isr J Earth Sci*, 58, 217–235.

Girdler R.W., 1990, The Dead Sea transform fault system. *Tectonophysics*, 180, 1–13.

Gómez F., Meghraoui M., Darkal A. N., Sbeinati R., Darawcheh R., Tabet C., Khawlie M., Charabe M., Khair K. & Barazangi M., 2001, Coseismic displacements along the Serghaya fault : an active branch of the Dead Sea Fault System in Syria and Lebanon. *J. Geol. Soc. Lond.*, 158, 405-408.

Gómez F., Meghraoui M., Darkal A.N., Hijazi F., Mouty M., Suleiman Y., Sbeinati R., Darawcheh R., Al-ghazzi R., Barazangi M., 2003, Holocene faulting and earthquake

recurrence along the Serghaya branch of the Dead Sea fault system in Syria and Lebanon. *Geophys. J. Int.,* 153, 658–674.

Gómez F., Khawlie M., Tabet C., Darkal A. N., Khair K., Baranzangi M., 2006, Late Cenozoic uplift along the northern Dead Sea transform in Lebanon and Syria. *Earth Planet. Sci. Lett.*, 241, 913–931.

Guidoboni E., Bernardini F., Comastri A., 2004, The 1138-1139 and 1156-1159 destructive seismic crises in Syria, south-eastern Turkey and northern Lebanon. *Journal of Seismology*, 8, 105–127.

Guidoboni E. & Comastri A., 2005, Catalogue of earthquakes and tsunamis in the Mediterranean area from the 11th to the 15th century. *Instituto Nazionale di Geofisica e Vulcanologia*, 1037 pp.

Hofstetter R., Klinger Y., Amrat A. Q., Rivera L. and Dorbath L., 2007, Stress tensor and focal mechanisms along the Dead Sea fault and related structural elements based on seismological data. *Tectonophysics*, 429, 165-181, doi:10.1016/j.tecto.2006.03.010.

Imprescia P., 2010, Meccanismi focali di terremoti come strumento per la definizione della sismotettonica dell'area mediterranea. *Ph.D. thesis*, University of Catania.

Imprescia P., Palano Mimmo, Gresta Stefano, 2012, Mapping crustal strain and stress fields across the Dead Sea Fault System by GPS observations and focal plane solutions. Conference paper: GNGTS November 2012, Volume: Extended Abstract.

Jordan Seismological Observatory, 1995, Earthquakes in Jordan and adjacent areas, Nat. Res. Auth., *Jordan Seis. Obs., Bul.*, No. 27.

Jordan Seismological Observatory, 1997, Earthquakes in Jordan and adjacent areas, Nat. Res. Auth., *Jordan Seis. Obs., Bul.*, No. 29.

Khair K., Karakaisis G. F. and Papadimitriou E. E., 2000, Seismic zonation of the Dead Sea Transform Fault area. *Annali di Geofisica*, 43, 61–79.

Klinger Y., Rivera L., Haessler H., Maurin J.C., 1999, Active faulting in the Gulf of Aqaba: new knowledge from the Mw7.3 earthquake of 22 November 1995. *Bull. Seismol. Soc. Am.*, 89, 1025– 1036.

Klinger Y., M. Le Beon and M. Al-Qaryouti, 2015, 5000 yr of paleoseismicity along the southern Dead Sea fault. *Geophys. J. Int.*, 202, 313–327, doi: 10.1093/gji/ggv134.

Lee W. H. K., 1990, Hypo71 Program. vol. 1. IASPI Software Library.

Litak R. K., M. Barazangi, W. Beauchamp, D. Seber, G. Brew, T. Sawaf and W. Al-Youssef, 1997, Mesozoic-Cenozoic Evolution of the Intraplate Euphrates Fault System, Syria: Implications for Regional Tectonics. *Journal of the Geological Society*, 154, 653-666.

Mahmoud Y., F. Masson, M. Meghraoui, Z. Cakir, A. Alchalbi, H. Yavasoglu, O. Yönlü, M. Daoud, S. Ergintav, S. Inan, 2013, Kinematic study at the junction of the East Anatolian fault and the Dead Sea fault from GPS measurements. *Journal of Geodynamics*, 67, 30–39.

Masson F, Y. Hamiel, A. Agnon, Y. Klinger, A. Deprez, 2015, Variable behavior of the Dead Sea Fault along the southern Arava segment from GPS measurements. *C. R. Geoscience*, http://dx.doi.org/10.1016/j.crte.2014.11.001.

Meghraoui M., Gómez F., Sbeinati R., van derWoerd J., Mouty M., Darkal A. N., Radwan Y., Layyous I., Al Najjar H., Darawcheh R., Hijaz F., Al-Ghazzi R., Barazangi M., 2003, Evidence for 830 years of seismic quiescence from palaeoseismology, archeoseismology and historical seismicity along the Dead Sea fault in Syria. *Earth Planet. Sci. Lett.*, 210, 35–52.

Mohamad R., Darkal A. N., Seber D., Sandvol E., Gómez F., Barazangi M., 2000, Remote earthquake triggering along the Dead Sea fault in Syria, following the 1995 Gulf of Aqaba earthquake (M_S = 7.3). *Seismol. Res. Lett.*, 71, 47–52.

Nemer T. & Meghraoui M., 2006, Evidence of coseismic ruptures along the Roum fault (Lebanon): a possible source for the AD 1837 earthquake. *Journal of Structural Geology*, 28, 1483–1495.

Nemer T, Meghraoui M, Khair K., 2008, The Rachaya-Serghaya fault system (Lebanon): evidence of coseismic ruptures, and the AD 1759 earthquake sequence. *J. Geophys. Res.*, 113:B05312

Palano M., Imprescia P., and Gresta S., 2013, Current stress and strain-rate fields across the Dead Sea Fault System: Constraints from seismological data and GPS observations. *EPSL*, 369, 305-316.

Preliminary Seismological Bulletin, 1995, SNSN: Syrian National Seismological Network, General Establishment of Geology and Mineral Resources, Syria.

Reilinger R., and S. McClusky, 2011, Nubia Arabia Eurasia plate motions and the dynamics of Mediterranean and Middle East tectonics. *Geophys. J. Int.*, 186, 971–979.

Salamon A., Hofstetter A., Garfunkel Z., Ron H., 1996, Seismicity of the eastern Mediterranean region: perspective from the Sinai subplate. *Tectonophysics*, 263, 293–305.

Salamon A., Hofstetter A., Garfunkel Z., Ron H., 2003, Seismotectonics of the Sinai subplate–the eastern Mediterranean region. *Geophys. J. Int.*, 155, 149-173.

Salamon A., T. Rockwell, S. N. Ward, E. Guidoboni, and A. Comastri, 2007, Tsunami hazard evaluation of the eastern mediterranean: historical analysis and selected modeling. *Bul. Seis. Soc. Am.*, 97, 1–9, doi: 10.1785/0120060147.

Salamon A., 2009, Patterns of seismic sequences in the Levant interpretation of historical seismicity. *J. Seismology*, 14, 339–367.

Saleh M., Hamiel Y., Ziv A., Bock Y., Fang P., Wdowinski A., 2012, Crustal deformation along the Dead Sea Transform and the Carmel Fault inferred from 12 years of GPS measurements. *J. Geophys. Res.*, 117, B08410, http://dx.doi.org/10.1029/2012JB009241.

Sbeinati M. R. & Darawcheh R, 1997, Earthquakes in and around Syria during 1996, Bulletin No. 6, AECS-G\RSS 233

Sbeinati M. R. & Darawcheh R, 1998, Earthquakes in and around Syria during 1997, Bulletin No. 7, AECS-G\RSS 279.

SEISAN: THE EARTHQUAKE ANALYSIS SOFTWARE, Version 10.3, Jens Havskov and Lars Ottemöller, Department of Earth Science, University of Bergen, Allégaten 41, 5007 Bergen, Norway, 2015.

Tan O. and Taymaz T., 2003, Source Parameters of November 20, 1994 and December 24, 1996 Palmyra (Syria) Earthquakes, and Anology to the Dead Sea Transform Fault Zone (DSTFZ). International Workshop on the North Anatolian, East Anatolian and Dead Sea Fault Systems: Recent Progress in Tectonics and Paleoseismology and Field Training Course in Paleoseismology, P.118, Middle East Technical University (METU), 31 August – 12 September 2003, Ankara, Turkey.

Uski M., Tiira, Korja, Elo S., 2006, The 2003 earthquake swarm in Anjalankoski, south-eastern Finland. *Tectonophysics*, 422, 55–69.

Walley C. D., 1988, A braided strike-slip model for the northern continuation of the Dead Sea fault and its implications for Levantine tectonics. *Tectonophysics*, 145, 63-72.

Walley C. D., 1998, Some outstanding issues in the geology of Lebanon and their importance in the tectonic evolution of the Levantine region. *Tectonophysics*, 298, 37–62.

Walley C. D., 2001, The Lebanon passive margin and the evolution of the Levantine Neotethys. In, W. Cavazza, A.H.F. Robertson and P. Ziegler (Eds.), PeriTethyan rift/wrench basins and margins. Memoires du Muséum National d'Historie Naturelle, Paris, PeriTethys Memoir 6.

Wechsler N., T. K. Rockwell, Y. Klinger, P. Štěpančíková, M. Kanari, S. Marco, and A. Agnon, 2014, A Paleoseismic Record of Earthquakes for the Dead Sea Transform Fault between the First and Seventh Centuries C. E.: Nonperiodic Behavior of a Plate Boundary Fault. Bul. Seis. Soc. Am., 104, No. 3, doi: 10.1785/0120130304.

Yolsal S., Taymaz T., Yalçıner A. C., 2007, Understanding Tsunamis, Potential Source Regions and Tsunami Prone Mechanisms in the Eastern Mediterranean. The Geological Society of London, Special Publications Book, Vol: 291, ISBN: 978-1-86239-239-7, pp. 201-230.

Zanchi a., G. B. Crosta , A. N. Darkal, 2002, Paleostress analyses in NW Syria: constraints on the Cenozoic evolution of the northwestern margin of the Arabian plate. *Tectonophysics*, 357, 255–278.

Zollo A. & Bernard P., 1991, Fault mechanisms from near-source data : joint inversion of S polarization and P polarities. *Geophys. J. Int.*, 104, 441-451.

Geofísica Internacional (2018) 57-2: 139-150

Original paper

Single-particle statistics in the southern Gulf of Mexico

Luis Zavala Sansón*, Julio Sheinbaum and Paula Pérez-Brunius

Received: May 03, 2017; accepted: December 07, 2017; published on line: April 02, 2018

Resumen

Se presentan diferentes medidas estadisticas de boyas de deriva superficiales liberadas en el sur del Golfo de México. El estudio se enfoca en la estimación de las escalas Lagrangianas, en el cálculo de dispersión absoluta y en el análisis de las funciones de densidad de probabilidad de los registros de velocidad. Los valores de difusividad basados en las escalas Lagrangianas varían entre 6.9 y 8.8 10^7 cm^2/s. Las distribuciones obtenidas tienen los extremos muy extendidos por lo que no tienen una forma Gaussiana. Se muestra que esta característica está asociada con el giro de Campeche (una circulación ciclónica muy intensa que se presenta con frecuencia en la región) y, en menor medida, con un flujo a lo largo del margen oeste del Golfo. Los resultados se comparan con estudios que han reportado distribuciones Gaussianas y no Gaussianas en otras regiones.

Palabras clave: difusión oceánica, Golfo de México, boyas de deriva.

Abstract

Single-particle statistics of a large data set of surface drifters released in the southern Gulf of Mexico are presented. The study is focused on the estimation of Lagrangian scales, the calculation of absolute dispersion and the analysis of probability density functions of velocity records. Diffusivity values based on the Lagrangian scales range from 6.9 to 8.8 10^7 cm^2/s. The probability distributions display a non-Gaussian shape with extended tails. It is shown that the long tails are mainly associated with the Campeche gyre (an intense cyclonic circulation frequently formed in the region) and, to a lesser extent, with a flow along the western margin of the basin. The results are discussed in the light of previous studies on ocean dispersion reporting Gaussian and non-Gaussian distributions in other regions..

Key words: dispersion, Gulf of Mexico, surface drifters.

L. Zavala Sansón*
J. Sheinbaum
P. Pérez-Brunius
Departamento de Oceanografía Física
Centro de Investigación Científica
y de Educación Superior de Ensenada
Carretera Ensenada-Tijuana 3918
Zona Playitas, 22860
Ensenada, Baja California, México.
Corresponding author: lzavala@cicese.mx

Introduction

The properties of a turbulent flow can be analyzed by measuring the dispersion of passive particles or tracers. Based on this idea, several studies have examined the turbulent character of the oceans and the atmosphere by releasing a number of drifters or substances that are advected by the flow (Griffa *et al.* 1995). Surface and subsurface drifters (the latter reaching depths of hundreds and even a few thousand meters) are commonly used to study oceanic dispersion at different temporal and spatial scales (LaCasce, 2008). Since the 1960s, controlled dye-release experiments in the ocean mixed layer have been carried out (Okubo, 1971). In the atmosphere, constant level balloons advected by the winds at different heights (*e. g.* the 200 mb-level) are often used to study their dispersion (LaCasce, 2010). Once the data set has been collected, either in a single campaign or during several observational periods, the statistical properties of the dispersion are calculated.

Different statistical analysis can be performed with the position and velocity components, such as single-particle statistics (with individual drifters) or two-particle statistics (with drifter pairs; see LaCasce, 2008). A fundamental tool for this purpose are the probability density functions (PDFs) of positions and velocities, which allow the calculation of statistical moments of the data records (*e. g.* dispersion, skewness, kurtosis).

The velocity PDFs might have a Gaussian or a non-Gaussian shape, which indicates how to parameterize dispersive properties of the turbulent flow. For instance, the evolution of a tracer concentration is often modeled with an advection-diffusion equation in an Eulerian framework, where the flow is decomposed into a large-scale flow, responsible for the advection, and a turbulent component associated with the diffusion (Griffa, 1996). Then, the 'eddy diffusivity' associated with the small-scale motions is parameterized with Lagrangian data, that is, by calculating the statistical behavior of a number of particles advected by the flow. The generalized advection-diffusion model of Davis (1987) requires the velocity PDFs to be Gaussian or nearly-Gaussian. In order to apply this model, Swenson and Niiler (1996) computed the velocity PDFs from the California Current and reported a Gaussian shape in most of their samples. Surface velocities calculated from satellite altimetry also show a Gaussian distribution (Gille and Llewellyn-Smith, 2000). However, other studies have shown that the PDFs can be strongly non-Gaussian for subsurface floats in the North Atlantic Ocean (Bracco *et al.,* 2000a; LaCasce, 2005) and in the surface of the Mediterranean Sea (Isern-Fontanet *et al.,* 2006). Such distributions are characterized by long tails, which indicate the presence of infrequent, but very energetic circulation events. In the ocean, these events are associated with intense mesoscale vortices and jets.

The shape of the velocity PDFs has been thoroughly studied in two-dimensional turbulent flows, where energetic coherent structures are formed due to the inverse energy cascade that characterizes this type of turbulence (Provenzale, 1999; Bracco *et al.,* 2000b). If the Reynolds number is moderate, and hence the vortices are relatively slow, the PDFs might be Gaussian or nearly-Gaussian. By contrast, for a large Reynolds number very intense vortices are generated and the PDFs might be clearly non-Gaussian (Bracco *et al.,* 2000b). Based on this, Pasquero *et al.* (2001) parameterized dispersive effects by using a suitable stochastic model that reproduces the non-Gaussian shape of the PDFs. Summarizing, transport processes can be very different depending on the shape of the velocity distributions, and it is therefore relevant to determine the PDFs in dispersion studies.

In this article we calculate single-particle statistics from a large set of surface drifters released in the southern Gulf of Mexico (hereafter GM). In particular, we estimate diffusivity scales and compare them with those reported in other regions. Afterwards we analyze the velocity PDFs and find that the distributions have extended wings, which represent infrequent, high energy velocity records (with respect to the mean). With this analysis we are able to identify the most energetic regions that generate the non-Gaussian distributions, and to show that these correspond to the semi-permanent cyclonic gyre in the Bay of Campeche and to the intense narrow flows along the western margin.

In previous studies we examined two-particle statistics (Zavala Sansón *et al.,* 2017a) and dispersion from localized areas regarded as point sources (Zavala Sansón *et al.,* 2017b), so the present work completes a series of Lagrangian analyses in the southern GM. These studies constitute an observational baseline for future observational and numerical Lagrangian studies in this region. One of the main motivations for gathering this information is to provide robust statistical results from a large drifter database that may shed some light on how to parameterize Lagrangian dispersion. For instance, operational numerical models that

simulate particle dispersion can be evaluated by examining their ability to reproduce at least some of the statistics presented in these studies (PDFs, Lagrangian scales, dispersion curves).

The paper is organized as follows. The data set is briefly described in Drifter database section. Calcultions of single-particle statistics (mean fields, integral time scales and absolute dispersion) are shown in Results section. Afterwards, the velocity PDFs and the energetic circulations responsible for the non-Gaussian shape of the distributions are analyzed. Finally, in the last section, the results are discussed.

Drifter database

Lagrangian data were obtained during a long-term observational program in the southern GM, developed by the Mexican oil industry (PEMEX and CICESE, Mexico). The drifter database has been used to describe general features of the southern and western circulation of the GM (Pérez-Brunius *et al.,* 2013), and to estimate two-particle statistics (Zavala Sansón *et al.,* 2017a,b). It has also been used to examine the connectivity between the Bay of Campeche and the rest of the GM (Rodríguez-Outerelo, 2015). Detailed information on the drifters' performance and several pre-processing steps are described in those studies. Here a brief account of the results shown in the next section is presented.

Between September 2007 and September 2014, a total of 441 surface drifters (Far Horizon Drifters, Horizon Marine Inc.) were released by aircraft in different locations of the southern GM. The drifters consist of a cylindrical buoy attached to a parachute that serves as drogue at a nominal depth of 50 m when the buoy drifts in the water. It is estimated that the drifters effectively follow oceanic currents below the surface Ekman layer. The geographical positions were tracked with a GPS receiver recording hourly positions. The data were filtered and interpolated to regular 6 h intervals. On average, there were about 63 launches per year, and 5 or 6 per month. The average lifetime of the drifters is 62 days with a standard deviation of 47 days. The longest record was 218 days.

Most drifters were released near five preferential locations between 19° and 20° N, and 96° and 93° W (see detailed maps in Zavala Sansón *et al.,* 2017a,b). Figure 1 shows the drifter trajectories up to 30 days, in order to illustrate their spatial distribution. The panels present the trajectories of 356 drifters starting from the preferential spots (panels a to e) and 85 drifters that started elsewhere (panel f). The first 15-day segments are colored differently than the subsequent sections.

Most drifters were retained in the south during the first 15 days, many of them trapped in the Campeche gyre, the semi-permanent cyclonic circulation at the Bay of Campeche (Monreal-Gómez and Salas de León, 1997; Pérez-Brunius *et al.,* 2013). This is particularly clear at the western spots (panels a, b and d). When the drifters escape northwards during the subsequent 15 days, they do it preferentially along the western margin of the GM. On the eastern side, very few drifters were able to reach the Yucatan shelf, beyond 92.5° W.

Results

Mean field

For the 84-month, 104232 drifter positions and velocities were recorded. The number of records in a regular grid of 0.25° resolution is plotted in Figure 2a. Only geographical bins having a number of records larger than 30 were considered (Bracco *et al.,* 2000a). The number of records is greater in the southern part (below 22° N), where most of the drifters were released. Note that some regions of the GM are sub-sampled, such as the eastern part and the Yucatan shelf. The reason is because drifters released at the southern GM barely transit over these regions. By interpolating the velocity records onto the grid (with mxn nodes) the mean velocity field (u^{mn}, v^{mn}) was generated, conformed by the zonal and meridional components, respectively (Figure 2b). A relevant feature is the cyclonic gyre at the Bay of Campeche, which reveals the extraordinary persistence in time of this structure. Another important feature is the northward flow along the western margin, between 22° and 26 ° N, which is associated with a northward advection of drifters observed in previous works (Pérez-Brunius *et al.,* 2013; Zavala Sansón *et al.,* 2017a,b).

The kinetic energy field (per mass unit)

$$E^{mn} = \frac{1}{2}\left[\left(u^{mn}\right)^2 + \left(v^{mn}\right)^2\right] \qquad (1)$$

is shown in Figure3a. The field is normalized with the mean value of the whole velocity records, E = 0.0624 m^2/s^2. The highest values are concentrated at the western margin and at the northern side. Some areas in the southern and central regions are also very energetic (about 1.5 times the mean value). The variance of the velocity field is presented in Figure 3b. High values are found at the western coast, indicating

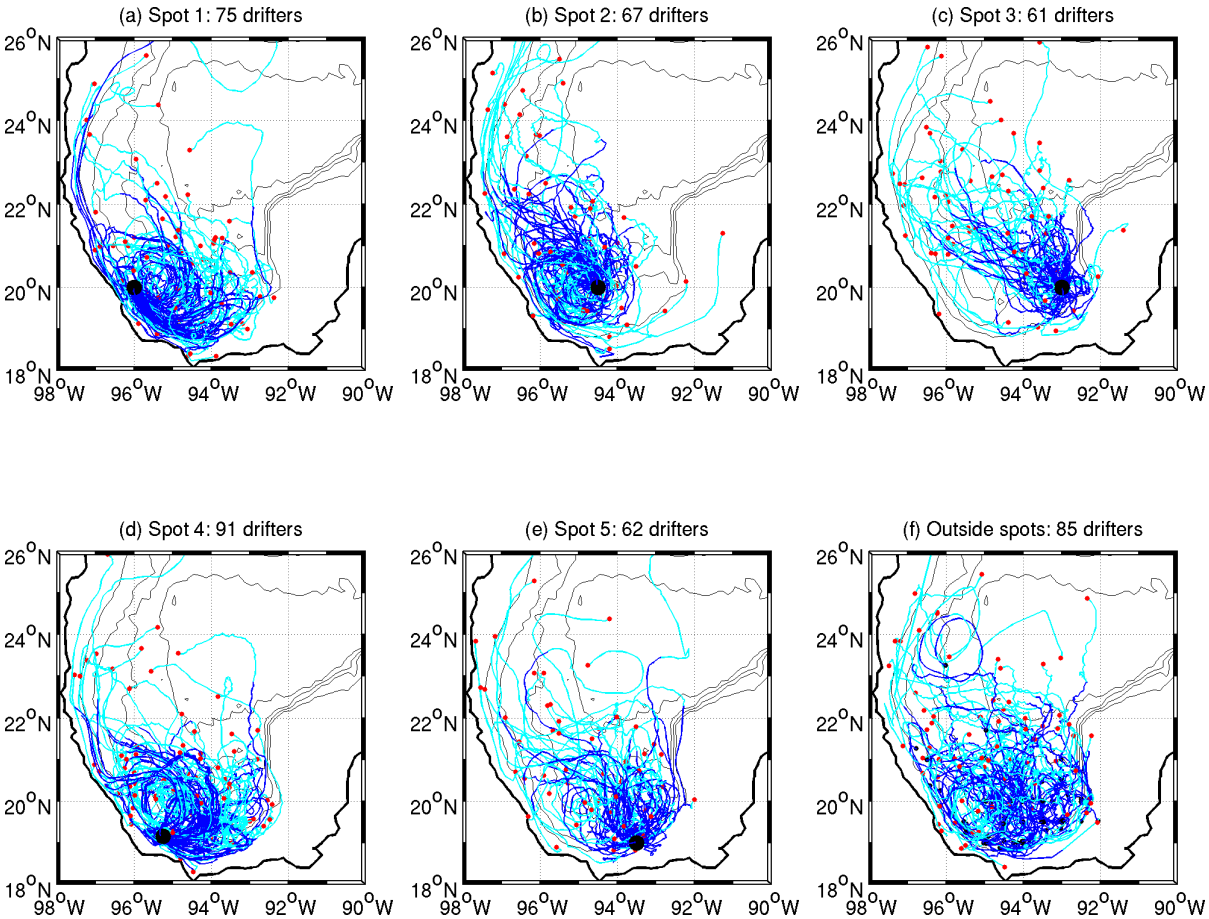

Figure 1. Trajectories of 441 drifters released in the southern GM. Panels (a) to (e) show the trajectories of 356 drifters released at five special locations denoted with a big black dot in each panel. 85 more drifters where released elsewhere (panel f). The maximum duration of the trajectories was 30 days. The first 15 days are colored in blue; subsequent days are colored in cyan. Small, black (red) dots indicate the initial (final) position of drifters. Topography contours (500, 1500, 2500 and 3500 m) are denoted with thin black lines.

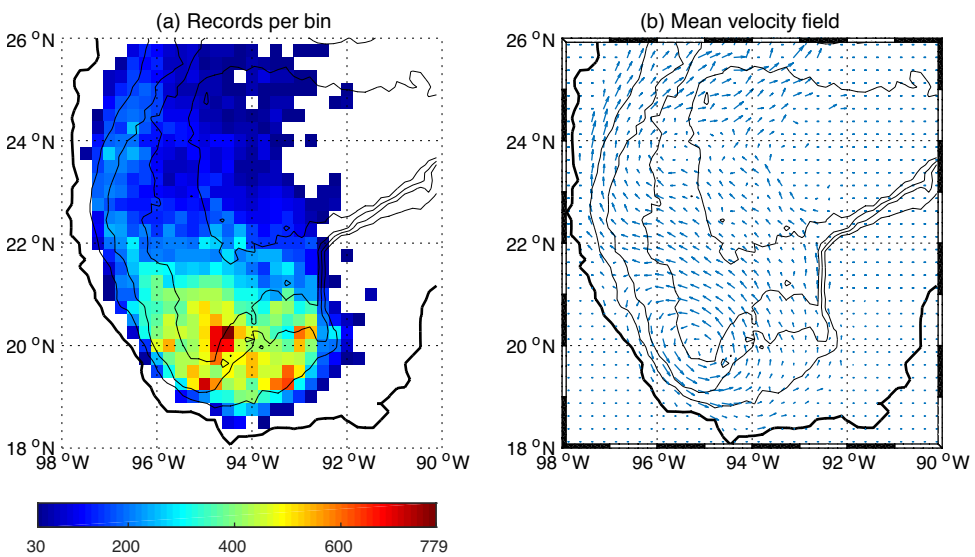

Figure 2. (a) Data records per geographical bin in a 0.25° 0.25° grid. Bins with less than 30 records are left blank. (b) Eulerian velocity field calculated from the mean records at each bin. Maximum velocity magnitude was 0.4 m/s.

the important variability of alongshore currents. In fact, even though the mean flow shows a south-to-north direction, the boundary flow can reverse its direction from north-to-south depending on the along-coast winds or due to the collision of mesoscale eddies with the shelf (Zavala-Hidalgo *et al.* 2003; Dubranna *et al.,* 2011; Zavala Sansón *et al.,* 2017a).

Lagrangian scales and absolute dispersión

The drifter velocity components at time t are denoted as $u_i(t)$, where $i = 1,2$ indicates the zonal and meridional directions, respectively. Lagrangian scales are calculated with residual velocities obtained by subtracting the Eulerian mean flow as the particles transit over geographical bins

$$u_i(t) = u_i'(t) - u_i^{mn}. \quad (2)$$

Then, the 'memory' of the drifter is calculated with the Lagrangian autocovariance function defined as (Provenzale, 1999)

$$R_{ii}(\tau) = \lim_{T\to\infty} \frac{1}{T} \left\langle \frac{1}{\sigma_i^2} \int_0^T u_i'(t) u_i'(t+\tau)\, dt \right\rangle, \quad (3)$$

where σ_i^2 is the velocity variance and $<*>=(1/N)\,\Sigma*$ indicates ensemble average over N particles. The Lagrangian integral time is formally defined as $T_i^L = \int_0^\infty R_{ii}(\tau)d\tau$. For a random process the integral converges as $R_{ii}(\tau)$ drops to zero. In practice, the integral time is usually calculated by integrating the autocorrelation function up to the first zero crossing time t_Z (Poulain and Niiler, 1989; Zavala Sansón, 2015)

$$T_i^L = \int_0^{t_z} R_{ii}(\tau)\, d\tau\,. \quad (4)$$

Lagrangian length and diffusivity scales are defined as

$$L_i = \langle\, \sigma_i \,\rangle\, T_i^L, \qquad K_i = L_i^2 \big/ T_i^L, \quad (5)$$

where the velocity standard deviation $<\sigma_i>$ is calculated at time T_i^L.

Figure 4 shows plots of the autocorrelation function for each velocity component (panel a), and the corresponding Lagrangian integral time (panel b). It is found that T_1^L~1.5 and T_2^L~1.5 days. The Lagrangian timescales are L_1~30 km and L_2~36 km. Diffusivity scales are K_1~6.9x10^7 and K_2~8.8x10^7 cm²/s.

Absolute dispersion, which is based on the mean-squared separation of particles from their position at a reference time t_0 was calculated. Let $x_i(t)$ be the position of particles in the i-direction at time t. Using N Lagrangian trajectories, absolute dispersion is (Provenzale, 1999)

$$\overline{A_i^2} = \left\langle \left[x_i(t) - x_i(t_0) \right]^2 \right\rangle. \quad (6)$$

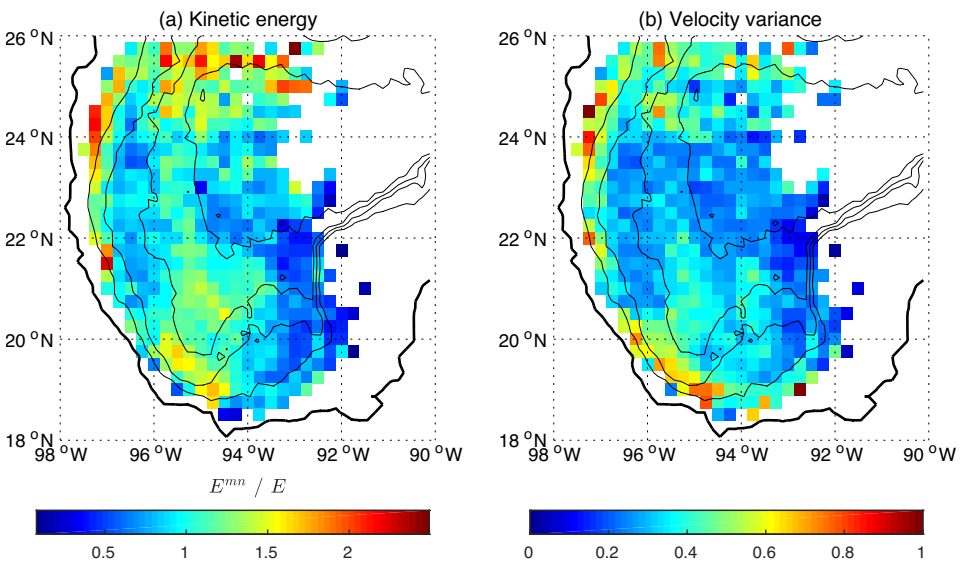

Figure 3. (a) Kinetic energy field normalized with the mean value of the velocity records E=0.0624 m²/s². (b) Normalized variance of the velocity field. Bins with less than 30 records were left blank.

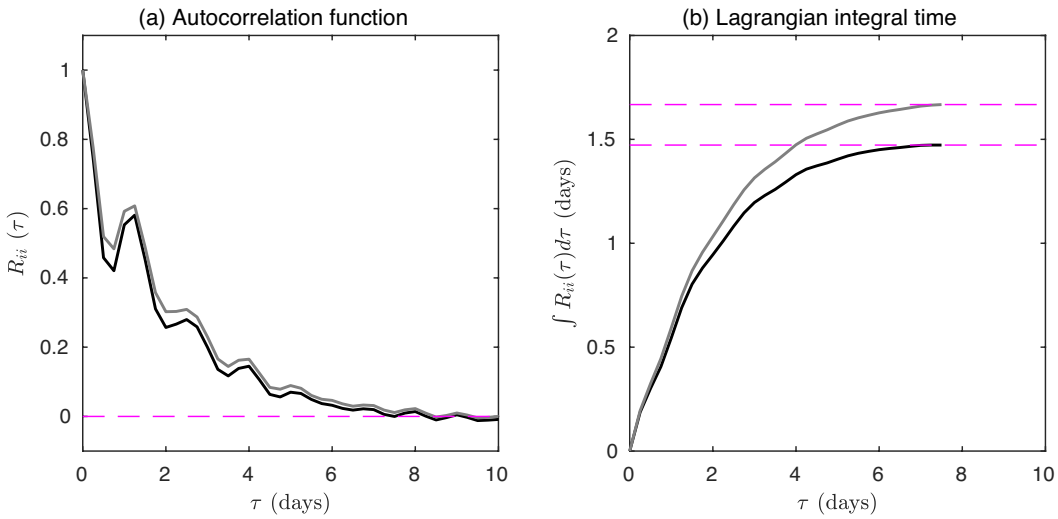

Figure 4. (a) Lagrangian velocity autocovariance for zonal (black line) and meridional (gray line) data. Horizontal dashed line indicates the zero. (b) Integral of the autocovariance calculated up to the first zero crossing for both components. Horizontal dashed lines indicate the value of the Lagrangian integral time.

The asymptotic behavior for "short" times $t \ll T_i^L$ is the quadratic, ballistic regime in which dispersion grows as t^2. For "long" times $t \gg T_i^L$ dispersion grows linearly in time in a random-walk or standard dispersion regime (Taylor, 1921). Absolute diffusion is defined as the temporal evolution of the dispersion

$$K_i = \frac{1}{2}\frac{d}{dt}\overline{A_i^2}\,. \qquad (7)$$

For drifters with a long lifetime with respect to the integral timescale, it is possible to increase the number of degrees of freedom by making subdivisions of the trajectories in segments with a duration longer than T_i^L. This is a reasonable period after which every segment can be considered as an independent trajectory (Poulain and Niiler, 1989). Using segments that are 10 days long, about 2500 'trajectories' from the 441 original tracks were initially obtained.

Figure 5a presents the absolute dispersion components as a function of time. Between 0.25 and 3 days both components grow at the same rate, approximately. Within this time interval a quadratic curve is drawn, showing that the

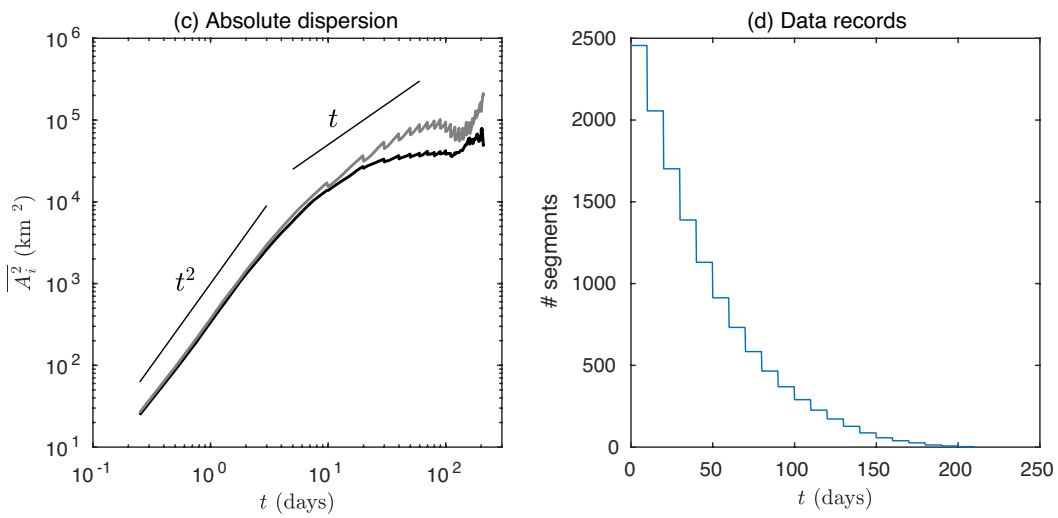

Figure 5. (a) Absolute dispersion components (zonal: black; meridional: gray) vs. time. For clarity, confidence intervals are not shown. The quadratic curve is drawn between 0.25 and 3 days, while the linear curve is drawn between 5 and 60 days. (b) Number of segments used to calculate absolute dispersion as a function of time.

growth is nearly ballistic. At later times, between 5 and 60 days, the meridional component is approximately linear, indicating a random-walk regime. In contrast, the zonal component is limited by the western margin of the GM and hence its growth is slower than t. When using the 441 trajectories instead of the set of segments the results are very similar (not shown). Figure 5b shows the number of available segments as time evolves, about 2500 during the first 10 days, and up to 850 at day 60.

Probability density functions

The raw velocity PDFs using the velocity records without any modification is initially presented. Figures 6a-b shows the distributions in the zonal and meridional directions, respectively. Superposed to the empirical data a Gaussian distribution with the same standard deviation and zero mean for each component is plotted:

$$P(u_i) = \frac{1}{(2\pi)^{1/2}\sigma_i} e^{-u_i^2/2\sigma_i^2} . \qquad (8)$$

The extended tails suggest a non-Gaussian shape of the distributions. Considering that these deviations might be due to the presence of intense mean flows and not to turbulent dispersion, the velocity records are corrected in order to compensate the additional advection due to such motions. We follow the procedure used by Bracco *et al.* (2000a), which consists of dividing the region of study in geographical bins (here the 0.25° 0.25° square grid considered above was used) discarding those with less than 30 velocity records. The Eulerian velocity is subtracted from each velocity record at the corresponding bin, as in equation (2), and the result is normalized with the standard deviation, so the new variables are u_i'/σ_i. Finally, all the realizations are used to generate the re-scaled

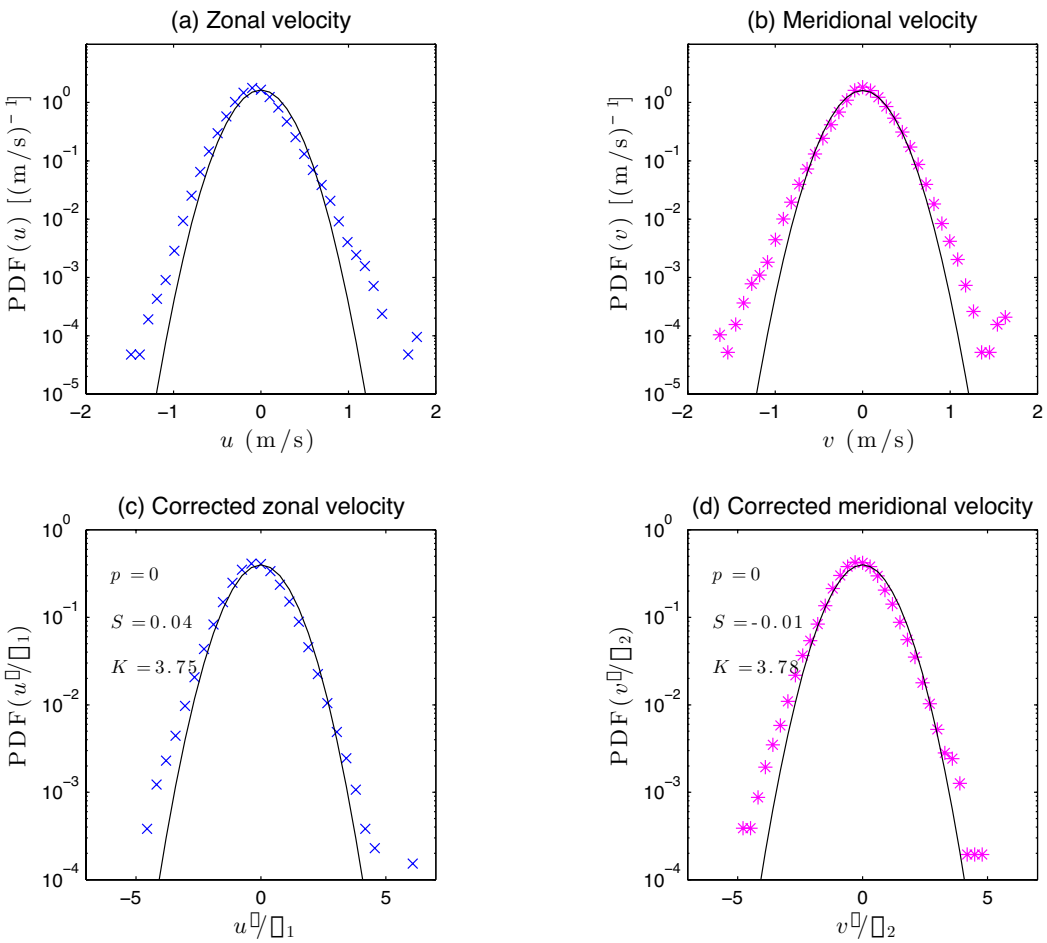

Figure 6. Velocity PDFs for (a) zonal (crosses) and (b) meridional (stars) records. Solid lines indicate the normal distribution (8). Corrected PDFs for both directions are shown in panels (c) and (d), respectively. Numbers in lower panels show the KS probability p, the skewness S and the kurtosis K.

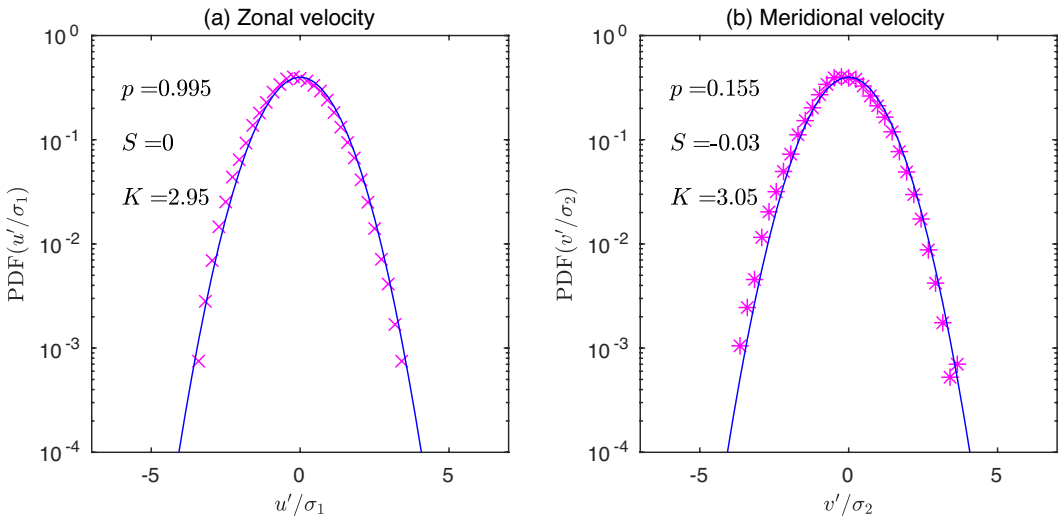

Figure 7. Low-energy velocity PDFs calculated with a threshold for (a) zonal (crosses) and (b) meridional (stars) records. Solid lines and numbers as in Figure 6.

PDFs for the whole region. The results for the zonal and meridional velocity components are shown in Figures 6c-d. The skewness is close to zero in both cases and the kurtosis is nearly 3.8. Since the kurtosis of a normal distribution is 3, these results suggest that the corrected PDFs are not Gaussian (which is again evident from the extended tails).

In order to quantify the Gaussian part of these distributions, the Kolmogorov-Smirnov (KS) test was used (Beron-Vera and LaCasce, 2016; Zavala Sansón *et al.* 2017 PONER a o b). The samples must be statistically independent, which is achieved by taking data every integral time-scale (LaCasce, 2005). Thus, only samples every 1.5 days were used, so the remaining records are 17231, approximately 1/6 of the total. The null hypothesis postulates that the distribution is sufficiently Gaussian when the KS probability p (associated with the maximum difference between the cumulative distribution of the empirical data and a Gaussian) is greater than the significance level α, chosen as 0.05. The KS probabilities for the zonal and meridional re-scaled PDFs are $p = 2.3\text{x}10^{-4}$ and $p = 7.3\text{x}10^{-6}$, respectively, and therefore the KS test confirms that these distributions are not Gaussian.

The extended tails of the PDFs are associated to infrequent but very energetic events that are mostly related with the presence of intense mesoscale features in the region. In order to show this, data subsets in which the most energetic records are subtracted were considered. The idea is to show that in such cases the PDFs tend to be Gaussian. The velocity records with "low" energy values are those whose energy is lower than sE, where E is the mean energy of the whole set (see Section 3.1) and the threshold is a positive real number. In Figures 7a-b the corrected PDFs for a low-energy subset with (16732 records) are presented, that is, the kinetic energy of each record is smaller than $3E$. According to the KS test, both PDFs are Gaussian, because the KS probability p is larger than 0.05 and the corresponding kurtosis is nearly 3. This demonstrates that the low energy records have a normal PDF, and that the infrequent events in the tails of the whole distributions are indeed high energy records.

The KS test is applied to several low-energy subsets generated with different values. The results are presented in terms of the normalized energy of the records that are removed, that is, the high-energy fraction HEF. To define this number the total energy E_T of the whole set of records and the mean energy E were calculated. Then the threshold s was set and the total energy E_{low} (E_{high}) of the records whose energy is lower (greater) than sE was calculated. Since $E_T = E_{low} + E_{high}$ then HEF is

$$HEF = \frac{E_{high}}{E_T} = 1 - \frac{E_{low}}{E_T}. \qquad (9)$$

The KS test is applied for HEF between 0 and 0.81, approximately, which corresponds with thresholds $s = 40/q$, where $q = 1, 2, 3 \ldots 50$.

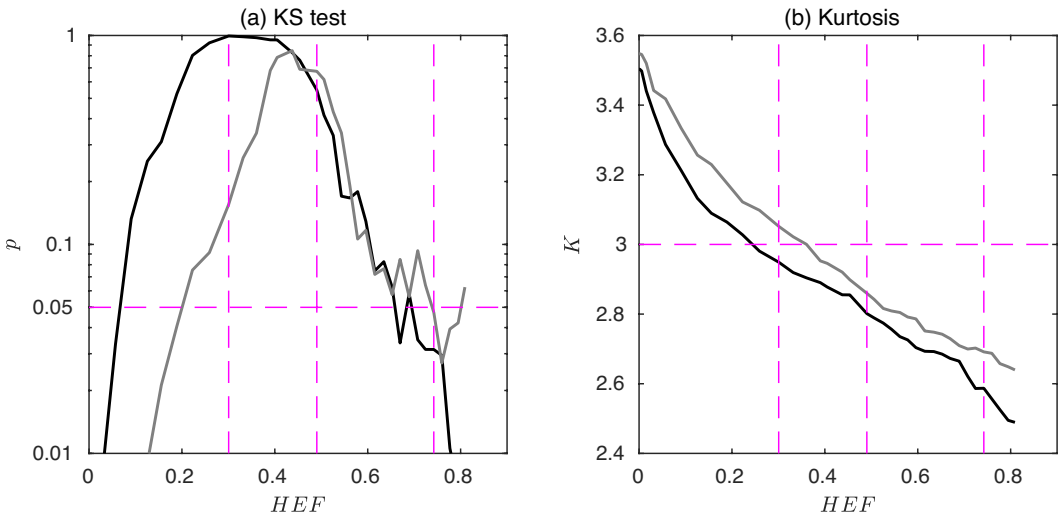

Figure 8. (a) Kolmogorov-Smirnov probability as a function of HEF defined in (9). The result of the test for the zonal (meridional) component is indicated with a black (gray) solid line. The horizontal dashed line represents the confidence level (0.05). The vertical dashed lines correspond to threshold values 3, 2 and 1 (from left to right). (b) Kurtosis of the distributions (line colors and styles as in previous panel). The value for a normal distribution (3) is indicated with a horizontal dashed line.

Figures 8a-b present the KS probability and the kurtosis as a function of HEF for the zonal and meridional directions. For small HEF it is verified that the PDFs are non-Gaussian (p<0.05 and K>3). This is expected because the distributions are not Gaussian $HEF = 0$ when (*i. e.* when no records are removed, see Figures 6c-d). For intermediate HEF values, say between 0.1 and 0.6, the distributions become Gaussian (p>0.05 and K~3). The first vertical dashed line at HEF~0.3 indicates the case of the PDFs shown in Figures 7a-b, where the threshold value is $s = 3$. The second and third vertical lines (HEF~0.5 and 0.75) correspond to cases with $s = 2$ and $s = 1$, respectively. For larger HEF the PDFs become non-Gaussian again (p<0.05 and K<3), but now the reason is the reduced number of degrees of freedom as more and more records are subtracted (these later cases are of no interest).

The geographical distribution of low and high energy records gives additional information, as shown in Figure 9 for the case with $s = 2$.

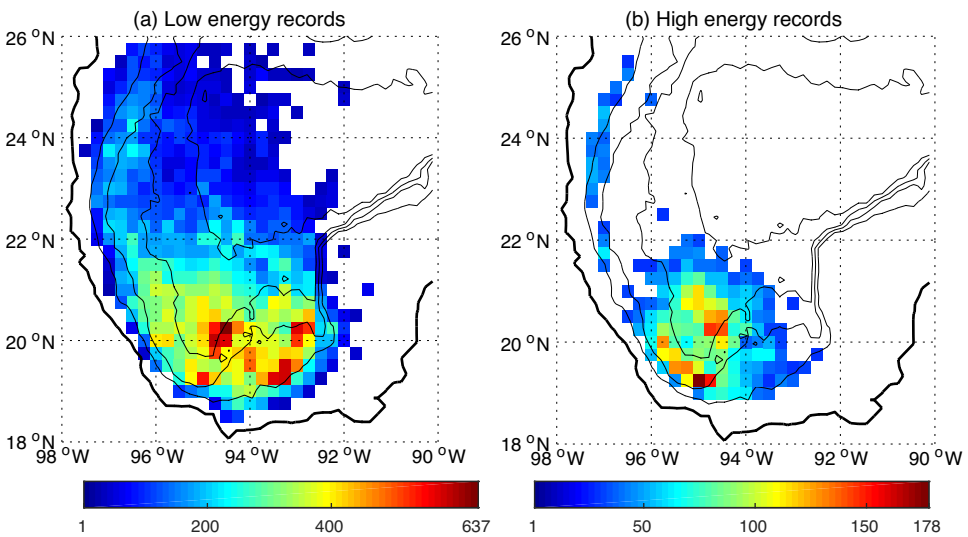

Figure 9. (a) Low energy and (b) high energy records per geographical bin when using a threshold s=2 (see text). Bins with less than 30 records are left blank.

The number of low energy records are found over almost the entire region, with maximum values at the Bay of Campeche (panel a). High energy records (panel b) are mainly located at the Bay of Campeche and a few more along the western boundary of the GM. This shows that very energetic records, responsible for the non-Gaussian form of the complete PDFs, are associated with the cyclonic gyre in Campeche and with the alongshore flow in the western margin.

Discussion

Lagrangian time, length and diffusivity scales were calculated from drifter records obtained during a 7-year period in the southern GM. The resulting diffusivities (from 6.9 to 8.8×10^7 cm^2/s) are now compared with similar calculations reported in previous studies for different regions of the GM.

Ohlmann and Niiler (2005) made estimations for the Texas-Louisiana and northwest Florida shelves during the SCULP experiments performed during the 1990s. Diffusivities over the Texas-Louisiana shelf range from 6.4×10^6 for inshore locations to 2.2×10^7 cm^2/s for offshore areas. Over the west Florida shelf, diffusivities were somewhat larger, ranging from 3.1 to 6.5×10^7 cm^2/s. Thus, diffusivities for the northern shelves of the GM are lower than the ones reported here, presumably because of the nearness to the coast.

More recently, Mariano *et al.* (2016) calculated Lagrangian statistics at coastal and offshore regions in the northeastern GM, using drifters from the GLAD experiment carried out in 2012. Horizontal diffusivity estimates near the coast and over the shelf are of order 10^7 to 10^8 cm^2/s. In offshore areas under the influence of the Loop Current diffusivities mostly range between 1 and 4×10^8 cm^2/s, reaching peak values up to 2×10^9 cm^2/s. These large values (greater than those found in the southern GM) are apparently due to the considerable magnitude of the Loop Current and the subsequent formation of strong mesoscale eddies in eastern GM.

Using two-particle statistics, Zavala Sansón *et al.* (2017a) calculated relative diffusivities in the southern GM (relative diffusivity is two times the absolute diffusivity for large particle separations (LaCasce, 2008). Their results range from 10^6 cm^2/s for small drifter separations (about 2 km) to 2×10^8 cm^2/s for larger separations (150-300 km). Recall, however, that these estimates are statistical values over a large set of drifters released at different times and locations. In other words, dispersion processes might change dramatically depending on the dominant circulation and this may lead to different dispersion scenarios, as described by Zavala Sansón *et al.* (2017a,b).

The examined shapes of the velocity PDFs, provide relevant information on the Lagrangian data and, consequently, on dispersion and diffusion properties. The velocity PDFs have a non-Gaussian shape characterized by long tails (with kurtoses of about 3.8). The non-Gaussian characteristic is associated with the presence of energetic circulation events, which generate the long tails of the distributions. This form of the PDFs has been discussed in dispersion studies for different oceanic regions (Bracco *et al.,* 2000a; LaCasce, 2005; Isern-Fontanet *et al.,* 2006) and in numerical simulations of two-dimensional turbulence (Bracco *et al.,* 2000b; Pasquero *et al.,* 2001).

One of the main mesoscale circulation features that characterizes the southern GM is the cyclonic gyre at the Bay of Campeche, which is clearly observed in the drifter trajectories and in the mean velocity field (Figures 1 and 2, respectively). It was shown that the PDFs become Gaussian when high-velocity records are removed, and that such a subset of records is indeed located in the area where the cyclonic gyre is usually formed (Figure 9). In other words, this circulation is apparently the main cause of the PDFs extended wings. Intense velocity records along the western margin were also found, associated with an alongshore flow frequently observed there (see e. g. Zavala-Hidalgo *et al.,* 2003). When flowing northward, these currents have also been related with the arrival of Loop Current Eddies from the eastern GM (Pérez-Brunius *et al.,* 2013) and the consequent south-to-north dispersion of drifters (Zavala Sansón *et al.,* 2017a,b).

The identification of very energetic regions in the southern GM (with respect to the mean) points out that any parameterization has to take into account the influence of the intense circulations found there. Therefore diffusivity values calculated with the whole set of drifters might be underestimated in the regions with high energy records. In other words, high energy motions might generate anomalous, super-diffusive effects that cannot be parameterized with standard random-walk models (which generate Gaussian velocity distributions). The formulation of stochastic models that are able to reproduce non-Gaussian PDFs are scarce [see e. g. Pasquero *et al.* (2001) in the context of 2D turbulence] and such an approach should be followed in oceanic models.

References

Beron-Vera, F. J. and J. H . LaCasce, 2016. Statistics of simulated and observed pair separations in the Gulf of Mexico. *J. Phys. Oceanogr*., 46, 2183-2199.

Bracco, A., LaCasce, J.H. and Provenzale, A., 2000a. Velocity probability density functions for oceanic floats. *J. Phys. Oceanogr*., 30, 461-474.

Bracco, A., LaCasce, J., Pasquero, C. and Provenzale, A., 2000b. The velocity distribution of barotropic turbulence. *Phys. Fluids*, 12, 2478-2488.

Davis, R.E., 1987. Modeling eddy transport of passive tracers. *J. Mar. Res*., 45, 635-666.

Dubranna, J., P. Pérez-Brunius, M. López, and J. Candela, 2011. Circulation over the continental shelf of the western and southwestern Gulf of Mexico. *J. Geophys. Res*., 116 C08009.

Gille, S. T., and S. G. Llewellyn Smith, 2000. Velocity probability density functions from altimetry. *J. Phys. Oceanogr*., 30, 125-136.

Griffa, A., Owens, K., Piterbarg, L. and Rozovskii, B., 1995. Estimates of turbulence parameters from Lagrangian data using a stochastic particle model. *J. Mar. Res*., 53(3), 371-401.

Griffa, A., 1996. Applications of stochastic particle models to oceanographic problems. In *Stochastic modelling in physical oceanography*, Birkhauser Boston, 113-140,

Isern-Fontanet, J., E. García-Ladona, J. Font, and A. García-Olivares, 2006. Non-Gaussian velocity probability density functions: an altimetric perspective of the Mediterranean Sea. *J. Phys. Oceanogr*., 36, 2153-2164.

LaCasce, J.H., 2005. Eulerian and Lagrangian velocity distributions in the North Atlantic. *J. Phys. Oceanogr*., 35, .2327-2336.

LaCasce, J.H., 2008. Lagrangian Statistics from Oceanic and Atmospheric Observations. *Lect. Notes Phys*., 744, 165-218.

LaCasce, J.H., 2010. Relative displacement probability distribution functions from balloons and drifters. *J. Mar. Res*., 68, 433-457.

Mariano, A. J., *et al.,* 2016. Statistical properties of the surface velocity field in the northern Gulf of Mexico sampled by GLAD drifters. *Geophys. Res. Lett*., 121, 7, 5193-5216.

Monreal-Gómez, M. A., and D. Salas de León, 1997: Circulación y estructura termohalina del Golfo de México. Contribución a la Oceanografía Física en México, M. Lavin, Ed., Monografía de la Unión Geofísica Mexicana, Vol. 3, Unión Geofísica Mexicana, 183–199.

Ohlmann, J. C. and P. P. Niiler, 2005. Circulation over the continental shelf in the northern Gulf of Mexico. *Prog. Oceanogr*., 64, 45-81.

Okubo, A., 1971. Ocean diffusion diagrams. *Deep Sea Res*., 18, 789-802.

Pasquero, C., A. Provenzale and A. Babiano, 2001. Parameterization of dispersion in two-dimensional turbulence. *J. Fluid Mech*., 439, 279-303.

Pérez-Brunius, P., García-Carrillo, P., Dubranna, J., Sheinbaum, J., and Candela, J., 2013. Direct observations of the upper layer circulation in the southern Gulf of Mexico. *Deep Sea Res. Part II: Topical Studies in Oceanography*, 85, 182-194.

Poulain, P. M. and P. P. Niiler, 1989. Statistical analysis of the surface circulation in the California current system using satellite-tracked drifters. *J. Phys. Oceanogr*. 19, 1588-1603.

Provenzale, A., 1999. Transport by coherent barotropic vortices. *Ann. Rev. Fluid Mech*., 31, 55-93.

Rodríguez Outerelo, J., 2015. Conectividad del golfo de Campeche con el resto del golfo de M\'exico a partir de datos lagrangianos reales y simulados. (in Spanish). M. S. thesis, CICESE, Mexico, 58 pp. Available from CICESE library www.cicese.edu.mx.

Swenson, M.S. and Niiler, P.P., 1996. Statistical analysis of the surface circulation of the California Current. *J. Geophys. Res*., 101, 22,631-22,645.

Taylor, G. I., 1921. Diffusion by continuous movements. Proc. London math. Soc., 20, 196-212.

Zavala-Hidalgo, J. S., L. S. Morey, J. J. O'Brien, 2003. Seasonal circulation on the western shelf of the Gulf of Mexico using a high-resolution numerical model. *J. Geophys. Res*., 108 (C12), 3389.

Zavala Sansón, L., 2015. Surface dispersion in the Gulf of California. *Progr. Oceanogr*., 137, A, 24-37.

Zavala Sansón, L., P. Pérez-Brunius and J. Sheinbaum, 2017a. Surface relative dispersion in the southwestern Gulf of Mexico. *J. Phys. Oceanogr*., 47(2), 387-403.

Zavala Sansón, L., P. Pérez-Brunius and J. Sheinbaum, 2017b. Point source dispersion of surface drifters in the southern Gulf of Mexico. *Environ. Res. Lett*., 12, 024006.

Geofísica Internacional (2018) 57-2: 151-160

Original paper

Amplitude versus offset (AVO) modelling and analysis for quantitative interpretation of porosity and saturation: A case study for Sawan gas field, middle Indus basin, Pakistan

Muhammad Rizwan*, Gulraiz Akhter, Ali Mustafa, Umair Bin Nisar and Khawar Ashfaq

Received: January 17, 2017; accepted: February 08, 2018; published on line: April 02, 2018

Resumen

En términos de monitoreo los parámetros importantes del yacimiento son la porosidad y la saturación de agua, que a su vez son necesarios para la ubicación de futuros pozos de producción. La técnica de modelado y análisis de amplitud versus compensación (AVO, por sus siglas en inglés) se ha utilizado para la interpretación cuantitativa de la porosidad y la saturación de agua. Gassmann utilizó, para el modelado AVO, el modelo de sustitución de fluidos en conexión con recolectores de ángulo sísmico 2D para el control de yacimientos sobre los pozos Sawan-4 y Sawan-7. Los resultados del modelo de AVO mostraron un aumento significativo del registro de densidad al sustituir el gas por agua, además del aumento moderado de la velocidad de la onda P y ningún cambio en la velocidad de la onda S. El modelado AVO demostró una fuerte relación entre la porosidad y la amplitud de reflexión para todos los rangos de desplazamiento. La anomalía de clase IV fue evidente para todas las porosidades hasta el 5%. A partir del modelado por sustitución de fluidos se hizo evidente que los cambios en la saturación de agua no modifican significativamente el efecto AVO, lo cual se corrobora mediante la investigación de la migración de tiempo previo a la acumulación (PSTM), el cual verifica los resultados del modelado. La relación de amplitud entre Sawan-4 y Sawan-7 está cerca del resultado modelado. La amplitud y el comportamiento de AVO indican una menor porosidad o un espesor de arena significativamente reducido en la vecindad de los pozos Sawan-4 y Sawan-7.

Palabras clave: modelado de amplitud contra desplazamiento (AVO), sustitución de fluidos, parámetros del depósito, interpretación cuantitativa, respuesta sísmica, campo de gas Sawan.

M. Rizwan*
Department of Earth Sciences
Quaid-i-Azam University
Islamabad, 45320, Pakistan

Department of Meteorology
COMSATS Institute of Information Technology
Islamabad, 45550, Pakistan
**Corresponding author: mmrizwan@student.qau.edu.pk*

Abstract

Porosity and water saturation are among the important reservoir parameters in terms of reservoir monitoring which in turn are necessary for placement of future production wells. Amplitude versus offset (AVO) modelling and analysis technique have been utilized for quantitative interpretation of porosity and water saturation. For AVO modeling, Gassmann fluid substitution model in connection with 2D seismic angle gathers were used for reservoir monitoring over Sawan-4 and Sawan-7 wells. AVO modelling results showed significant increase of density log by substituting gas by water, moderate increase of P-wave velocity and no change in S-wave velocity. Moreover, AVO modelling proved a strong relationship between porosity and reflection amplitude for all offset ranges. The class IV anomaly was evident for all porosities down to 5%. From fluid substitution modelling it is evident that changes in water saturation do not change the AVO effect significantly which further substantiate by investigation of pre-stack time migration (PSTM) gathers verifying the modelling results. The amplitude relationship between Sawan-4 and Sawan-7 is close to the modelled result. The amplitude and the AVO behaviour indicate lower porosity or significantly reduced sand thickness in the vicinity of Sawan-4 and Sawan-7 wells.

Key words: Amplitude versus offset (AVO) modelling, Fluid substitution, Reservoir parameters, Quantitative interpretation, Seismic response, Sawan gas field.

G. Akhter
Department of Earth Sciences
Quaid-i-Azam University
Islamabad, 45320, Pakistan

A. Mustafa
Petroleum Exploration Private Limited
Islamabad, Pakistan

U. Bin Nisar
Department of Earth Sciences
COMSATS Institute of Information Technology
Abbottabad

K. Ashfaq
Department of Meteorology
COMSATS Institute of Information Technology
Islamabad, 45550, Pakistan

Introduction

The study area of Sawan gas field is located at the slop area of Thar Platform, Middle Indus Basin and extends between 24º and 28º N latitude and from 66º E longitude to the eastern boundary of Pakistan (Zaigham and Mallick, 2000). Sawan field is one of the major naturally gas producing area from Cretaceous Aged Lower Goru Formation. The sands bearing sequences of Lower Goru are potential reservoirs and consist of alternating sand-shale layers (Afzal *et al*., 2009). A, B, C and D intervals are the lithostratigraphic units of the Lower Goru Formation (Figure 1). The sand of C interval is dominantly acting as a potential reservoir in the Sawan area (Ahmad *et al*., 2004).

Hydrocarbon production causes variation in reservoir parameters like fluid type, fluid saturation, pressure, temperature and viscosity which in turn changes the seismic properties of reservoir (Lumley, 2001). Sediment saturation and porosity affect the bulk modulus, shear modulus and density of the host rock, therefore uncertainty in one parameter may affect accuracy to estimate the other parameters. After years of production, prediction of porosity and water saturation trends ease to evaluate remaining hydrocarbon potential within the reservoir. To delineate the hydrocarbon potentials of reservoirs, amplitude versus offset (AVO) method was developed (Ostrander, 1984). AVO method was initially used for synthetic models generation and their comparison to common offset stacks generated from real data. Smith and Gidlow (1987) developed the methodology to identify fluid content in reservoir through anomalies on seismic data. Afterward, the cross plot method of intercept versus gradient was developed with several alternative approaches for fluid anomalies identification (Verm and Hilterman, 1995; Castagna *et al*., 1998; Hedlin, 2000; Hilterman, 2001). On the assumption of isotropic and linearly elastic earth model, the seismic response of a sediment can be completely characterized by three parameters i.e. bulk modulus, shear modulus, and bulk density, therefore, rock physics models are often used to link seismic data to reservoir properties (Bachrach, 2006), more specifically for the amplitude versus offset (AVO) modeling. In this study, the effect of porosity and water saturation variation through AVO modeling and analysis was examined in the context of Biot-Gassmann theory (Gassmann, 1951; Biot, 1962). The availability of substantial geological & geophysical data including 2D/3D Seismic CDP gathers, complete log suites of Sawan-4 and Sawan-7 wells, allowed to perform AVO modeling and analysis over these two selected wells including the seismic lines passing there on (Figure 2).

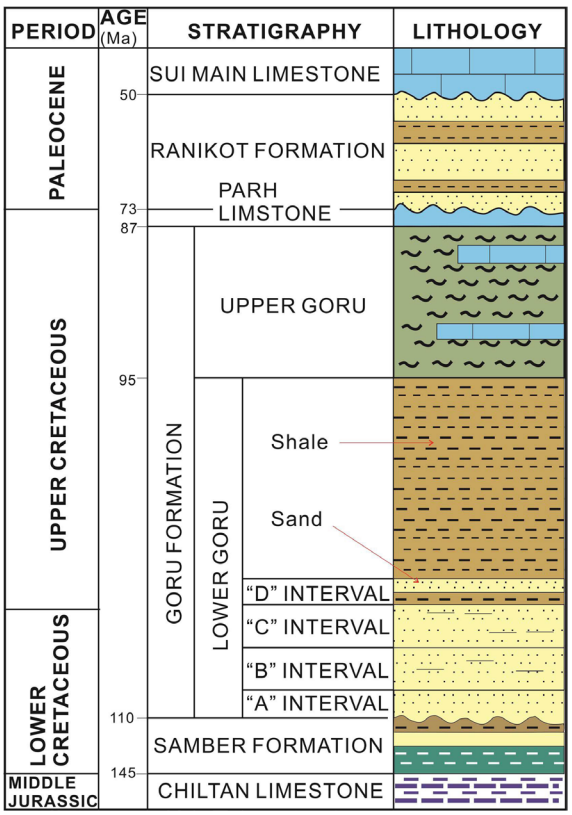

Figure 1. Generalized stratigraphic column showing alternating sand-shale distribution in A, B, C and D intervals of Lower Goru Formation (modified after Krois *et al*., 1998).

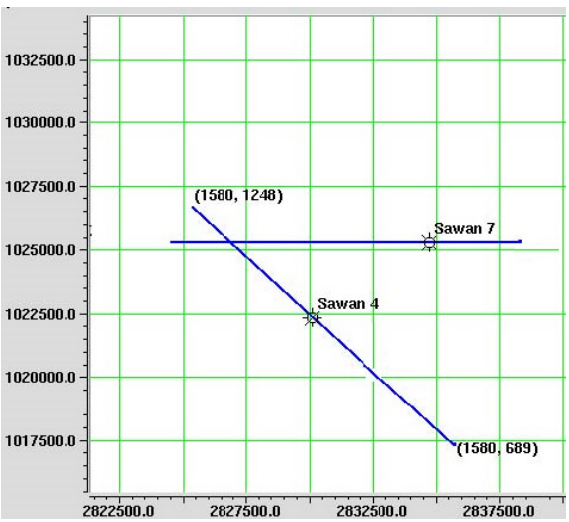

Figure 2. Base map of study area.

Methodolgy

The objective of this study was to predict the reservoir properties (porosity and water saturation) using seismic and petrophysical data, before drilling future production wells for optimum exploitation of Sawan natural gas resources. There are several techniques to relate fluid content and porosity to the seismic data but AVO modeling of Sawan wells and AVO analysis of seismic line passing from these wells were adopted to visualize the amplitude response of porosity and water saturation of C sands reservoir of the field. The models were carried out using Hampson-Russell's software. For AVO modelling, petrophysical results of Sawan-4 and Sawan-7 wells were utilized in rock physics templates (Gassmann fluid substitution Model) as input data. Seismic response of porosity and water saturation was expressed in terms of amplitude; therefore, synthetic AVO modeling has been generated by using Zoeppritz (1919) equation as a function of porosity and water saturation. AVO analysis has been done over 2D seismic lines connecting Sawan-4 and Sawan-7 wells. The fluid substitution modeling was conducted using Gassmann equation and this modelled seismic response was tied with AVO analysis results of 2D lines (Figure 2).

AVO modelling (Fluid substitution modelling)

The rock physics and elasticity theories were utilized for porosity and water saturation estimation. According to Biot-Gassmann theory, the bulk modulus of a reservoir rock can be computed from the porosity and the bulk moduli of the saturated solid, the pore fluid and the dry rock. As the pore fluids do not transmit shear, the shear modulus is unaffected by saturation.

A saturated reservoir rock with porous media consists of solid and fluid phases, the solid porous rock matrix is considered as dry rock. The bulk modulus for dry rock can be calculated through Biot empirical relation or Gassmann's backward can be employed. Once the dry rock bulk modulus is computed, the velocities of a reservoir rock can be obtained for all possible pore fluids using rock physics modelling. Moreover, the results of the petrophysical log analysis, the volume percentages for Quartz, Clay, Chlorite etc. are taken to compute the density, bulk and shear moduli of the rock matrix, so these three elastic parameters are sufficient to completely characterize seismic response of a reservoir. The fluid moduli for gas and water were calculated at the reservoir temperature and pressure of 170 ºC and 320 bar respectively. The synthetic offset dependent data was calculated with 25 Hz Ricker wavelet to get seismic response of modelled AVO data and the fluid replacement was carried out using the real density and velocity logs, known (log evaluation) lithology and log values for different porosity and saturation. The effects of replacing gas with water for Sawan-7 are shown in Figure 3.

The velocity and the density logs are shown in grey for the original logs and in red for the modelled water saturation of 100%. The biggest change is evident for the density log: the increase in water saturation results in a significant increase in density, a smaller increase is seen in P-wave velocity. The S-wave velocity decreases slightly. The leftmost gathers displayed in Figure 3 are

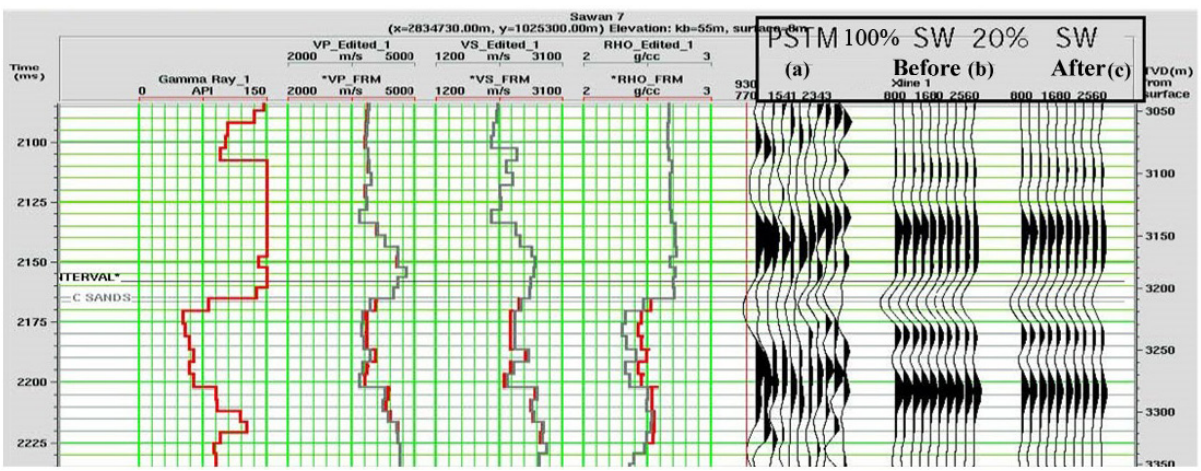

Figure 3. Sawan-7 logs and synthetic gathers before and after fluid replacement modelling. Original logs are shown in grey and modelled logs are shown in red. (a) The offset gathers show the Pre-Stack Time Migration (PSTM) gather, (b) Offset gathers from original logs, (c) Offset gathers from modelled logs.

the Pre-Stack Time Migration (PSTM) gather after offset balancing and then gathers modelled from the velocity and density logs. The offset gathers are modelled using the Zoeppritz equation from the original (middle) and the modelled logs (rightmost gather).

The visual comparison indicates a different amplitude level, but no significant change in AVO behavior. Using the gradient analysis tool on the synthetic gathers, it is quite obvious that the decrease in amplitude with offset is quite low in comparison to the change in zero incidence reflectivity (Figure 4). The decrease of amplitude with offset is almost identical between the original and the modeled full water saturation.

The same modelling procedure was repeated for Sawan-4 data. Using the well logs and the petrophysical results the water saturation is changed to 100%. The results are shown in Figure 5. The log input quality check (QC) panels display the Gamma Ray, P and S wave sonic, density log, a synthetic seismogram and the porosity and water saturation from the petrophysical analysis. A change in porosity is visible between the upper and the lower sand at Sawan-4. This manifests itself as an increase of the amplitude of the intra reservoir peak in the synthetic. The effects of the fluid replacement are less pronounced for Sawan-4 as the difference in water saturation from the original to the modelled log is lower than at Sawan-7. The change in the density log is significantly lower.

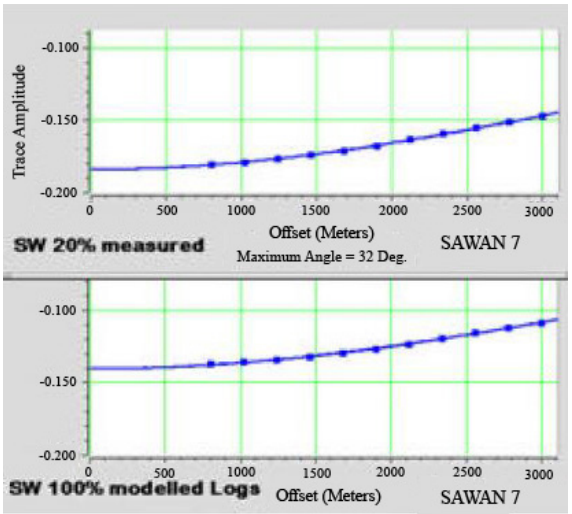

Figure 4. Sawan-7 AVO comparison between original and modelled 100% water saturation.

Water saturation and porosity variation modelling

A strong variation is seen in R_o reflectivity with changing gas saturation in the synthetic offset gathers that are computed from the Sawan-7 measured, respectively modeled logs (Figure 5). The availability of good data on the lithology from the petrophysical analysis allowed to model changes of both porosity and saturation for the Sawan reservoir in order to see the effects on synthetic seismic. For Sawan-7, two parameter variation modelling porosity range 5–25% with 5% increment and water saturation range 10–100% with 10% increment occur. The result is a modelled V_p and V_s velocity and a density logs for every parameter combination. Elastic forward modelling allows computing synthetic seismograms from these logs.

Figures 6 and 7 show the change in amplitude for near and far offset for varying gas saturation and porosity keeping one of the parameters constant. In order to compare near and far

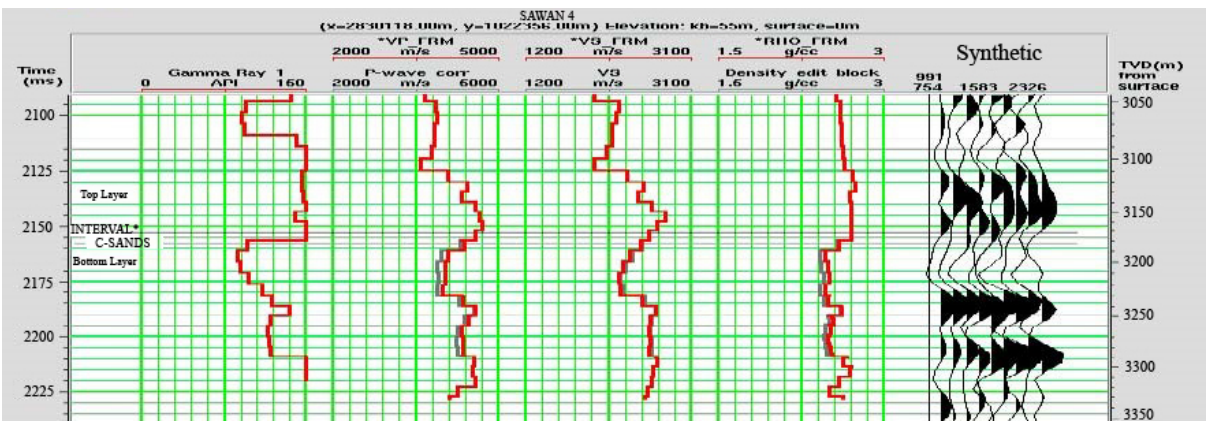

Figure 5. Fluid replacement modeling curves of Sawan-4. Original logs are shown in grey and modelled logs are shown in red. The intra reservoir peak in the synthetic is shown in bottom sand layer.

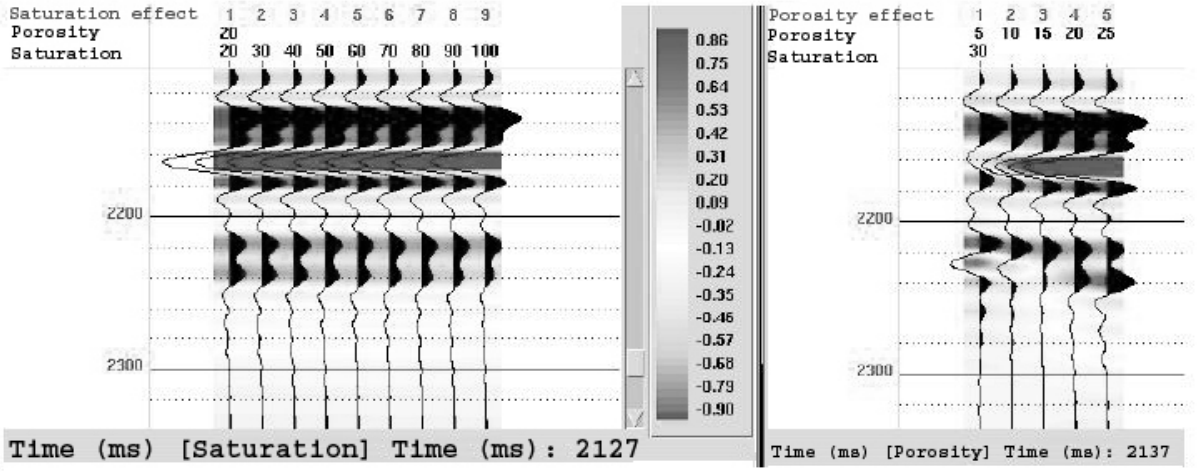

Figure 6. Sawan-7 fluid replacement modelling near offset modelled traces.

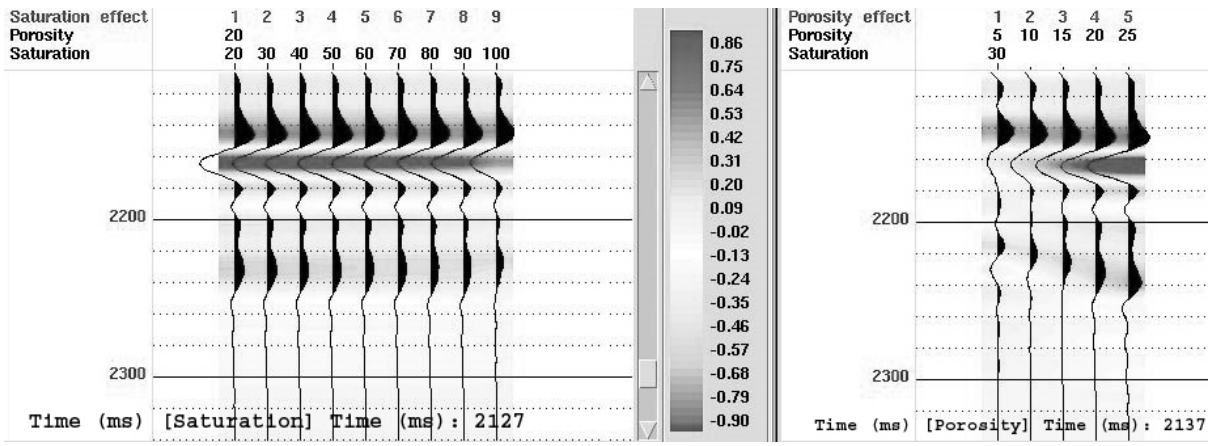

Figure 7. Sawan-7 fluid replacement modelling of far offset modelled traces.

offset trace amplitudes and the computed AVO gradient, the amplitudes were normalized to Sawan-7 response and the change in top reservoir amplitude for changes in water saturation and porosity occurred. The nominal offset for this trace is 200 m. The left panel shows the effect of changing the water saturation from 20% to 100% (at 20% porosity). The decrease in amplitude with increasing saturation is not discernible with this color and amplitude code. A significant amplitude change is visible for the change in porosity in the right panel. The computed amplitude for top reservoir ranges from 0.01 at 5% to 0.9 at 25% porosity. A similar behavior is visible in the modelled 3000 m offset traces. The amplitudes for top reservoir are lower for far offsets as already shown in Figure 4. A slight decrease in amplitude occurs for increasing saturation. The difference to the near offset change is negligible, but the change is more visible at lower amplitude levels due to more significant change in the color levels.

Figures 8 to 10 show the modelled range of saturations and porosities. Figure 8 emphasizes the results discussed earlier: amplitudes change rapidly with porosity but insignificantly with saturation. A similar picture is visible for the far offset data in Figure 9. There are a lower number of amplitude classes, but almost identical gradients. The increase of amplitude with decreasing water saturation is slightly higher for higher porosities. The effect is not large enough to be recognized in the gathers with the noise level seen in the Sawan dataset.

As the PSTM gathers demonstrate a similar decrease in amplitude between Sawan-7 and

Sawan-4, confidence in the modelling result is shown. Using the near and far trace modelling result, the AVO gradient was computed for every porosity/saturation combination. Figure 9 shows the amplitude slice for the near offset. Modelled near trace amplitude reservoir, properties decrease by 25% from Sawan-7 to Sawan-4. The computed AVO response was normalized again; the value for Sawan-7 was set to 1.

The computed AVO gradient changes significantly with porosity. The change with water saturation, recognizable for porosities of 20% and larger, diminishes with decreasing porosity. To summarize the modelling result: on both the amplitude and the calculated AVO the amplitude effect of porosity changes are many times larger than the saturation effect. The small decrease in AVO gradient visible when water saturation increases at 20% porosity, diminishes to no change in AVO gradient at 5% porosity.

AVO analysis

There are several methods to check the AVO behavior but in the present study, two methods on the gathers extracted along the 2D lines passing through the wells Sawan-4 and Sawan-7 are discussed. Several steps are taken to increase the signal/noise ratio for the AVO analysis. After the correction for residual move out macro gathers are created, by adding

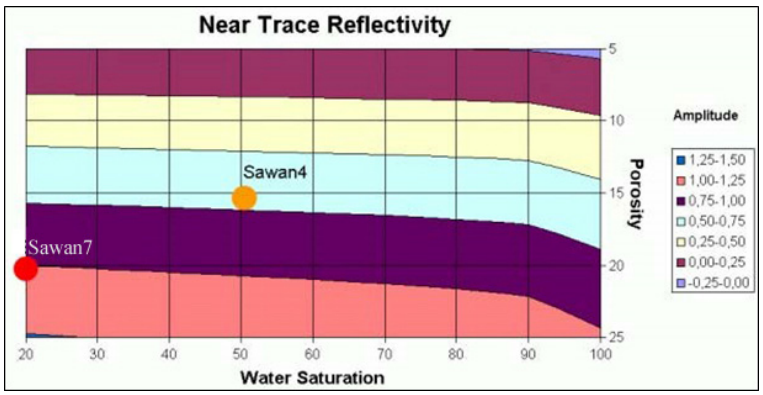

Figure 8. Near trace normalized amplitude slice. The porosity/saturation encountered in Sawan-7 is marked by a red dot and Sawan-4 by an orange dot.

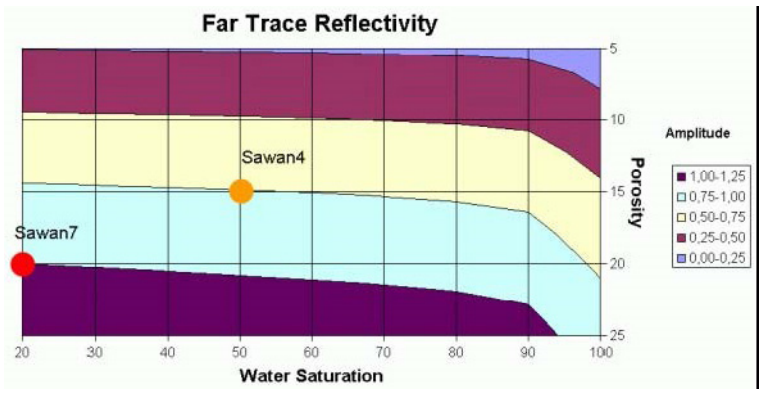

Figure 9. Far trace normalized amplitude slice. The porosity/saturation encountered in Sawan-7 is marked by a red dot and Sawan-4 by an orange dot.

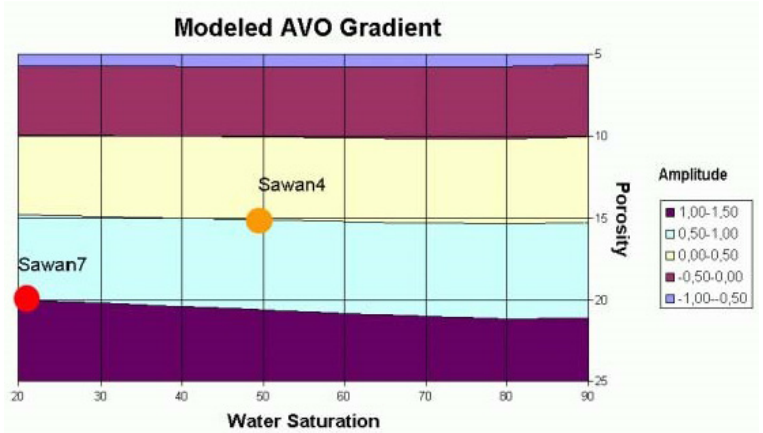

Figure 10. Normalized computed AVO gradient. The porosity/saturation encountered in Sawan-7 is marked by a red dot and Sawan-4 by an orange dot.

three adjacent traces. To preserve the offset information, this addition was performed in the offset domain. To overcome the expected problem is the creation of artificial AVO by analyzing traces with an erroneous change of amplitudes with offset ???. The comparison of the offset scaling computed within the AVO software and the correction applied in the processing sequence, showed a more stable compensation achieved in the processing. Figure 11 shows the gathers near Sawan-7 from the east-west (E-W) extracted 2D line. The uppermost panel depicts the raw gathers. The middle picture is taken after the residual normal move out (RNMO) correction and the trace mix. A significant increase in signal to noise ratio was achieved by adding, without sacrificing much of lateral resolution. The lowermost panel shows the gathers with RNMO correction, trace mix and residual offset scaling applied. The comparison shows the increase of S/N ratio with each processing step from top to bottom of Figure 11.

Figure 11 shows the AVO attributes for the E-W line connecting prospect A to Sawan-7 (yellow ovals referred as prospect A). The topmost panel shows the zero incidence reflectivity (R_o) intercept data, the middle panel displays the AVO gradient section and the lowermost panel is a composite plot: Trace

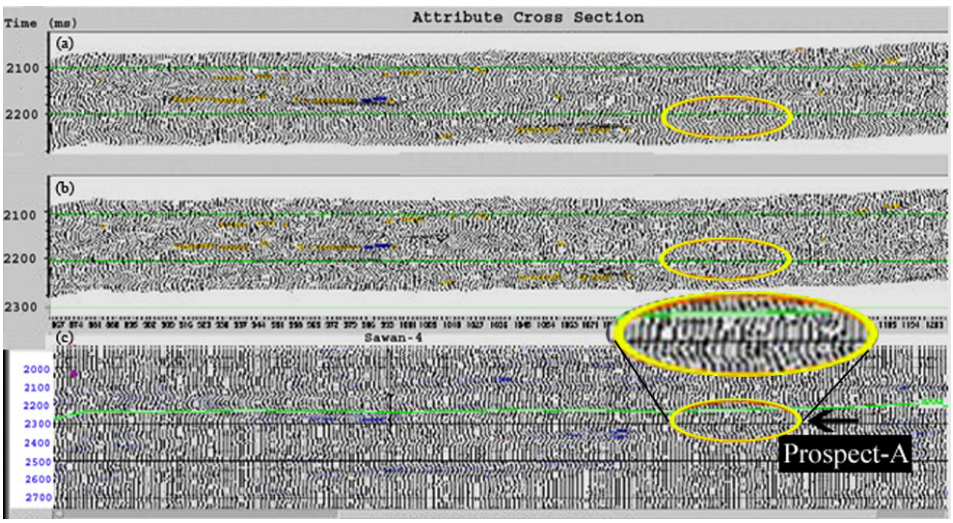

Figure 11. AVO attributes of E-W line connecting Sawan-7. (a) The zero incidence reflectivity (R_o) intercept data, (b) The AVO gradient section, (c) A composite plot with prospect-A shown by arrow.

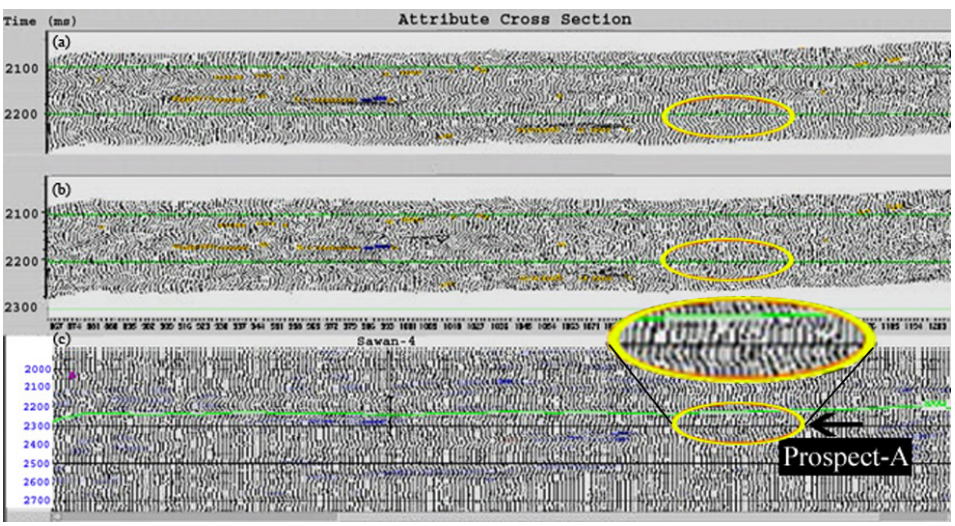

Figure 12. AVO attributes of E-W line connecting Sawan-4. (a) The zero incidence reflectivity (R_o) intercept data, (b) The AVO gradient section, (c) A composite plot with prospect-A shown by arrow.

data shows the intercept R_o and color data shows the product of intercept times gradient (R_o x GA). The top C-sand horizon shown on the composite plot is used to define the window for cross plotting. Figure 12 is a confirmation of the results already described by figure 11. The blue color of very good reservoir is just seen at the edge of the Sawan-4 anomaly, whereas the location does not show anomalous behavior at all.

AVO gradient analysis

The gradient analysis tool shows variation with offset in amplitude values extracted at a certain time sample of the gather as connected points. The smooth curves are the regression lines fitted using a linear (dashed) or robust (solid line) fitting algorithm. The correlation coefficients are shown for both methods of regression computation. The analyses are displayed for Sawan-4, Sawan-7 and around the location of selected 2D seismic lines. The results display the amplitude values extracted at the trough (for the top reservoir) in blue and the amplitudes of the next peak in red color.

As amplitude outliers are excluded from the final regression in the robust algorithm, differences between the solutions are visible. The amplitude at zero offset is largest at the Sawan-7 location (Figure 13). The slightly higher decrease of amplitude with offset shows the seismic expression of the best reservoir of the analyzed wells. The extrapolated zero offset value in the Sawan-7 gather is just below -3000. The amplitude value used for the Sawan-4 analysis found -2100 for the gather (Figure 14). This is in the range expected from the water saturation and porosity variation modeling that predicted a decrease by 40%. The correlation coefficient for the robust regression is 0.76, slightly lower than the Sawan-7 location with 0.85. Amplitude decrease with offset is slightly less than at Sawan-7.

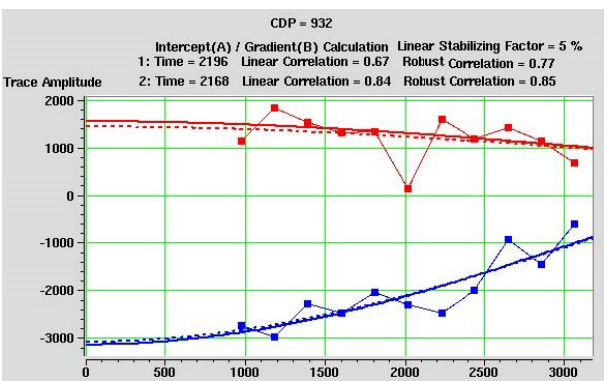

Figure 13. Sawan-7 AVO analysis at 2168 ms. The extracted amplitude values at the trough are shown in blue and at peak are shown in red respectively. The extrapolated zero offset amplitude value is just below -3000.

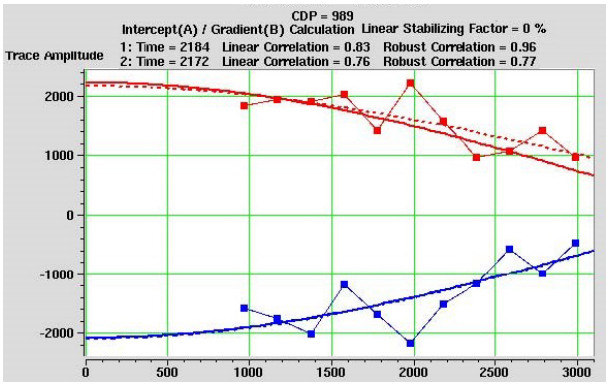

Figure 14. Sawan-4 AVO analysis at 2172 ms. The extracted amplitude values at the trough are shown in blue and at peak are shown in red respectively. The extrapolated zero offset amplitude value is about -2100.

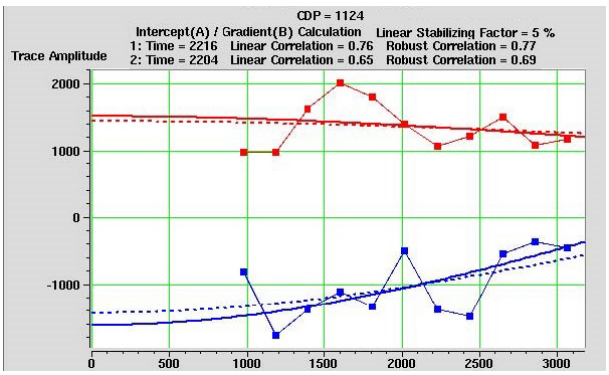

Figure 15. AVO analysis at 2204 ms. The extracted amplitude values at the trough are shown in blue and at peak are shown in red respectively. The extrapolated zero offset amplitude value is -1600.

AVO analysis was performed at common depth point (CDP) 1124 of the east-west arbitrary line at 2204 ms (Figure 15). The correlation coefficient, 0.69 for the robust solution, is just a little lower than at Sawan-4. The extrapolated zero offset amplitude is -1600. For a proposed water saturation between 50% and 70%, this amplitude would plot at a porosity of 12% in the near offset reflectivity plot in Figure 8. These single CDP analyses are used to define the robust curve fit to calculate sections of the AVO attributes used for cross plotting, namely R_o, the zero incidence reflectivity and GA, the AVO gradient from the gathers of the selected lines.

AVO cross plotting

Cross plotting of R_o, the zero incidence amplitude with GA, the AVO gradient, allows to classify the anomalies. The modeling focused to search a class IV AVO anomaly. The analysis is carried out in a window (-100 to + 200 ms) defined by the top C-Sand pick. As the seismic data was loaded in 2D mode, the analysis was done separately for each of the extracted lines.

The intercept versus gradient of the E-W line is displayed in Figure 16. The blue polygon delineates the values for the C-sand in the vicinity of Sawan-7. Data points within the polygons defined in the cross plot are highlighted with the colors. It is obvious that the good sand with anomalous R_o and gradient behavior is present only in the vicinity of Sawan-7. At this location only patch of sand behaving similar to the one found at Sawan-4. This indicates that the reservoir quality to be expected at this location will be in the range of the reservoir quality of Sawan-4 at the maximum. It is not expected to reach the sand quality of Sawan-7. The offset from the shale trend depicted by the solid red line indicates Class IV behavior of C-sand. The offset from the shale trend is quite small. Usually, zones need to define when once areas in the cross plot are picked and remembered within the system and could be used for the analysis of multiple lines. These defined zones can be shown in the respective seismic or attribute section.

Conclusions

The availability of dynamic data and improved understanding of statics of the Sawan field reservoir allowed performing AVO modelling and analysis to quantitatively predict the reservoir properties (porosity and water saturation) before drilling future production wells for optimum exploitation of Sawan natural gas resources. The fluid replacement/porosity modelling shows that R_o amplitudes change rapidly with porosity but insignificantly with saturation. A similar picture is visible for far offset reflectivity data. Amplitudes do not change a lot with water saturation. The increase of amplitude with increasing porosity is much more significant. This leads to the conclusion that AVO analyses are prone to find porous sands rather than gas saturated sands. The same can be said for elastic impedance inversion. Anomalies will point out high porosity zones rather than high gas saturation zones. The AVO gradient analyses on single gathers for Sawan-7 and Sawan-4 area show good separation in the R_o reflection amplitudes but a very similar AVO gradient. R_o was strongest for Sawan-7 and weakest for prospect A. From the analysis it can be judged that the sand quality at prospect A is the same or worse than the sand at Sawan-4 location.

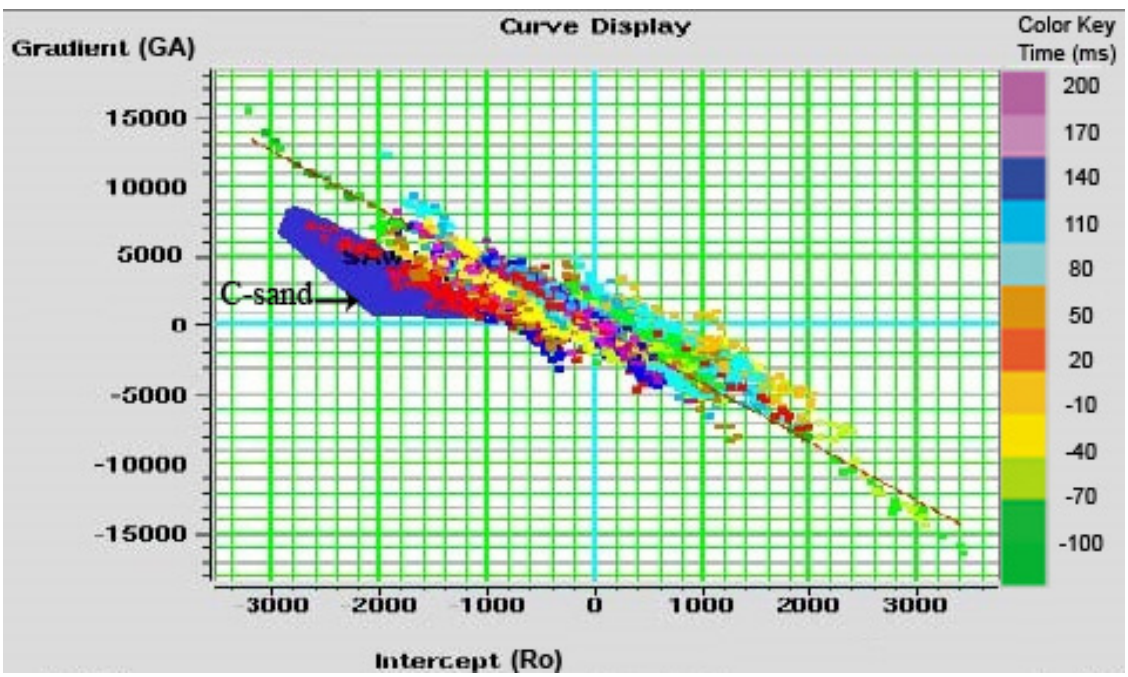

Figure 16. The gradient (GA) versus intercept (R_o) at the E-W line AVO cross plot. The time-window cross plot generated from a (-100 to + 200 ms) window around the top C-sand pick. The C-sand values are defined within blue polygon and the solid red line across data points indicates its Class IV behavior.

Acknowledgments

The authors would like to give special recognition to the Directorate General of Petroleum Concession (DGPC) Pakistan, for providing seismic and well data used in this study. We extend our grateful appreciation to our co-author (working at PEL) for software support.

References

Afzal.J., Kuffner T., Rahman A., Ibrahim M., 2009, Seismic and Well-log Based Sequence Stratigraphy of The Early Cretaceous, Lower Goru "C" Sand of The Sawan Gas Field, Middle Indus Platform, Pakistan. Proceedings, Society of Petroleum Engineers (SPE)/Pakistan Association of Petroleum Geoscientists (PAPG) Annual Technical Conference, Islamabad, Pakistan.

Ahmad N., Paul F., Sturrock S, Mahmood T., Ibrahim M., 2004, Sequence stratigraphy as a predictive tool in Lower Guru Fairway, Lower and Middle Indus Platform, Pakistan, Pakistan Association of Petroleum Geoscientists (PAPG), Annual Technical Conference (ATC), Islamabad, Pakistan, October 8-9.

Bachrach R., 2006, Joint estimation of porosity and saturation using stochastic rock-physics modeling. Geophys. 71, 5, 53–63.

Biot M. A., 1962, Mechanics of deformation and acoustic propagation in porous media. J. Appl. Phys., 23, 1482-1498.

Castagna J. R., Swan H. W., Foster D. J., 1998, Framework for AVO gradient and intercept interpretation, Geophys. 63, 948–956.

Gassmann F., 1951, Elastic waves through a packing of spheres, Geophys. 16, 673–685.

Hedlin K., 2000, Pore space modulus and extraction using AVO, in 70th Annual international meeting, SEG expanded abstracts, 170-173.

Hilterman F. J., 2001, Seismic amplitude interpretation, Short Soc. Expl. Geophys. Distinguished Instructor Series 4.

Krois P., Mahmood T., Milan G., 1998, Miano Field, Pakistan, a case history of model driven exploration Proc. Pakistan Petroleum Convention, Pakistan Assoc. Petroleum Geologists, Islamabad, 111–31.

Lumely D. E., 2001, Time-lapes seismic reservoir monitoring, Geophys. 66,1, 50-53.

Ostrander W. J., 1984, Plane-wave reflection coefficients for gas sands at non-normal angles of incidence, Geophys. 49, 1637–1648.

Smith G. C., Gidlow P. M., 1987, Weighted stacking for rock property estimation and detection of gas, Geophys. Prosp. 35, 993–1014.

Verm R., Hilterman F., 1995, Lithology color-coded seismic sections: The calibration of AVO crossplotting to rock properties, The Leading Edge, 14, 847–853.

Zoeppritz K., 1919, On the reflection and propagation of seismic waves, Gottinger Nachrichten, 1, 66–84.